



# Finite Element Approach to Photoemission of Complex Molecules

Tobias Möhle

January 15, 2017

# Contents

<b>1</b>	<b>Introduction</b>	<b>1</b>
<b>2</b>	<b>Calculation of Photoelectron spectra</b>	<b>6</b>
2.1	The Green's Function Approach . . . . .	8
2.2	Combined Bound and Continuum State Representation . . . . .	9
2.3	The Dyson Orbital Formalism . . . . .	11
2.3.1	Time-dependent Dyson Orbitals . . . . .	12
2.3.2	Time-independent Dyson Orbitals . . . . .	12
2.3.3	Sudden Approximation . . . . .	14
<b>3</b>	<b>Description of Free Particles</b>	<b>16</b>
3.1	Continuum Waves . . . . .	16
3.1.1	Stieltjes Imaging . . . . .	19
3.2	Finite Differences and Finite Volumes . . . . .	20
3.3	Pseudospectral Methods . . . . .	21
3.4	Radial Basis Functions . . . . .	22
3.5	Finite Elements . . . . .	23
3.6	Wavelets . . . . .	25
3.7	Hybrid Methods . . . . .	26
<b>4</b>	<b>Finite Element Methods</b>	<b>28</b>
4.1	Finite Element Methods for Electronic Structure Calculations . . . . .	28
4.2	Setup of the Equation System . . . . .	29
4.3	Element Types and Mesh Types . . . . .	29
4.4	Boundary Conditions . . . . .	31
4.4.1	Complex Absorbing Potential . . . . .	32
4.4.2	Non-Reflecting Boundary Conditions . . . . .	32
4.4.3	The Boundary Element Method . . . . .	33
4.4.4	Infinite Elements . . . . .	34
4.5	Solving Large Eigenvalue Problems . . . . .	37
4.5.1	Generalised Eigenproblem . . . . .	38
4.5.2	Stabilisation of Eigenproblems . . . . .	38
<b>5</b>	<b>Applied Protocol</b>	<b>41</b>
5.1	Bound State Functions . . . . .	41
5.1.1	Ground State Density . . . . .	41
5.1.2	Properties of Excited States . . . . .	43

5.1.3	OTRSH-scheme . . . . .	44
5.1.4	Obtaining the Electrostatic Potential and Dyson orbitals . . . . .	45
5.2	Free Electron Function . . . . .	47
5.2.1	Coulomb Waves . . . . .	47
5.2.2	Setup of the Grid . . . . .	47
<b>6</b>	<b>Results and Discussion</b>	<b>52</b>
6.1	Comparison of Boundary Conditions . . . . .	52
6.1.1	Dirichlet Boundary Condition . . . . .	53
6.1.2	Infinite Elements . . . . .	55
6.1.3	Conclusion on Boundary Conditions . . . . .	62
6.2	Numerical Benchmarks and Stability Tests . . . . .	62
6.3	Energy-dependence of the Cross-Section . . . . .	62
6.4	Photoelectron spectra . . . . .	65
<b>7</b>	<b>Resumee</b>	<b>68</b>
7.0.1	Boundary condition . . . . .	68
<b>A</b>	<b>Appendix</b>	<b>86</b>
A.1	Additional Data . . . . .	86
A.1.1	Comparison of Setup-schemes . . . . .	86
A.1.2	Cross section . . . . .	88
A.1.3	Photoelectron spectra of Sulphur . . . . .	88

## Notation:

- $\mathbf{r}$  vector in 3 dimensions
- $\mathbb{R}$  General matrix
- $|\Psi\rangle$  one-particle wave function
- $|\Phi^{\text{DO}}\rangle$  Dyson orbital
- $|\Phi^{\text{el}}\rangle$  Free electron function
- $|\Psi^N\rangle$   $N$ -electron wave function
- $\hat{a}/\hat{a}^\dagger$  annihilation/creation operators:.

## Abbreviations:

- BC boundary condition
- CAP complex absorbing potential
- CI configuration interaction
- DO Dyson orbital
- DFT density functional theory
- DVR discrete variable approximation
- ESP electrostatic potential
- eV electron volt
- FD finite difference
- FEF free electron function
- FEM finite element method
- FE-DVR finite element discrete variable approximation
- FV finite volume
- HOMO highest occupied molecular orbital
- LCAO linear combination of atomic orbitals
- LUMO lowest unoccupied molecular orbital
- OTRSH optimally tuned range-separated hybrid
- RBF radial basis function
- SCF self-consistent field
- SD Slater determinant
- SA sudden approximation
- SE Schrödinger equation
- TDDFT time dependent density functional theory

# 1 | Introduction

Steady state as well as time-resolved photoelectron spectroscopy have become widely used tools to study the composition of gases and liquids [1–4], the structure of solids [5] as well as chemical reactions such as electron transfer [3]. The process studied by photoelectron spectra is the absorption of a high-energetic photon (usually in the ultra-violet to hard X-ray regime) by an  $N$ -electron system which leads to the release of an electron whose kinetic energy is measured. This process is sketched in Figure 1.1 where the bound states are depicted by horizontal bars and the states of the outgoing electron are visualised by the gradient-filled block, indicating that its energy is continuous. Measuring the kinetic energy of the photoelectron yields information on the energy of its previous states due to energy-conservation over the process.

One of the main reasons for the broad success of this particular type of spectroscopy is that these spectra are very sensitive to small changes in the chemical environment and hence yield information not only about the chemical structure of molecules but also about intermolecular interactions as for example solvation effects [1, 6–9]. Furthermore, photoelectron spectroscopy provides a more direct access to the energy levels than optical absorption and emission spectroscopy since the transition energies are obtained with respect to the vacuum level and no “dark” states occur due to different selection rules. Finally the ease of handling charged particles experimentally makes this method appealing and a good temporal resolution can be achieved by varying the path in the time of flight spectrometer. Moreover, besides its capabilities in steady state spectroscopy, photoelectron spectra are the standard tool to study attosecond physics due to the naturally high energy of the short pulses which ionise the systems under

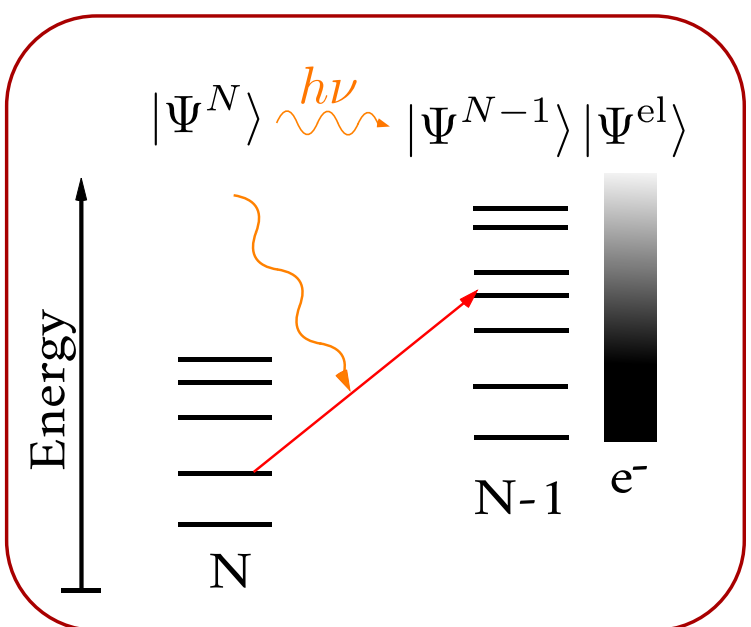


Figure 1.1: Schematic representation of a photoelectron transition : an incoming photon with energy  $h\nu$  ionises the  $N$ -electron system, transferring it into a free electron in a continuum state and a system of  $N - 1$  bound electrons. The bars denote bound states, the color-gradient depicts the energy of the outgoing electron.

study [10–15]. However, a limitation of photoelectron spectroscopy is that the short free-path of electrons in condensed phases limits the probe depth significantly.

Having performed a measurement of a photoelectron spectrum (PES) it is, at least for complex systems, rich of features and hence the interpretation requires theoretical methods. This especially applies to systems with strong electron correlation which manifests itself in the appearance of combination transitions. Over the decades a large variety of methods to calculate photoelectron spectra have been developed at different levels of theory. In literature often the theoretical spectra are estimated on the basis of Koopmans' theorem [16], (or its density functional theory (DFT) counterpart [17],) assuming equal intensities for all transitions [18–21]. Even though this is a quite successful approach for solid states [22, 23] and gives an easy interpretation, it is too simplistic in many cases since it neglects electron relaxation and correlation effects and hence may give an invalid picture as shown by Cederbaum *et al.* even for small systems such as various diatomics [24, 25]. Furthermore in this model no reliable information about intensities can be obtained. To retrieve quantitative transition strengths, more advanced models are needed. Since simulations in time-domain are very demanding they are only applied to small molecules, mainly to study strong-field effects such as high harmonic generation [11, 26–29] which can not be described in frequency-domain. In this thesis however the focus is on complex molecular systems and a wide range of kinetic energies, while more moderate field strengths should be applied. Hence frequency-domain methods derived from a perturbation theory with respect to the irradiating electromagnetic field are applicable here.

In this thesis, the PESs are calculated within the Dyson orbital (DO) formalism which is derived and explained in more detail. This formalism is based on Fermis' Golden Rule [30] and allows a reduction of the dipole moment matrix element from an  $N$ -electron integral to effective one-particle quantities. Thereby the initial state and the bound part of the final state are represented by a one-electron quantity denoted as DO. The other wave function entering the dipole moment operator is the free electron function (FEF). In this formalism electron relaxation and correlation effects between bound states of the unionised and ionised systems are included, allowing the description of combination transitions. Per contra, this formalism neglects the correlation of the outgoing electron with the ionic remainder and thus may neglect certain transitions [31].

Since the bound state wave functions can be obtained from standard quantum-chemical tools, the computation of the DO is straightforward even though technically demanding [32]. The computation of the FEF is in general not trivial since analytic solutions are known only for few special cases such as hydrogen-like atoms [33] and general basis sets as they are used for bound states are not available. Among others, three analytic expressions have been suggested, each based on an expansion of spherically symmetric functions in plane waves [34]. One of them is the spherical wave basis which is a set of solutions of the Schrödinger equation (SE) without any potential and hence is especially well-suited for photodetachment from negative ions, leaving systems in an uncharged state [34, 35]. The other two expansions are based on Coulomb waves which assume a Coulomb potential and hence are exact for the ionisation of hydrogen-like atoms [33]. Thereby one of them is an expansion in Coulomb waves for the given momentum vector  $\mathbf{k}$  while the other is an asymptotic expression for Coulomb waves with vanishing momentum (Coulomb  $|\mathbf{k}| = 0$ ).

The functions each are expanded in a series of increasing quantum numbers for angular momentum  $l$  and its projection  $m$ . Since all three functions assume spherical symmetry of the potential, they are expected to give a good approximation to the real FEF for spherically symmetric systems only. Ionisation *e. g.* from a delocalised orbital of a linear molecule have a different symmetry and thus can be expected to be described only crudely by this approach. The effects due to lower molecular symmetry become especially important for low kinetic energies because the interaction with the ionic remainder becomes strong in this case.

To analyse the quality of a given expression for a FEF, it is instructive to study the intensity of a given transition as a function of kinetic energy. Such a study is examined in Figure 1.2, showing the intensity of the photoionisation transition from the highest occupied molecular orbital (HOMO) of water for different kinetic energies of the photo-electron, estimated with the above-mentioned expansions. The comparison shows that all three expansions yield different intensities for most transition energies. Besides leading a wrong wrong symmetry of the FEF, these expansions yiled even in the limit of infinite terms only a plane-wave, neglecting the ionic potential and hence are not asymptotically correct.

To overcome the restrictions in symmetry and kinetic energy of the photoelectron function, an explicit formulation is needed, taking the molecular electrostatic potential experienced by the outgoing electron into account. Assuming that the correlation between the FEF and the bound states of the ion is weak (which is a prerequisite for the DO formalism anyway), one can use the mean-field potential of the molecular remainder. This allows for obtaining the FEF from the one-electron SE with an appropriate potential and thus reduces the complexity compared to the exact case where a coupled  $N$ -electron equation needs to be solved, considerably.

In the thesis at hand a good approximation to the FEF is aimed which should be applicable to a wide range of molecules and photon energies. Such a flexible description is possible exploiting the finite element method for solving the SE. In the finite element method, the space of interest is subdivided into small volume elements and solved variationally with stepwise polynomials whose support spans over one or few elements only [36, 37]. The finite element description is especially efficient here since the size of the elements

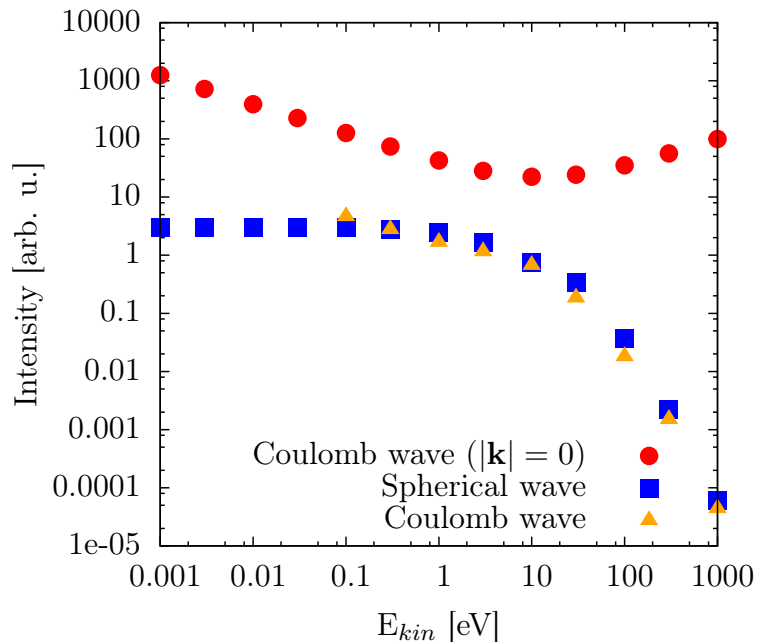


Figure 1.2: The intensity of the lowest-lying transition of water depending on the kinetic energy of the photoelectron. Each expansion is performed up to  $l = 10$ .

can be locally adapted to reproduce finer structures or broader shapes [36, 38]. Using finite elements, the one-particle SE is formulated a generalised eigenvalue problem with sparse matrices.

An important characteristic of the exact FEF is its spacially infinite extend which can not be handled by the finite element method. To describe the function in a good approximation, the finite elements are extended by infinite elements [39–42] which are volume elements with infinite radial extend that are connected to the outer surface of the finite element region. Thereby the radial function is a polynomial in  $\frac{1}{r}$  multiplied by  $e^{ikr}$ , resembling the asymptotic behaviour of known analytic solutions and fulfilling the Sommerfeld radiation condition [43].

The bound states can be obtained on the level of density functional theory (DFT) which is a formally exact method based on the Hohenberg-Kohn theorem [44], stating that the total electron density determines all system properties such as electronic binding energies. However, the correct form of the exchange potential as well as the kinetic energy are not known as functionals of the electron density and hence approximate functionals need be used. While the kinetic energy can be estimated reasonably by the Kohn-Sham scheme [45], the expressions used for the exchange-correlation potential yield electron densities that have a wrong long-range asymptotic decay which affects the observables of these systems [19, 20, 46]. To reduce this error, range-separated hybrid functionals are used where the usual DFT exchange functionals are used at small distances while a Hartree-Fock exact exchange ensures the correct behaviour at larger distances. The interchange between these contributions is modelled via an error function with a characteristic distance that is optimized for each system separately. This procedure has been observed to enhance the accuracy of the predicted properties such as the orbital energies [46–49].

While the schemes described above are well established, their combination is only rarely used. Especially the FEF is found in literature to be approximated only crudely as plane-wave functions [50] or in some expansion as described above [32, 34, 47]. The goal of this thesis is to use the DO formalism with bound states being described by DFT using the above-mentioned optimized range-separated hybrid (OTRSH) functionals to obtain accurate orbital energies and complement it with a FEF that accounts the molecular electrostatic potential explicitly using the finite and infinite element methods which have been applied only to very few quantum mechanical problems [51, 52].

In the protocol used the DFT and time-dependent DFT calculations for excited states are done using a locally modified version of **NWChem** [53] and the **Gaussian 09** package [54]. From those, the DO is calculated with the in-house code **DYSON** developed previously [32]. A self-written interface extracts the required data as *e.g.* the molecular orbital coefficients and overlap matrix of atomic orbitals from the output of these programs. For the computation of the FEF, the program **FreeWilly** [55] is developed using the finite element library **Libmesh** [56]. **Libmesh** is an open source library that provides a broad range of capabilities and interfaces to several high-performance linear algebra libraries [57–59]. Moreover, it supports MPI parallelisation and implements a recent formulation of the above-mentioned infinite elements [42]. Especially the latter is to the best of my knowledge a unique option. Furthermore it has an automated procedure to adaptively refine or coarsen the elements according to local error estimates.

The goal of this thesis is to find a systematic way to setup the finite element mesh

for any given molecule to describe the photoelectron with a reasonable accuracy that goes beyond the capabilities of existing programs in this field. The developed protocol is applied to seval systems. To show the properties of the respective setup and compare different schemes suggested, atomic hydrogen is used for which an analytic solution, namely the Coulomb waves, is known. Further tests are applied to lithium, **doing ....** and **Cross section**. As a simplet test-system for a molecular case carbondioxide is chosen for which several experimental as well as theoretical reference-data are available, **studying the PES and croos section**. For this system, the usual approach to represent the FEF as a Coulomb wave is expected to be not valid. Finally, as a representative for larger and more complex molecules, here benzene is chosen which is a well-studied system.

## 2 | Calculation of Photoelectron spectra

The large variety of systems and effects studied with photoelectron spectroscopy led to the existence of diverse methods for theoretical modelling of the spectra [60, 61]. In this work, the focus is put on steady-state photoelectron spectra of molecular systems with a size up to some tens of atoms. As light source, here a classical ultra-violet or soft X-ray source with a discrete spectrum such as a gas discharge lamp or a laser is assumed where the strength of the applied electromagnetic field is weak and the kinetic energy of the outgoing electrons reaches at most tens of electronvolt but may become arbitrarily small.

A summary of methods that can be used to describe the most important scenarios arising in photoelectron spectroscopy is given in the Table 2.1 and some of them are described in more detail in the following sections. The main classification of these methods can be done dividing them into time and frequency domain. These domains are related to each other via the Fourier transform but provide different pictures and properties. Using a frequency-domain method, the Hamiltonian has to be diagonalised to obtain the states' energies and wave functions. In contrast to this, in time domain the Hamiltonian is applied to an initial state to propagate the system in time. Usually such a simulation needs several thousands of propagation steps to obtain reasonable accuracy. Moreover, the joint treatment of bound and continuum states demands a large and flexible basis which makes time domain methods usually computationally very demanding and restricts their applicability to small systems as shown in the Table 2.1. On the other hand, in frequency-domain the nonlinear response properties are neglected so that strong-field effects such as multiphoton ionisation and high harmonic generation (HHG) can not be treated. Due to the different treatment of the system in both domains, they each have a set of methods that can be used and which are more or less specific to the domain as shown in the third column of Table 2.1. The same holds for the quantum chemical methods available to treat the system.

	Field Str.	Method	System Size	Typical Problems	QC <sup>(a)</sup>
Time-domain	weak to strong	TDDO [62] SE Green's function	atoms [63], diatomics [26, 64, 65] triatomics [66]	HHG [27–29], Multiph. ionisation attosec. dynam.[10–15]	(TD)DFT, GASCI [63], EOM-CC [67], CASSCF
Frequency-domain	weak	R-Matrix [68–72] DO [35, 50] Green's Function [73, 74] Koopmans'[17, 75, 76]	up to biomolecules [77], solid state [22, 23]	steady-state, angle-res. PES time-res. PES	CI[78] RASSCF [32, 47, 79, 80], TD-DFT

Table 2.1: Overview of time- and frequency-domain methods and theyr typical applications.

<sup>(a)</sup>QC: quantum chemical; GASCI: generalised active space configuration interaction; CASSCF: complete active space self-consistent field; EOM-CC: equation of motion- coupled cluster; RASSCF: restricted active space self-consistent field.

Besides the distinction according to the domain, the methods can be also categorised according to the partitioning of the system they use which is sketched in Figure 2.1. The simplest and crudest method is an approach derived from Koopman's theorem where only the ground state of the un-ionised state is considered which is visualised in Figure 2.1 by the fact that the box for this method is only at the  $N$ -electron system. Similarly, also the Green's function approach treats only the initial state but accounts for electron relaxation and thus correlation effects during ionisation due to its quasi-particle picture. In the DO formalism, in contrast, the final state is treated explicitly, using a partitioning into the bound  $N - 1$ -electron state  $|\Psi^{N-1}\rangle$  and the FEF  $|\Psi^{\text{el}}\rangle$ . Finally a large class of methods treat the system uniformly, using a joint treatment for the bound and continuum states as indicated by the single box in Figure 2.1.

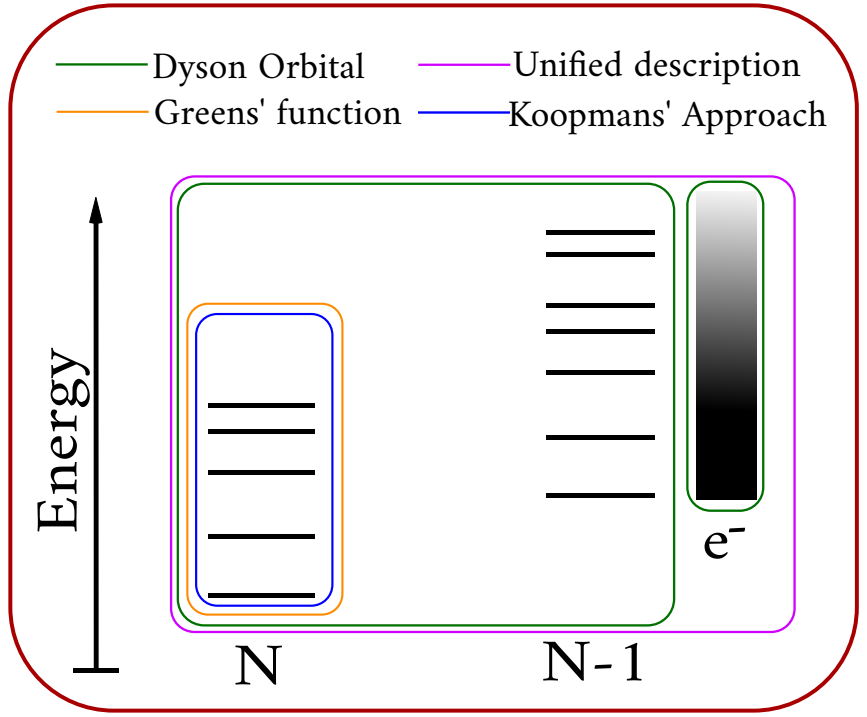


Figure 2.1: Scheme of the system-representation used in the different methods.

The Koopmans' approach is, at least among the frequency domain methods, the most prominent representative [19, 75, 76, 81]. In this scheme, the systems ground state is computed with a self-consistent field quantum mechanical method to obtain the one-electron binding energies. The photoelectron spectrum is than estimated using the orbital energies as the transition energies and using uniform intensities. Although this method has shown to be in qualitative agreement with experiments for different systems [19, 20, 81–83], it breaks down in case of strong electron correlation [24, 74] due to relaxation of the orbitals upon ionisation. This method is characterised by its low computational costs and robustness and, thus, is well-suited for very large systems such as solid state problems where calculations beyond ground-state DFT are very demanding or not feasible at all.

In the following sections, the most important methods will be briefly introduced according to their affiliation to the groups distiguished in Figure 2.1. First, in section 2.1 the working equations of the Green's function approach are introduced to give a fundamental understanding of this group of methods. Thereafter, in section 2.2 several approaches both in time- and frequency-domain are described that use a unified description of the complete  $N$ -electron system. Finally the DO formalism is derived in more detail, since it is the method of choise in this work, in section 2.3.

## 2.1 The Green's Function Approach

From a formal point of view, the computation of photoelectron spectra using the Green's function approach is similar to the use of Koopmans' approach since in both methods only the ground state of the unionised system is considered. However, the level of theory achievable when using Green's functions is much higher.

In contrast to most other quantum-chemical methods, in the Greens' function approach expectation values for a given operator  $\hat{O}$  are not computed as a scalar product  $\langle \Psi^N | \hat{O} | \Psi^N \rangle$  with the wave function  $|\Psi^N\rangle$  of the  $N$  electron state of interest, but by contour integrals with the Greens' function [84, 85]. Thereby the (one particle) Greens' function is a matrix  $\mathbb{G}$  whose elements are defined as

$$G_{i,j}(t, t') = -i\langle \Psi^N | \hat{T} \left( \hat{a}_i(t) \hat{a}_j^\dagger(t') \right) | \Psi^N \rangle \quad (2.1)$$

with the creation operator  $\hat{a}_j^\dagger(t) = e^{i\hat{H}t} \hat{a}_j e^{-i\hat{H}t}$  of an electron in state  $j$  at time  $t$  in Heisenberg picture and the annihilation operator  $\hat{a}(t) = e^{-i\hat{H}t} \hat{a}_j e^{i\hat{H}t}$  respectively.  $\hat{T}$  is the Dyson time ordering operator that orders the operators  $\hat{a}$  and  $\hat{a}^\dagger$  by their time arguments to ensure that the operator with smaller time argument acts first [84]. Hence, the Greens' function can be interpreted as an additional electron (or hole, depending on the time ordering) propagating from  $t'$  to  $t$  in a system described by the Hamiltonian  $\hat{H}$  [84].

To find an expression of the Green's function (2.1) from which the transition energies and intensities can be extracted, it needs to be reformulated. In the first step, the time ordering operator is written explicitly which results in

$$G_{i,j}(t, t') = i\langle \Psi^N | \hat{a}_j(t) \hat{a}_i^\dagger(t') | \Psi^N \rangle \Theta(t - t') - i\langle \Psi^N | \hat{a}_i^\dagger(t') \hat{a}_j(t) | \Psi^N \rangle \Theta(t' - t). \quad (2.2)$$

Inserting the closure relation  $\hat{1} = \sum_k |\Psi_k^M\rangle \langle \Psi_k^M|$ , where  $M = N \pm 1$  and  $|\Psi_k^M\rangle$  describes a bound state, between the operators in both terms of (2.2), the Lehmann representation [84] is obtained whose Fourier transform is

$$G_{i,j}(\omega) = i \sum_k \frac{\left| \langle \Psi^N | \hat{a}_j | \Psi_k^{N+1} \rangle \right|^2}{\omega - (E_k^{N+1} - E^N) + i\nu} - i \sum_k \frac{\left| \langle \Psi^N | \hat{a}_i^\dagger | \Psi_k^{N-1} \rangle \right|^2}{\omega + (E_k^{N-1} - E^N) - i\nu}, \quad (2.3)$$

where  $\nu$  is a small parameter arising from calculation of principal value and  $\omega$  denotes the argument of the Fourier transform while  $E^N$  and  $E_k^M$  are the energies of the  $N$ -electron ground state  $|\Psi^N\rangle$  and of the  $k$ -th  $M$ -electron state  $|\Psi_k^M\rangle$ , respectively. In this form, the second sum corresponds to transitions in the PES: the nodes of the denominator (poles of the Greens' function) can be easily assigned to the ionisation potentials and, thus, the transition energies in photoelectron spectra. Further, the integrals in the nominator are equivalent to the sudden approximation derived in chapter 2.3.3 and hence provide a good approximation to the transition strengths. The terms in the first sum correspond to the respective quantities of electron detachment [85].

However, computing the Greens' function is a demanding task which is of similar complexity as the computation of a solution to the SE. Over the years several approaches were developed of which the algebraic diagrammatic construction [85] and the equation

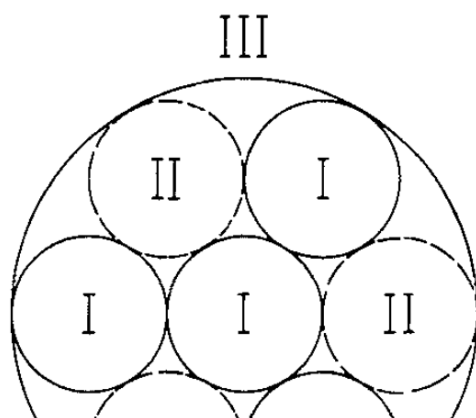
of motion [81, 85] are the most prominent. In the diagrammatic construction one starts with an initial zeroth order Greens' function  $\mathbb{G}^0(\omega)$  constructed in a Hartree-Fock basis and corrects it iteratively by the term  $\mathbb{G}^0(\omega)\Sigma(\omega)\mathbb{G}(\omega)$ , where  $\Sigma(\omega)$  is the self-energy, an effective potential that is used to recover electron correlation and relaxation effects [73]. The self-energy usually is expanded in a perturbation series with respect to Feynman diagrams with increasing number of vertices and is exact in the limit of infinite terms [84, 86]. The one-particle energies, Coulomb matrix elements and overlap integrals are obtained from self-consistent field (SCF) calculations [85] *e.g.* on the HF-level [73] but (TD)DFT or any other quantum chemical method can be used as well via the GW-approach [87, 88]. Being much easier to compute, the Hartree-Fock basis has the disadvantage that only single configurational electronic states can be treated.

On the other hand, an important advantage of the Greens' function method is that the transition energies are computed directly whereas in most other methods they are calculated as the difference of the initial and final state energies. The latter approach however can lead to errors in the electronvolt range when the difference in the correlation energy is badly estimated [85].

## 2.2 Combined Bound and Continuum State Representation

In contrast to the Greens' function method, in which the explicit description of the FEF omitted, a large group of methods describes the full  $N$ -electron system before and after the ionisation, respectively (see Figure 2.1). In this section a selection of such methods is presented. The treatment of bound and continuum states, however, requires a very flexible formalism whose large computational costs restrict its applicability to small systems that often fulfil certain symmetry-requirements and have a small amount of electrons.

The most prominent representative of this class in frequency domain is the R-matrix method [70, 71, 89]. Its general idea is to conduct a partition of space into regions which are treated differently and connected by explicit boundary conditions to ensure smoothness of the wave function. These regions are constructed with concentric spheres, restricting the symmetry of wave functions in this scheme. Nonetheless it is found to be applied not only to atoms [68, 69, 90] but also to small molecules [72, 91]. In the R-matrix formalism the inner region is chosen large enough to contain the bound part of the  $N$ -electron function that is usually represented by a configuration interaction (CI) expansion of Slater determinants (SDs), using a linear combination of atomic orbitals (LCAO) basis or a grid representation [70]. The FEF is commonly described by a linear combination of bound orbital type functions and continuum functions such as Coulomb waves [71, 89]. In the outer region, an expansion in Coulomb waves is used to ensure the asymptotically correct behaviour. In addition to the inner region and the asymptotic outer region further intermediate regions can be added where the FEF is represented by a multipole-radiation expansion which is a polynomial of



inverse powers of the distance to the centre [70].

A generalisation to non-spherical systems is employed, *e.g.*, by Johnson [92] who used different kinds of non-concentric spheres. One set spheres is centred at atoms while others are placed in the interatomic regions such that the space is filled as dense as possible as shown in Figure 2.2 for a molecule with four atoms. Each atom is located in the centre of a circle denoted as I while the circles II fill the interatomic space. An outer sphere surrounds the molecule to account for the asymptotic region similar to the asymptotic region in R-matrix theory. In this scheme, the exchange-correlation is treated on an approximate level [93] and is spherically averaged, resulting in a description that is equivalent to the muffin-tin potential which is a well-known model in solid state physics [94, 95]. The continuity of the wave-functions as well as their derivatives is ensured over the regions via multiple-scattered-wave theory [92]. The wave-functions are chosen in each region as a one-centre expansion in spherical coordinates of the form

$$\Psi(r, \theta, \phi) = \sum_{l=0}^{l_{\max}} \sum_{m=-l}^l c_{l,m} R_l(r) Y_l^m(\theta, \phi) \quad (2.4)$$

where  $r, \theta, \phi$  are the spherical coordinates and  $Y_l^m(\theta, \phi)$  are the spherical Harmonics [33] and the radial function  $R_l(r)$  is a solution of the radial SE

$$\frac{\partial^2 R(r)}{\partial r^2} + \left( 2(E - V(r)) + \frac{l(l+1)}{r^2} \right) R(r) = 0 \quad (2.5)$$

with the respective spherically averaged potential  $V(r)$  [92].

An approach applied by DeCleva *et al.* to  $H_2^+$  [26] and benzene [96] refrains from the use of spheres, allowing for more general boundaries between the inner and outer regions. Here the FEFs are globally represented as the one-centre expansion (2.4) where  $R(r)$  is expressed by a B-spline basis. An advantage of the spline-based description is that smoothness at the interface between the regions is ensured intrinsically.

Another scheme in frequency domain is used by Richards and Larkins [97] with a hybrid ansatz: The bound states of the  $H_2$  molecule are described in the common LCAO scheme and the FEF is described by the product ansatz  $\Psi(\mathbf{r}) = R(r, \theta) e^{im\phi}$ , which is a generalisation of (2.4), where  $R(r, \theta)$  is obtained from a two-dimensional SE on a regular grid using a finite difference (FD) scheme. In contrast to the previously described methods, here no partition of space is performed but instead a finite box with Dirichlet boundary conditions is used. Moreover, the FEF is treated on the HF-level, neglecting correlation effects [97].

Similar descriptions are used in time domain by several authors [63, 67, 98]. Even though they are much more demanding than calculations in frequency domain, time do-

main methods can predict strong-field effects and are used to simulate attosecond dynamic which is both not achievable using frequency-domain methods.

An important difference between time- and frequency-domain methods of practical use is that in time-domain unbound particles are described by a wave packet and hence as a localised function. Moreover, at short times after ionisation the continuum states often can be assumed to be of similar spacial extend as bound states, allowing the basis to be a linear combination of bound state functions but having a complex energy whose real part introduces oscillations and the imaginary part damps the wave function, leading to a finite lifetime of the function [67]. Moreover a complex absorbing potential (CAP) (discussed in chapter 4.4.1 in more detail) is most often applied, ensuring that the continuum states can be described by bound-state functions by cutting off that part of the wave function which is not localised at the molecule anymore. Due to these considerations the LCAO basis can be used for the description of the free particles as well, see *e.g.* Jagau *et al.* [67]. In other simulations, grid-based descriptions are chosen using symmetry-adapted coordinate systems [66, 98–100], allowing for a product ansatz similar to (2.4) and hence a reduction in dimensionality. On the remaining one-dimensional grids often a discrete variable representation (DVR) (described in section 3.3 of this thesis) is chosen. As an example, Yip *et al.* [101] simulate double ionisation of atomic beryllium in spherical coordinates, using the expansion (2.4) where  $R(r)$  is separated into two regions in which a DVR and a finite element DVR (FE-DVR) scheme are used respectively. As other examples, Tao *et al.* [98] as well as Bauch *et al.* [63, 64] use the FE-DVR basis in spheroidal coordinates.

The examples introduced above represent only a small fraction of the methods used to describe photoionisation in frequency and time domain. But a drawback that is common to these methods is that a large number of continuum functions is required which are correlated with the bound electrons and thus lead to a computationally expensive description of the system. To overcome this drawback, in the DO formalism that is presented in the coming section the description of bound and continuum states is separated into separate problems.

## 2.3 The Dyson Orbital Formalism

The Dyson orbital (DO) formalism can be considered as an approximation to the methods described above. Here the free and bound states are described separately, see Figure 2.1, using a product ansatz. Using such a separation leads to a neglect of correlation effects between the outgoing electron and the bound states and is often denoted as sudden ionisation limit [32, 34]. Moreover, non-linear effects as well as recombination transitions are not considered within DO theory. An important advantage, however, is that the overlap between the initial state and the bound part of the final state is formulated as a one-electron quantity, called DO which can be used to simplify the description of the photoionisation process. Usually the DO scheme is considered in the frequency domain, but a time domain formulation exists as well and is described in the following section [62].

### 2.3.1 Time-dependent Dyson Orbitals

A good starting point for the DO formalism is an expansion of the time-dependent  $N$ -electron function  $|\Psi^N(t)\rangle$  (omitting the spacial coordinates for brevity) in the form

$$|\Psi^N(t)\rangle = \frac{1}{\sqrt{N}} \sum_k |\Psi_k^{DO}(t)\rangle |\Psi_k^{N-1}\rangle e^{iE_k^{N-1}t} \quad (2.6)$$

where  $E_k^{N-1}$  are the energies of the  $N - 1$ -electron bound states described by the time-independent wave functions  $|\Psi_k^{N-1}\rangle$  that are complete in the space of  $N - 1$ -electron wavefunctions. The expansion coefficients  $|\Psi_k^{DO}(t)\rangle$  have the dimensionality of a one-particle function and are denoted as time-dependent DO (TDDO). An important feature of the expansion (2.6) is that the dynamics of the  $N$ -electron system is reduced to a system of one-electron quantities  $|\Psi_k^{DO}(t)\rangle$ , propagated according to the electronic SE [62]. In this approach the interaction of the DO with the bound states is approximated by the mean-field electrostatic potential (ESP) [62], neglecting exchange and correlation.

The physical interpretation of the TDDO becomes clear when regarding its definition, given by the  $N - 1$ -electron integral

$$|\Psi_k^{DO}(t)\rangle = e^{iE_k^{N-1}t} \sqrt{N} \langle \Psi_k^{N-1} | \Psi^N(t) \rangle_{N-1}. \quad (2.7)$$

The remaining coordinate (2.7) belongs to the photoelectron since  $|\Psi^N(t)\rangle$  is restricted to the description of bound states. Considering eq. 2.7 in a frozen orbital approximation, *i.e.* one-electron ionisation, the TDDO corresponds to the photoelectron. However, relaxation effects lead to non-orthogonal orbitals of the  $N$ - and  $N - 1$ -electron systems and thus lead to additional contributions to the TDDO. Therefore, when considering relaxation effects, the TDDO is a quasi-particle describing the electron that is ionised, including relaxation and correlation effects [34, 62].

### 2.3.2 Time-independent Dyson Orbitals

Working in frequency domain, no propagation needs to be considered. Instead, the quantity of interest here is the stationary DO which corresponds to the TDDO at  $t = 0$ . From eq. 2.7 the DO can be interpreted as quasi-particle that is ejected by the irradiating light [34].

While for the TDDO only the general expressions were shown, in this section, since the time-independent DO formalism is used within this work, a more detailed derivation of the expressions is done.

The main advantage of this formalism in frequency-domain becomes clear when the photoelectron cross-section is considered. In the Fermis' Golden Rule [30] formulation, which assumes the wavelength to be much larger than the characteristic size of the system under study and weak irradiating light-field, the cross-section for the transition between an initial  $i$  and final  $k$  states is in atomic units [32, 97]

$$\sigma(\epsilon) = \frac{2}{3} \sum_k (\epsilon + E_k - E_i) \left| \langle \Psi_i^N | \hat{\mathbf{d}} | \Psi_k^N \rangle \rho(\epsilon) \right|^2 \propto \sum_k |\mathbf{D}_k|^2 \quad (2.8)$$

where  $\epsilon = h\nu - (E_k - E_i)$  is the kinetic energy of the photoelectron that is determined by the photon energy  $h\nu$  and the energies  $E_\alpha$  of the initial unionised state  $|\Psi_i^N\rangle$  and the final ionised state  $|\Psi_k^N\rangle$  which includes all electrons, further  $\mathbf{D}_k = \langle \Psi_i^N | \hat{\mathbf{d}} | \Psi_k^N \rangle$  is the transition dipole moment and  $\rho(\epsilon)$  is the density of final states which is in the following assumed to be a delta function. Writing the initial and final states each as SDs

$$|\Psi_i^N\rangle = \hat{A}_N |\Phi_{i,1} \dots \Phi_{i,N}\rangle \quad (2.9a)$$

$$|\Psi_k^N\rangle = \hat{A}_N |\Phi_{k,1} \dots \Phi_{k,N-1} \Psi_k^{\text{el}}\rangle \quad (2.9b)$$

where  $\hat{A}_N$  is an  $N$ -electron antisymmetrisation operator,  $|\Phi_{k,j}\rangle$  are the  $j$ -th (Kohn-Sham) orbitals and  $\Psi_k^{\text{el}}$  is the FEF. The index  $k$  enumerates the final states which can have an arbitrary electron configuration here. The dipole operator  $\hat{\mathbf{d}}$  is a one-electron operator that can be written as  $\hat{\mathbf{d}} = \sum_{j=1}^N \hat{\mathbf{d}}_j$  where  $\hat{\mathbf{d}}_j = \mathbf{r}_j$  in length gauge or  $\hat{\mathbf{d}}_j = \nabla_j / (\epsilon + E_k - E_i)$  in velocity gauge respectively [97].

Using the SD representations (2.9), the integral  $\mathbf{D}_k$  in eq. (2.8) can be written as

$$\mathbf{D}_k = \langle \Phi_{i,1} \dots \Phi_{i,N} | \hat{A}_N \sum_{j=1}^N \hat{\mathbf{d}}_j \hat{A}_N | \Phi_{k,1} \dots \Phi_{k,N-1} \Psi_{\text{el}} \rangle, \quad (2.10)$$

where hermiticity of the antisymmetrisation operator is used. The expression (2.10) can be further expanded taking into account that  $\hat{A}_N$  commutes with the dipole operator and making use of the relation  $\hat{A}_N \hat{A}_N = \sqrt{N!} \hat{A}_N = \sum_P (-1)^p \hat{P}$  where the sum goes over all permutations  $\hat{P}$  of electron indices with parity  $p$

$$\mathbf{D}_k = \sqrt{N!} \sum_P (-1)^p \sum_{j=1}^N \langle \Phi_{i,P(1)} \dots \Phi_{i,P(N)} | \hat{\mathbf{d}}_j | \Phi_{k,1} \dots \Phi_{k,N-1} \Psi_{\text{el}} \rangle \quad (2.11)$$

$$= \sqrt{N!} \sum_P (-1)^p \sum_{j=1}^N \langle \Phi_{i,P(j)} | \hat{\mathbf{d}}_j | \Phi_{k,j} \rangle \langle \Phi_{i,P(1)} | \Phi_{k,1} \rangle \dots \langle \Phi_{i,P(j-1)} | \Phi_{k,j-1} \rangle \quad (2.12)$$

$$\times \langle \Phi_{i,P(j+1)} | \Phi_{k,j+1} \rangle \langle \Phi_{i,P(N-1)} | \Phi_{k,N-1} \rangle \dots \langle \Phi_{i,P(N)} | \Psi_{\text{el}} \rangle \quad (2.13)$$

where  $P(j)$  is a permutation of the  $j$ -th orbital. Thereby the term  $j = N$  differs qualitatively from the others since the dipole operator acts on the FEF. Hence the sum can be reordered to obtain

$$\begin{aligned} \mathbf{D}_k &= \underbrace{\sqrt{N!} \sum_P (-1)^p \langle \Phi_{i,P(1)} | \Phi_{k,1} \rangle \dots \langle \Phi_{i,P(N-1)} | \Phi_{k,N-1} \rangle \langle \Phi_{i,P(N)} | \hat{\mathbf{d}}_j | \Psi_{\text{el}} \rangle}_{\langle \Psi_k^{\text{DO}} |} + \\ &\quad \underbrace{\sqrt{N!} \sum_P (-1)^p \sum_{j=1}^{N-1} \langle \Phi_{i,P(1)} | \Phi_{k,1} \rangle \dots \langle \Phi_{i,P(j-1)} | \Phi_{k,j-1} \rangle \langle \Phi_{i,P(j)} | \hat{\mathbf{d}}_j | \Phi_{k,j} \rangle \times} \\ &\quad \langle \Phi_{i,P(j+1)} | \Phi_{k,j+1} \rangle \dots \langle \Phi_{i,P(N-1)} | \Phi_{k,N-1} \rangle \langle \Phi_{i,P(N)} | \Psi_k^{\text{el}} \rangle \end{aligned} \quad (2.14)$$

where the first sum is denoted as DO and the second as conjugate DO respectively [65]. To reduce the large amount of integrals therein, the strong orthogonality approximation

is applied under the assumption that the overlap

$$\langle \Phi_{i,j} | \Psi_{\text{el}} \rangle = 0 \quad \forall j = 1, \dots, N \quad (2.15)$$

of the FEF with all bound states vanishes. This is strictly valid if  $|\Phi_{i,j}\rangle$  and  $|\Psi^{\text{el}}\rangle$  would correspond to the same Hamiltonian. But in most cases the relaxation of the orbital  $|\Phi_{i,j}\rangle$  is small, leading to a small but non-zero overlap with the FEF [47, 65]. Applying the strong orthogonality condition leads to the drop out of the second sum in eq.(2.14) and the transition dipole moment simplifies to

$$\begin{aligned} \mathbf{D}_k &= \sum_p (-1)^P \langle \Phi_{i,P(1)} | \Phi_{k,1} \rangle \dots \langle \Phi_{i,P(N-1)} | \Phi_{k,N-1} \rangle \langle \Phi_{i,P(N)} | \hat{\mathbf{d}}_j | \Psi_k^{\text{el}} \rangle \\ &= \langle \Psi_k^{\text{DO}} | \hat{\mathbf{d}}_j | \Psi_k^{\text{el}} \rangle \end{aligned} \quad (2.16)$$

**?? At the moment, there is no equation of the DO to reference. Write it differently?** which corresponds to the definition of the TDDO in eq.(2.7) for  $t = 0$  as mentioned above. The expression for the PES cross-section in the DO formalism simplifies to

$$\sigma(\epsilon) = \frac{2}{3} \sum_k (\epsilon + E_k - E_i) \left| \langle \Psi_k^{\text{DO}} | \hat{\mathbf{d}} | \Psi_{\text{el}} \rangle \right|^2. \quad (2.17)$$

In the derivation given above, it is assumed that initial and final states can be represented by single SD. In practice, states often are described by a linear combination of SDs with different electronic configurations. A respective generalisation of the DO is straight forward but introduces additional summations and thus leads to more complex terms [47].

### 2.3.3 Sudden Approximation

Further simplification of the DO formalism can be obtained by applying the so-called sudden approximation (SA) where the computation of the FEF is omitted. In the SA it is assumed that the transition to the continuum with corresponding energy has a constant probability [102]. This can be justified for high kinetic energies where the oscillations of the FEF are much stiffer than the structures of bound states so that small changes in the energy of the FEF do not play an important role. Thus, the transition dipole moment (2.14) reduces to the scalar

$$D_k = \sum_p (-1)^P \langle \Phi_{i,P(1)} | \Phi_{k,1} \rangle \dots \langle \Phi_{i,P(N-1)} | \Phi_{k,N-1} \rangle \quad (2.18)$$

which involves only the bound  $N - 1$ -electron system [103]. With this assumption the kinetic energy of the free electron dependence of the PES is neglected, assuming error introduced is a similar factor for all transitions. This has shown to be a valid assumption if the nature and spacial extend of the Dyson orbitals is similar for different transitions. Note that the expression (2.18) corresponds to the nominator of the Greens' function in (2.3) and thus is the level of theory at which the Greens' function PES transitions are computed.

Finally, the expression (2.18) can be further simplified to get the approach described

in the introduction to this chapter, based on Koopmans' theorem. Therefore the electron relaxation is neglected and thus the  $N - 1$ -electron state can be written as  $|\Psi_k^{N-1}\rangle = \hat{a}_k |\Psi_i^N\rangle$ . Thus, the sum over all permutations  $\hat{P}$  in (2.18) reduces to the case  $\delta_{P(j),j}$  due to orthogonality of the orbitals. Moreover, due to the normalisation of the orbital functions, all transitions have a probability of one and thus corresponds to the scheme described earlier.

# 3 | Description of Free Particles

The description of unbound particles has several complications of conceptual and technical kind. In this chapter, different numerical methods are introduced that can be used to solve the one-electron SE in particular for FEFs. In section 3.1, the conceptual differences between bound and continuum states as well as the numerical treatment of the latter in a finite basis are discussed. Thereafter, in the sections 3.2 - 3.6, different numerical methods are introduced that can be used to solve the one-particle SE on a molecular domain.

## 3.1 Continuum Waves

Continuum waves are discussed only sparsely in lectures on quantum mechanics, even though their fundamental differences compared to bound states makes them an interesting object to study. The states considered here have a spatial infinite extend as it is well-known for plane waves

$$\Psi_{\mathbf{k}}^{\text{plan}}(\mathbf{r}) = \sqrt{\frac{|\mathbf{k}|}{(2\pi)^3}} e^{i\mathbf{k}\cdot\mathbf{r}} \quad (3.1)$$

with  $\mathbf{k}$  being the wave-vector as well as for spherical waves. Moreover, continuum wave functions are not square integrable and hence can not be normalised according to  $\int \Psi_{\mathbf{k}}^{\dagger}(\mathbf{r}) \Psi_{\mathbf{k}}(\mathbf{r}) d\mathbf{r} = 1$  and thus the probability interpretation is invalid [104]. Instead, these functions are sharp in a continuous variable (namely the momentum) and hence should rather be interpreted as probability densities, suggesting the normalisation  $\int \Psi^{\dagger}(\mathbf{r}) \Psi(\mathbf{r}') d\mathbf{r} = \delta(\mathbf{k} - \mathbf{k}')$  where  $\delta(\mathbf{k})$  is the Dirac delta distribution [104, 105]. This property distinguishes the analytical FEF from those obtained with numerical methods that often have a finite support and are obtained from an approximate Hamiltonian matrix which has no continuous spectrum due to finiteness of its basis. Especially the difference in the normalisation of wave functions and by this in the dimensionality of overlap integrals also affects the integral evaluated when calculating the transition dipole matrix elements [106]. However, the Stieltjes imaging approach described in section 3.1.1 gives a formal verification for the use of square-integrable function for the approximation of a continuum state. Moreover, it provides a formalism to enhance the quality of spectra obtained with numerical methods.

A further aspect of numerical treatment of continuum functions that is only sparsely discussed in literature concerns the question of the physical interpretation of the numerical solution **Can one expect some theory about it?**. When dealing with approximate continuum functions, it is often assumed that the analytic function of interest  $|\Psi_a(\mathbf{k})\rangle$  is approximated by that particular numeric solution  $|\Psi_n(\mathbf{k}')\rangle$  which is closest in energy to the desired one [26] **more sources: ideas?**. An alternative interpretation would be to assume that the

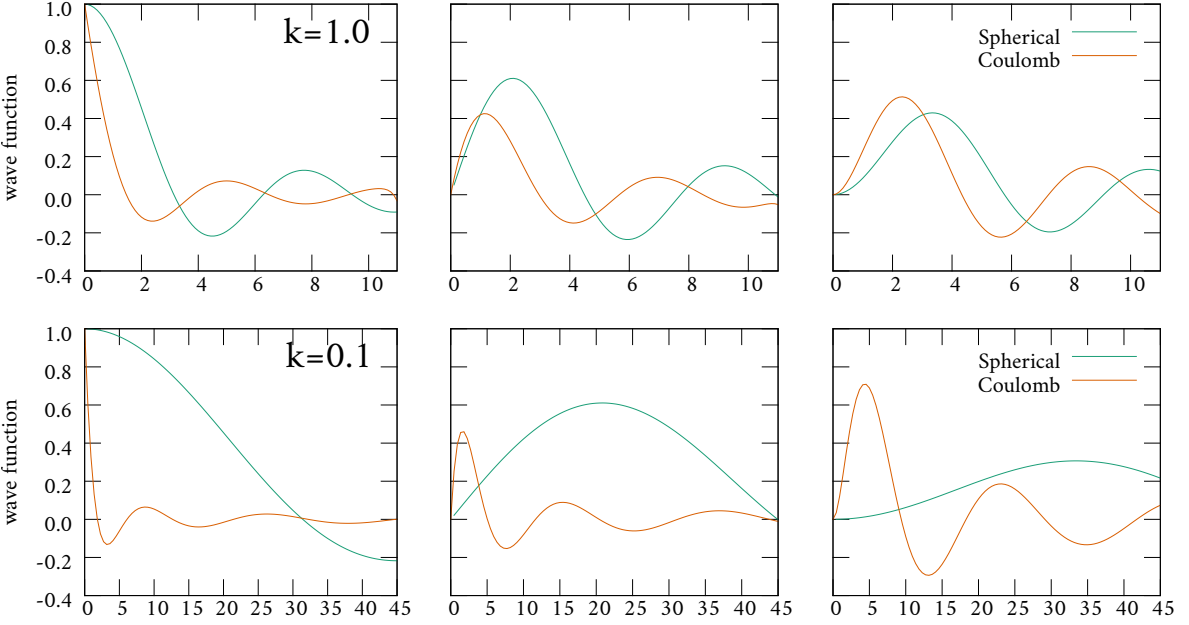


Figure 3.1: Radial part of spherical waves and Coulomb waves (confluent hypergeometric function approximated with 55 terms each) for  $l = 0$  (left),  $l = 1$  (centre) and  $l = 2$  (right). The Coulomb waves are not normalised.

numerical solution corresponds to an approximation to  $|\Psi_n\rangle \approx \frac{1}{k^+ - k^-} \int_{k^-}^{k^+} |\Psi_a(k)\rangle dk$  which would change its interpretation and normalisation.

In other works simulating PES in frequency domain only sparsely explicit calculations on the FEF are obtained [26, 105]. Instead, mainly two different representations of the photoelectron are found which are based on plane-wave expansions in spherically symmetric bases [34, 35, 107]. One of the expansions is that in spherical waves [33]

$$\Psi_{\mathbf{k}}^{\text{Sph}}(\mathbf{r}) = 4\pi \sum_{l=0}^{\infty} \sum_{m=-l}^l i^l j_l(kr), Y_l^m(\theta, \phi) Y_l^{\dagger, m}(\theta_k, \phi_k) \quad (3.2)$$

where  $k = |\mathbf{k}|$  and  $r = |\mathbf{r}|$  are the lengths of the wave vector  $\mathbf{k}$  and spatial vector  $\mathbf{r}$ , respectively,  $j_l(kr)$  are spherical Bessel functions that solve the radial SE (eq. (2.5) with  $V(r) = 0$ ) and the arguments to the spherical Harmonics  $Y_l^m(\theta, \phi)$  and  $(\theta_k, \phi_k)$ , are the angles of the spherical coordinate system in real-space and Fourier-space, respectively [34]. Another expansion of a plane wave often used is that in Coulomb waves

$$\begin{aligned} \Psi_{\mathbf{k}}^{\text{Coul}}(\mathbf{r}) = & \frac{1}{(2\pi)^{\frac{3}{2}}} \sum_{l=0}^{\infty} \sum_{m=-l}^l i^l (2kr)^l e^{-\pi \frac{Z}{2k}} \frac{|\Gamma(l+1+i\frac{Z}{k})|}{\Gamma(2l+2)} \\ & e^{ikr} F_1(l+1-i\frac{Z}{k}, 2l+2, 2ikr) Y_l^m(\theta, \phi) Y_l^{\dagger, m}(\theta_k, \phi_k) \end{aligned} \quad (3.3)$$

where  $Z$  is the charge of the nucleus and  $F_1$  is the confluent hypergeometric function of the first kind [107, 108]<sup>1</sup>.

A third expansion that is available *e.g.* in the program ezDyson [34] is an asymptotic

---

<sup>1</sup>  $F_1(\alpha, \gamma, z) = 1 + \frac{\alpha}{\gamma} z + \frac{\alpha(\alpha+1)}{\gamma(\gamma+1)} \frac{z^2}{2!} + \dots$

Coulomb wave expression for vanishing momentum in which the confluent hypergeometric function can be approximated by a Bessel function as

$$\lim_{k \rightarrow 0} F_1(l + 1 + \frac{i}{k}, 2l + 2, 2ikr) = (2l + 1)!(2r)^{-l-\frac{1}{2}} J_{2l+1}(\sqrt{8r}) \quad (3.4)$$

where  $Z = -1$  is assumed and  $J_{2l+2}(x)$  is the Bessel function that is connected to the spherical Bessel functions  $j_l(x)$  via the relation  $j_l(x) = \sqrt{\frac{\pi}{2x}} J_{l+\frac{1}{2}}(x)$  [33]. This case is separately available in `ezDyson` [34].

The spherical Harmonics [109] moreover have the form

$$Y_l^m(\theta, \phi) = (-1)^{(m+|m|)/2} i^l \sqrt{\frac{2l+1}{4\pi} \frac{(l-|m|)!}{(l+|m|)!}} P_l^{|m|}(\cos(\theta)) e^{im\phi} \quad (3.5)$$

where  $P_l^m(x)$  are associated Legendre polynomials [33]. The spherical harmonics are orthonormalised according to

$$\int Y_l^{\dagger m}(\phi, \theta) Y_{l'}^{m'}(\phi, \theta) d\mathbf{r} = \delta_{l,l'} \delta_{m,m'} \quad (3.6)$$

and have the property

$$\int Y_l^{\dagger m}(\phi, \theta) \mathbf{r} Y_{l'}^{m'}(\phi, \theta) d\mathbf{r} = \delta_{l,l' \pm 1} C_{l,l',m,m'} \quad (3.7)$$

if not both  $l$  and  $l'$  are 0 where  $C_{l,l',m,m'}$  are Clebsch-Gordan coefficients. The relation (3.7) governs the dipole transition probabilities of molecular systems.

Both expansions (3.2) and (3.3) do not take the molecular potential into account but give an easy picture for the photoelectron. Since the spherical wave basis is obtained under the assumption of no potential  $V(\mathbf{r})$ , this is assumed to be a good approximation for photodetachement when the initial state is neutral whereas the Coulomb wave expansion takes into account the ESP of the remaining anion at larger distances to the molecule and thus is more reasonable for ionised remainder systems [107]. Due to these obvious deficiencies of the inflexible expansions, some modifications are used by several authors which involve the choice of an effective charge  $Z^* < 1$  in the expansion (3.3) [107] and an orthogonalisation of the expansion with respect to the DO [107, 110–112]. The latter can be shown to be equivalent to a respective shift of the expansion centre such that the expectation value of the dipole moment of the DO vanishes [110].

In this work the spherical waves (3.2) are used as reference basis for the computed solutions for an easier interpretation and comparison of different results. To do so, the numerically obtained solution  $|\Psi_n\rangle$  is projected onto spherical waves for different  $l$  and  $m$  which will be referred to as partial wave coefficient.

In addition to the previously discussed questions about the relation of analytic and numeric FEFs, the infinite degeneracy of the analytical solutions has no numerical counterpart and thus leads to problems which are discussed on the example of the ionisation of a hydrogen-like atom whose analytical FEF is of the form (3.3) but with arbitrary coefficients for each term whose only prerequisite is that their squares add up to one [33].

The Coulomb wave basis is, given its energy  $E = \frac{1}{2}|\mathbf{k}|^2$ , infinitely degenerate in the

direction of  $\mathbf{k}$  as well as in the quantum numbers  $l$  and  $m$ . However, the coefficients of the physically observable FEF are determined by the matrix elements of the dipole operator with the DO (2.16). Considering the ionisation of hydrogen in its ground state, the FEF is in one of the three  $p$ -waves because the probability to access any of the other vacuum-states with the correct energy vanishes due to dipole selection rules eq. (3.7) for spherically symmetric systems.

Unfortunately, as shown in section 6.1, the considerations made above are not true for the numerical solution anymore where a finite set of superpositions is obtained which, due to numerical treatment, differ in energy and thus can not be assigned to a common value of  $\mathbf{k}$ . Choosing the energetically best-fitting solution though might in principle result in a function with vanishing contribution of the  $p$ -type orbitals whereas, for a slightly changed computational scheme or target energy it could yield a solution with large  $p$ -contributions and high intensity, respectively.

### 3.1.1 Stieltjes Imaging

The Stieltjes imaging [106, 113–115] provides an elegant way to use the numerically obtained FEFs of a discrete character lying above the ionisation threshold for PES calculations. To correct on the different character of the spectrum and the smaller extend of the numerically obtained solution, the Stieltjes imaging approach uses spectral moments [116]

$$\mu_n = \int_0^\infty \epsilon^n df(\epsilon) \quad (3.8)$$

where  $n < 0$  denotes the order of the moment,  $\epsilon = E - E_0$  is the transition energy and

$$\frac{df}{d\epsilon} = \frac{2}{3}(E - E_0) \left| \langle \Psi_0 | \hat{\mathbf{d}} | \Psi_f \rangle \right|^2 \quad (3.9)$$

is the oscillator strength with the dipole operator  $\hat{\mathbf{d}}$ , the energies  $E_0$  and  $E$  of the ground state  $|\Psi_0\rangle$  and final state  $|\Psi_f\rangle$ , respectively. Since the final state can be of bound state character  $|\Psi_\alpha\rangle$ , where the energies are discrete, as well as of continuous character  $|\Psi_\varepsilon\rangle$  with continuous spectrum, one can rewrite the spectral moment (3.8) as [113]

$$\mu_n = \sum_{\alpha} (E_{\alpha} - E_0)^n \left| \langle \Psi_0 | \hat{d} | \Psi_{\alpha} \rangle \right|^2 + \int_0^\infty \varepsilon^n \left| \langle \Psi_0 | \hat{d} | \Psi_{\varepsilon} \rangle \right|^2 d\varepsilon \quad (3.10)$$

where  $\varepsilon$  denotes the kinetic energy of the FEF. Since, in contrast to the analytic case (3.10), the numeric Hamiltonian has a discrete spectrum, the respective spectral moments here are of the form

$$\mu_n = \sum_{j=0}^N (E_j - E_0) \left| \langle \Psi_0 | \hat{d} | \Psi_j \rangle \right|^2 \quad (3.11)$$

where  $N$  denotes the number of eigenfunctions  $|\Psi_j\rangle$  and the sum accounts for the bound as well as unbound states [106, 114]. Assuming that the first  $2l - 1$  spectral moments can be restored by the numerical Hamiltonian in good approximation, they can be used to

obtain a histogram representation of the cross section of the form

$$\sigma(\varepsilon) = \frac{2}{3} \frac{df}{d\varepsilon} = \frac{2}{3} \begin{cases} 0 & 0 < \varepsilon < \varepsilon_1(l) \\ \frac{1}{2} \frac{(f_i + f_{i+1})}{\varepsilon_{i+1} - \varepsilon_i} & \varepsilon_j(n) < \varepsilon < \varepsilon_{j+1}(l) \\ 0 & \varepsilon_n(l) < \varepsilon \end{cases} \quad (3.12)$$

where  $(\varepsilon_i, f_i)_{i=1,\dots,l}$  are a principal pseudo spectrum [114]. The values  $\varepsilon_i$  and  $f_i$  are obtained from an eigenvalue equation of a symmetric tridiagonal matrix whose diagonal elements  $\alpha_i$  and off-diagonal elements  $\beta_i$  can be found as parameters a function

$$I(z) = \frac{\beta_0^2}{z - \alpha_1 - \frac{\beta_1^2}{z - \alpha_2 - \dots - \frac{\beta_{l-1}^2}{z - \alpha_l}}} \quad (3.13)$$

which contains the full information about the first  $2l - 1$  spectral moments and has the alternative form [117]

$$I(z) = \frac{\mu_0}{z} + \frac{\mu_1}{z^2} + \dots + \frac{\mu_{2l-1}}{z^{2l}} \quad (3.14)$$

where  $\mu_i$  are the spectral moments (3.11) [117]. The key task in Stieltjes imaging is the transformation from the form (3.14) to (3.13) [117].

In practice, the Stieltjes imaging is very demanding if energetically narrow transitions occur since many terms in expression (3.11) are needed for convergence, making this method efficient mainly for low energy range [26].

## 3.2 Finite Differences and Finite Volumes

The most common and straightforward approach to solve differential equations such as the SE numerically is via the so-called finite difference (FD) scheme. Starting from the one-particle SE in atomic units

$$\left( -\frac{1}{2} \nabla^2 + V(\mathbf{r}) \right) \Psi(\mathbf{r}) = E \Psi(\mathbf{r}) \quad (3.15)$$

where  $V(\mathbf{r})$  is an arbitrary potential at this point. Considering a general problem where the low symmetry does not support a product ansatz as *e.g.* eq. (2.4) which reduces the dimensionality and thus the complexity of the problem, the kinetic energy operator has in a matrix representation at least 6 off-diagonal terms per line whose non-banded structure requires iterative solvers [118]. An important disadvantage of finite difference schemes is that they require the evaluation points to be on a regular grid whose stepsize is governed by the sharpest features in the system while local refinement is hardly available. If considering molecules and thus Coulomb-shaped potentials  $V(\mathbf{r})$ , the finest structures are expected to be close to the nuclei whereas at larger distances a respectively dense grid is not needed and thus computations of FEFs with a reasonable box size become very expensive [97]. Nonetheless, there are applications of this scheme to the SE [118, 119], some of them with massive parallelisation using MPI and multiple GPUs [120].

To overcome this bottleneck for systems with non-uniform parameters, often the finite volume method is used. The finite volume method is an integral method that is not

based on a regular grid. Instead, for the estimation of the kinetic energy Gauß's theorem  $\int_V \nabla \mathbf{u}(\mathbf{r}) dV = \int_S \mathbf{u}(\mathbf{r}) \mathbf{n} dS$  is used where  $\mathbf{u}(\mathbf{r})$  is a vector-valued function and  $\mathbf{n}$  is the normal vector on the surface  $S$  of the volume  $V$  under consideration. Chosing  $\mathbf{u}(\mathbf{r}) = \nabla \Psi(\mathbf{r})$  yields the relation

$$\nabla^2 \Psi(\mathbf{r}) = \lim_{V \rightarrow 0} \frac{\int_{\partial V} \nabla \Psi(\mathbf{r}) \mathbf{n} dS}{V}. \quad (3.16)$$

This scheme becomes especially interesting when the finite volume elements are chosen to be Voronoi cells [121]. A Voronoi-tesselation is associated with a grid and is constructed such that the Voronoi cell  $T_i$  consists of all points in space that are closer to the point  $i$  than to any other points in the grid, see Figure 3.2 [122–124].

This description has the advantage that the quantities on the right-hand side of (3.16) can be associated with properties of the Voronoi-Cell, leading to the first-order approximation of the kinetic energy

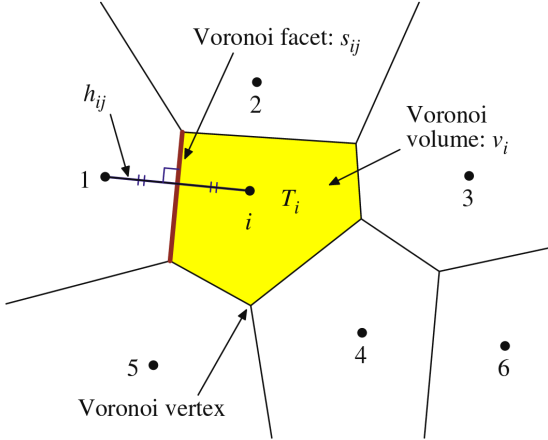


Figure 3.2: 2-dimensional Voronoi diagram on an arbitrary distribution of seven points [125].

$$\nabla^2 \Phi(\mathbf{r}_i) = \frac{1}{v_i} \sum_j^{\text{neighbours}} \frac{\Psi(\mathbf{r}_j) - \Psi(\mathbf{r}_i)}{h_{ij}} s_{ij} a \quad (3.17)$$

where  $v_i$  is the volume of the  $i$ -th Voronoi-cell (yellow area in Figure 3.2),  $h_{ij} = |\mathbf{r}_i - \mathbf{r}_j|$  is the distance between the centres of the  $i$ -th and  $j$ -th Voronoi-cells (bold black line) and  $s_{ij}$  is the area of the common facet of the  $i$ -th and  $j$ -th Voronoi cells (red line in Figure 3.2).

Such a scheme is applied, *e.g.*, by Son and Chu [121, 125] to the time-dependent SE, studying multi-photon ionisation of several molecular systems.

### 3.3 Pseudospectral Methods

Under the term (pse)udospectral methods a large group of methods is comprised which treat the differential equation of interest variationally using an orthogonal basis  $\{\varphi_i(\mathbf{r})\}$ , hence seeking for a solution of the form

$$\Psi(\mathbf{r}) = \sum_i^n c_i \varphi_i(\mathbf{r}) \quad (3.18)$$

where  $c_i$  are coefficients to be found [126]. In the pseudospectral methods the basis functions  $\varphi_i(\mathbf{r})$  are smooth global functions, *e.g.*  $\varphi_k(\mathbf{r}) = e^{ik\mathbf{r}}$ , resulting in the Fourier space [127]. Alternatively Jacobi, Chebychef or Legendre polynomials are commonly used [128].

To find the corresponding coefficients, the problem is solved on a grid, leading to a linear system of equations. Depending on the technique used for determining the coefficients, it can be seen as a high-order FD or high-order FEM. One prominent advantage of this class of methods is that the error of the solution  $\psi(\mathbf{r})$  usually decays exponentially with the number  $n$  of basis functions and the grid can be chosen coarsely, making the numerical scheme very efficient [128, 129]. In addition, many formulations allow for an implementation making use of the fast fourier transform [128].

A special representative subgroup of the pseudospectral methods are the so-called discrete variable representation (DVR) schemes which are frequently used to study electronic structure and vibrational problems in molecules [101, 130, 131]. Since this scheme is applicable in one dimension only, often symmetry-adapted coordinates such as spherical coordinates are used product functions such as (2.4) are applied.

The basis functions used in this scheme commonly are Lagrange polynomials [98, 130, 131] whose nodes are chosen by a general Gauß quadrature rule [130] or from a quadrature rule for the radial Coulomb function which is in particular popular whene electronic structure problems are considered [129, 131]. Even if the DVR provides a flexible and fast-convergent basis, an extension to higher dimensionality can only be achieved by a product ansatz and thus is applicable to problems with high symmetry.

Moreover, as for the other pseudospectral methods, the system matrices are dense and thus the solution is numerically expensive. This is at least partially solved by using a hybrid scheme of the finite element and DVR scheme where the DVR scheme is used on small segment only, connected by single bridge-functions each [98, 130].

## 3.4 Radial Basis Functions

The radial basis function (RBF) technique is based on an arbitrary point distribution with very general properties. The ansatz functions  $\varphi_i(\mathbf{r})$  used in this technique need to be spherically symmetric, *i.e.*  $\varphi_i(\mathbf{r}) = \varphi_i(|\mathbf{r}|)$  and are placed at the grid points on a given domain. The RBF-scheme is used not only for solving differential equations but is also a usefull tool for interpolation of scattered data in arbitrary dimensions [132] and surface reconstruction from scattered data [133].

Among the commonly used functions are, besides linear and cubic ones, multiquadratic ( $\sqrt{r^2 + r_0^2}$ ), inverse multiquadratic ( $(r^2 + r_0^2)^{-\frac{1}{2}}$ ) and Gaussian ( $\exp(-\frac{r^2}{2r_0^2})$ ) functions are to be mentioned where  $r_0$  is the radius, respectively [134, 135].

If the parameter  $r_0$  is chosen reasonably, the scheme is numerically stable and fast convergeing [134], but the choise of  $r_0$  can be non-trivial especially for highly non-regular grids where a good quality of the representation between two points with a large distance require a respectively large radius  $r_0$  whereas too large radii can make the scheme numerically instable for close-lying points. Moreover the resulting system matrices are dense due to the global definition of the ansatz functions, making it computationally expensive when large domains are considered.

## 3.5 Finite Elements

In the FEM the differential equations to be solved are formulated in their weak form which is an integro-differential equation and can be understood as a generalisation of the differential equation [36]. Starting with the well-known (strong) form of the SE defined on a domain  $\Gamma$  in atomic units which are used here and in the following chapters

$$-\frac{1}{2}\nabla^2\Psi(\mathbf{r}) + V(\mathbf{r})\Psi(\mathbf{r}) = E\Psi(\mathbf{r}) \quad \mathbf{r} \in \Gamma \quad (3.19)$$

with the condition

$$\Psi(\mathbf{r}) = 0 \quad \mathbf{r} \in \partial\Gamma \quad (3.20)$$

for the boundary domain  $\partial\Gamma$  which is assumed to be Lipschitz continuous. The first term in equation (3.19) corresponds to the kinetic energy and  $V(\mathbf{r})$  is a potential that is not further specified at this point. The unknowns of this equation are the wave function  $\Psi(\mathbf{r})$  and respective energy  $E$ . To bring equation (3.19) into the weak form, it is first multiplied by the complex conjugate of a test function  $\Phi(\mathbf{r})$  which fulfils the same boundary conditions and needs to be differentiable. In the second step, one integrates over the whole space of interest resulting in the equation

$$\int d\mathbf{r} \left( -\frac{1}{2} (\nabla^2\Phi^*(\mathbf{r})) \Psi(\mathbf{r}) + V(r)\Phi^*(\mathbf{r})\Psi(\mathbf{r}) \right) = E \int d\mathbf{r} \Phi^*(\mathbf{r})\Psi(\mathbf{r}). \quad (3.21)$$

The kinetic energy term can be symmetrised using Green's first identity  $\int_{\Gamma}(\nabla^2\Psi)\Phi^*d\mathbf{r} = \int_{\partial\Gamma}(\nabla\Psi)\Phi^*ds - \int_{\Gamma}(\nabla\Psi)(\nabla\Phi^*)d\mathbf{r}$  to obtain the final expression

$$\int_{\Gamma} d\mathbf{r} \left( \frac{1}{2} (\nabla\Phi^*(\mathbf{r})) (\nabla\Psi(\mathbf{r})) + V(r)\Phi^*(\mathbf{r})\Psi(\mathbf{r}) \right) = E \int_{\Gamma} d\mathbf{r} \Phi^*(\mathbf{r})\Psi(\mathbf{r}) \quad (3.22)$$

$$\Phi(\mathbf{r}) = 0 \quad \Psi(\mathbf{r}) = 0 \quad \mathbf{r} \in \partial\Gamma \quad (3.23)$$

which is denoted as the weak form of the SE. A function  $\Psi(\mathbf{r})$  is considered as a solution of (3.22) if the equation holds for any test function  $\Phi(\mathbf{r})$ . Since usually only real-valued bases functions are used, in the literature the complex conjugation is omitted. Moreover, from a mathematical point of view, since  $\Phi(\mathbf{r})$  is an arbitrary function, complex conjugation does not change anything here but it will be shown later that it is more reasonable from a physical point of view if the weak formulation is defined as given in equation (3.22).

The weak formulation (3.22) has two main changes in its properties compared to the strong formulation (3.19). The first is that any solution of (3.19) solves (3.22) while the space of solutions of the weak form is larger since only first derivatives need to be defined, which lead to the terms weak and strong respectively. In addition, a weak solution is defined only up to a cardinal number of zero; hence changing the values of a given solution  $\Psi(\mathbf{r})$  along a finite number of planes in three dimensions yields a function that still solves (3.22). These properties play an important role here since they allow *e.g.* the use of piecewise linear basis functions as they are commonly used in the FEM scheme which do not have a second derivative and whose first derivative is undefined on certain planes.

As usual for numerical methods, in the FEM scheme one restricts the search for solutions to a subspace spanned by a finite set of test functions for both  $\Psi(\mathbf{r})$  and  $\Phi(\mathbf{r})$ ,

leading to the Petrov-Galerkin scheme. To get best flexibility for the wave function, the domain  $\Gamma$  is subdivided into finite volume elements with a close packing. These volume elements, denoted as finite elements, give this method its name. Having this subdivision of space, the ansatz (basis) functions  $\varphi(\mathbf{r})$  used to construct  $\Psi(\mathbf{r})$  and  $\Phi(\mathbf{r})$  are defined as piecewise polynomials being non-zero only on one or few elements.

Considering  $\Gamma$  to describe a 2D-plane, the elements can be, for example, triangles as shown in Figure 3.3. Enumerating the vertices of the triangles as  $\mathbf{r}_i i = 1, \dots, N$ , the piecewise linear (Lagrange-) basis functions are defined as

$$\varphi_i(\mathbf{r}_j) = \begin{cases} 1 & j = i \\ 0 & j \neq i \end{cases} \quad (3.24)$$

resulting in two-dimensional “hat” functions as depicted in Figure 3.3 for an index  $i$ . This definition of a

basis ensures continuity of the solution over  $\Gamma$  while the first derivatives are continuous only within each element. To assure continuity of the first derivatives as well, second order polynomials are needed. At the border of  $\Gamma$ , respectively truncated

“hat” functions are used whose coefficients are given by the boundary condition.

As usual in variational schemes, the wave function of interest is constructed as a linear combination of these basis functions  $\Psi(\mathbf{r}) = \sum_i c_i \varphi_i(\mathbf{r})$  where  $c_i$  are weighting coefficients. The test functions are chosen from the same space of ansatz functions, testing each basis separately  $\Phi(\mathbf{r}) = \varphi_j(\mathbf{r}), j \in 1, \dots, N$ . Hence, the SE (3.22) with the finite basis reads

$$\sum_i \int d\mathbf{r} \left( \frac{1}{2} (\nabla \varphi_i(\mathbf{r})) (\nabla \varphi_j(\mathbf{r})) + V(r) \varphi_i(\mathbf{r}) \varphi_j(\mathbf{r}) \right) c_i = E \sum_i \int d\mathbf{r} \varphi_i(\mathbf{r}) \varphi_j(\mathbf{r}) c_i \quad \forall j \in \{1, \dots, N\} \quad (3.25)$$

which is the  $j$ -th component of the generalised matrix eigenvalue problem

$$\left( \frac{1}{2} \mathbb{A} + \mathbb{V} \right) \mathbf{c} = E \mathbb{M} \mathbf{c}. \quad (3.26)$$

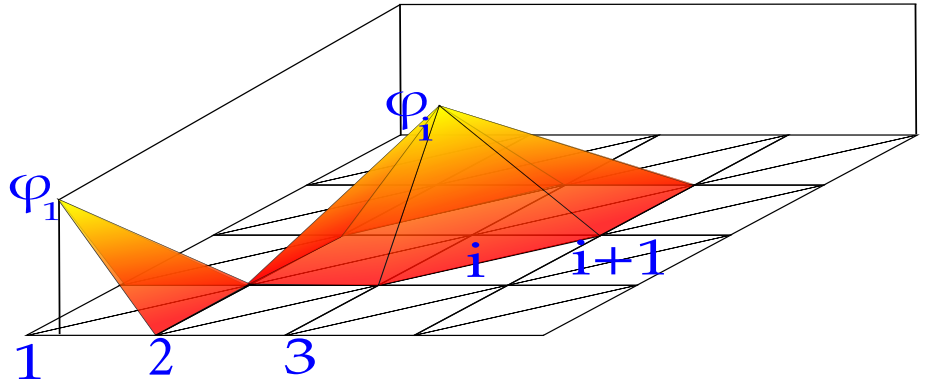


Figure 3.3: Example of finite elements in 2D of triangular shape and linear basis functions  $\varphi_i(\mathbf{r})$  defined on them.

with

$$\mathbb{A}_{ij} = \int d\mathbf{r} (\nabla \varphi_i(\mathbf{r})) (\nabla \varphi_j(\mathbf{r})) \quad \mathbb{V}_{i,j} = \int d\mathbf{r} V(\mathbf{r}) \varphi_i(\mathbf{r}) \varphi_j(\mathbf{r}) \quad \mathbb{M}_{i,j} = \int d\mathbf{r} \varphi_i(\mathbf{r}) \varphi_j(\mathbf{r}) \quad (3.27)$$

and the vector  $\mathbf{c}$  in equation (3.26) contains the coefficients  $c_i$  to be found.

The quality of this basis depends strongly on the size and shape of the finite elements: The stronger the solution varies, the smaller element sizes or higher order ansatz functions are required to be able to represent the wave function. Knowledge about ranges of sharp structures and areas with smooth variation of the wave function  $\Psi(\mathbf{r})$  hence is crucial for the setup of a good mesh.

In chapter 4 more details about the finite element formulation are given with a special focus on how to setup a grid that is well suited for describing free particles in quantum mechanics.

## 3.6 Wavelets

The wavelet method was developed in the 1980s [136] as a generalisation of the Fourier transform that combines the advantages of the Fourier space and the FEM. Similar to the FEM, it is based on a local basis but the wavelets have some characteristic scales similar to the wavelength in the Fourier basis, so that they can be used to decompose objects into features of different scales as a generalisation of the Fourier transform [136–138]. Even though wavelets possess very advantageous properties, they are to date not very well-established. The most prominent and widely distributed application of Wavelets is compression of data as used, for example, in the jpeg2000 standard [139].

In general, a wavelet is a basis of the function space  $L_p(\mathbb{R}^d)$  *i.e.*, the space of functions  $\phi(\mathbf{r})$  for which  $\int \phi(\mathbf{r})^p d\mathbf{r} < \infty$  where  $\mathbf{r} \in \mathbb{R}^d$  and  $p$  is a positive integer. A particular wavelet is defined by a finite set of orthonormal mother wavelets  $\varphi_i(\mathbf{r})$  for which a series of functions

$$\varphi_{i,j,\alpha}(\mathbf{r}) = m^{\frac{j}{2}} \varphi_i(\mathbb{M}^j \mathbf{r} - \boldsymbol{\alpha}) \quad (3.28)$$

with the matrix  $\mathbb{M}$  whose eigenvalues have modulus larger than one,  $m = |\det(\mathbb{M})|$  and the running indices  $j \in \mathbb{Z}$  and  $\boldsymbol{\alpha} \in \mathbb{Z}^d$  can be defined which span  $L_p(\mathbb{R}^d)$  [137]. In practice, this very general definition is often restricted by additional requirements such as orthogonality of  $\varphi_{i,j,\alpha}(\mathbf{r})$  or utilisation of only one mother-wavelet  $\varphi(\mathbf{r}) = \varphi_i(\mathbf{r})$ . For brevity, in the following only the space  $L_2(\mathbb{R})$  with  $\mathbb{M} = 2$  is considered which corresponds to the original definition of wavelets [140]. The most prominent representatives are the Daubechies wavelets that are shown in Figure 3.4 which are a set of orthogonal wavelets with compact support and increasing smoothness. Especially the first-order Daubechies wavelet, more commonly known as the Haar-wavelet, is famous and by far the easiest existing orthogonal wavelet basis. In contrast to most other bases, in principle no smoothness properties are required but are desired since the functions to be represented are usually smooth [141].

Besides their broad use in data compression and analysis, wavelet bases also provide a handy tool to solve partial differential equations and are found to have similar numerical properties as the FEM [138, 142]. When applying a wavelet basis to solve a partial differ-

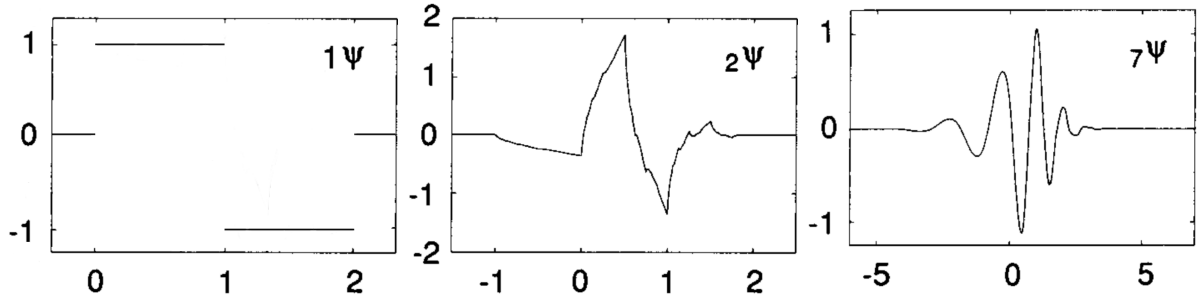


Figure 3.4: Daubechies wavelets of the orders 1, 2 and 7 (from left to right) [141].

ential equation, the weak form (3.22) is used [137]. However, not all wavelets form a valid basis for partial derivatives since, for example, the Haar-wavelet has a constant derivative of zero and the Daubechies-wavelet 2 (shown in Figure 3.4) is only semi-differentiable at some points [143]. However, the generality of the wavelet formulation allows to use problem-specific bases that are, *e.g.*, especially adapted to certain pseudo-differential operators, increasing the speed of convergence [137]. Finding such optimised bases in a systematic way is under current research and one can expect that they can be used for numerically stable, fast and accurate partial-derivative solvers [137, 144].

### 3.7 Hybrid Methods

In the previous sections a large variety of different methods are presented with different advantages and disadvantages which make them suitable for different applications. Moreover, there is a large number of approaches that combine the ideas of some of the above-mentioned methods to use the advantages of the respective methods together. In this section, several of these methods are presented which seem to be the most prominently used. One of the most prominent combinations of the above-mentioned methods is the FE-DVR scheme [98, 130] that was mentioned in chapter 2.2 already. In the FE-DVR scheme, a one-dimensional finite element scheme is used with comparatively large elements on which a DVR representation is used, but usually using the strong formulation of the respective partial-derivative equation. In this approach, more flexibility compared to the DVR scheme is obtained since in addition to the degree of polynomials in use, also the size of the elements can be varied which is especially advantageous for problems involving a Coulomb potential where the local kinetic energy varies strongly [101]. Moreover, the usually dense Hamiltonian and overlap matrix of DVR representation changes to a block-structure, with block being coupled to each other by single columns and rows [98]. A generalisation to multiple dimensions is the so-called spectral element used by several authors [145–147] for quantum mechanical problems. In contrast to the FE-DVR-scheme, it is based on the weak formulation and typically uses higher order Chebychev or Lagrange polynomials [145] and hence allows for larger elements than usual FEM. Thus, it can be also understood as a high order FEM scheme, combining the flexibility of FEM with the fast convergence of the pseudospectral basis. The spectral elements are found to be well suited for linear problems but require a complex implementation and lead to denser system matrices. The larger density in the resulting matrices in general leads to a reduced numerical stability and computationally more expensive solution strategies. Finally, com-

plex geometries usually benefit more from smaller elements than from higher order bases [148].

A successfull combination of spectral elements with the FEM is the so-called spectral difference method [149, 150]. In this scheme, a spatially uniform grid is used (as usual in the finite difference scheme) while employing a pseudospectral basis on the respective elements. The appealing properties of this method are an exponential convergence as known from finite difference methods by employing the sparseness of the equation system obtained in FEM [149]. More advanced methods based on the spectral difference schemes are available as well [150, 151] but are for brevity not discussed here in more detail.

# 4 | Finite Element Methods

As a conclusion of the previous chapter one can see that the number of methods that are currently available to describe a FEF in presence of an intricate electrostatic background potential is not that large. In this work, the method of choice to model the free electron function is the FEM which has been applied to quantum-mechanical problems by several authors [152–155]. However, to the best of my knowledge, only the bound state problems were addressed so far. A brief review of these works is given in section 4.1. Besides its large flexibility and computational efficiency pointed out in section 3.5, the large amount of available FEM libraries [56, 156–159] that are developed mainly for engineering problems is another advantage of practical importance due to the complexity of the generation of a suitable mesh, assembling of matrices and solution of matrix equations.

In the following chapter, the integration of the matrix elements (section 4.2) and set up of the mesh (section 4.3) will be described. Thereby the focus is put on the application to the one-particle SE that is to be solved with molecular electrostatic potential (ESP). Since the interest thereby is on free particle solutions, the spectrum is expected to be very dense and the wave function to be delocalised, requiring well-designed boundary conditions. A discussion of various boundary conditions and mimicing asymptotic behaviour available for FEM is described in section 4.4.

## 4.1 Finite Element Methods for Electronic Structure Calculations

The FEM is mainly known from engineering disciplines where it is used in a broad range of applications such as modelling of fluids [160, 161], heat transfer and flow [162–164] or material deformation under mechanical stress [165, 166]. However, also several different quantum-mechanical problems have been addressed with this method: electronic structure methods for small systems such as light atoms [152, 167–170] or diatomics [171], model oscillator systems [153] and solid state problems [172, 173]. Moreover, even Hartree-Fock [154] and DFT calculations on systems up to the size of benzene [155, 174, 175] have been performed, yielding results comparable to those obtained by the usual LCAO approach.

The above-mentioned applications have shown that the FEM is able to obtain reasonable results for molecular systems where the errors were comparable to those obtained with standard quantum-chemistry schemes even though their computational costs are higher. Here, usual quantum-chemical methods are more suited, since local basis functions localised on atoms are more convenient for bound problems. This suggests however that

the FEM should be a robust tool for the description of unbound states which represents a very non-trivial task for conventional techniques.

## 4.2 Setup of the Equation System

In section 3.5 the basics of the FEM were described and the generalised eigensystem shown in eq.(3.26) for the SE was derived. Here this is taken as starting point and a closer look at the computation of the matrix elements as well as solving strategies for the large sparse generalised eigenproblems are taken.

The generalised eigenproblem as given in eq.(3.26) consists of three matrices. Since the ansatz functions (shape functions)  $\varphi_i(\mathbf{r})$  have only a small support, most of the matrix elements are zero. However, in two and three dimensions no distinct band structure is achievable and the matrices are irreducible. Thereby matrix elements are zero when the elements involved are not neighboured as can be followed from Figure 3.3 where a linear basis function of a 2D-mesh is shown. The computation of the non-zero matrix elements involve an integration as, *e.g.*, the overlap integral  $\mathbb{M}_{i,j} = \int d\mathbf{r} \varphi_i(\mathbf{r}) \varphi_j(\mathbf{r})$  of ansatz functions. In practice these integrals are performed on a standard reference element and than scaled according to the Jacobian of the respective linear transformation that transforms the reference element to the physical one. Since these functions are the same for all elements, the evaluation of the integrals on the reference elements can be done via a lookup-table or an efficient numerical integration scheme whose order is given by the shape functions. The matrix elements  $\mathbb{A}_{i,j} = \int d\mathbf{r} (\nabla \varphi_i(\mathbf{r})) (\nabla \varphi_j(\mathbf{r}))$  consist of overlap integrals of known functions similar to those of  $\mathbb{M}$ . The only matrix containing system-specific information is the potential  $\mathbb{V}_{i,j} = \int d\mathbf{r} \varphi_i(\mathbf{r}) V(\mathbf{r}) \varphi_j(\mathbf{r})$  which requires numerical integration involving a reasonable approximation to  $V(\mathbf{r})$  which can be obtained via interpolation of known points or using exact values computed at the given quadrature points.

After assembling the matrices the eigenpair  $(e_i, \mathbf{c}_i)$  of the system

$$\left( \frac{1}{2} \mathbb{A} + \mathbb{V} \right) \mathbf{c}_i = e_i \mathbb{M} \mathbf{c}_i \quad (4.1)$$

need to be found, where the energy  $e_i$  is the closest to the target kinetic energy of the photoelectron. Since matrices with dimensions of several thousands typically occur, numerous schemes have been developed to solve them efficiently [176–179], and are described in section 4.5. Despite the numerical complexity because of the high dimensionality of this problem (several thousands of basis functions) the second problem is due to the fact that the eigenenergies  $e_i$  are expected to be close to each other since the corresponding exact Hamiltonian has a continuous spectrum in this energy range. It is well known in numerics that this leads to instabilities especially for the eigenvectors, making a regularisation of the problem (described in section 4.5.2) indispensable.

## 4.3 Element Types and Mesh Types

Among the FEM formulations several flavours were designed for different purposes. Given a certain equation to be solved in FEM, there are in general two systematic ways to

increase the accuracy. The first way is to increase the number of elements which is referred to as the  $h$ -FEM approach [42]. The refinement of the mesh is in principle always possible but technically demanding since it is not known in which regions of a mesh are too coarse in general [42]. To overcome this, some FEM implementations such as that of **Libmesh** [56] which is used here, provide an iterative mesh refinement scheme, adapting the mesh using local error estimations and thus is fully automatic [56]. However, these schemes are numerically demanding and hence can be only applied to benchmark systems.

The second strategy is called  $p$ -FEM. In the  $p$ -FEM scheme, the order  $p$  of the test functions is increased, resulting in smoother and more flexible solutions at the price of incrementing dimensionality [180]. Standard FEM-libraries usually have only  $p = 1, 2$  implemented, but high-order polynomials are also reported [158]. Combined schemes where the grid-size as well as the element order are adapted is referred to as  $hp$ -FEM [181]. These schemes are in principle promising but require detailed knowledge about the solution to setup the parameters reasonable in order to keep the computational demands in a feasible range.

Besides different refinement strategies, finite element types also vary in the way in which global smoothness is ensured and the numerical integration is obtained. While for Lagrange elements the shape functions are evaluated at certain inner or boarder points, *e.g.* in Argyris or Hsieh-Clough-Tocher elements also first or even second derivatives are evaluated [38, 182]. Moreover, one distinguishes conforming and the more general non-conforming meshes [183]. In case of the latter, more general structures are supported as *e.g.* hanging nodes which occur when a vertex of one element is on the edge of another as illustrated in Figure 4.1a [38]. The setup of the mesh is, as mentioned above already, critical to the quality of the solution and hence of special importance. Moreover, it is technically non trivial to set up a close packing of volume elements with the desired properties in a systematic way. Although in principle any element shape can be chosen, in three dimensions only tetrahedral (simplex), prism- and pyramid-shaped as well as hexahedral elements commonly are used. By choosing the element shape and the polynomial order, the element type of shape functions are fully defined.

When considering meshes to describe molecular properties it is clear that the element size should be smaller in the vicinity of the nuclei while it may be larger at longer distances. One way to create a hexahedral mesh with local refinement is to start with a coarse uniform lattice and subdivide the hexahedra where necessary as shown in Figure 4.1a for a benzene molecule. Another way is to setup small regular cubic grids around the nuclei and expand them radially in boxes of growing size as shown in Figure 4.1b. These brick-shaped elements however have the disadvantages that the regular cube-like structures therein might be not well-suited for atoms and molecules having higher symmetries.

Another approach used by Lehtovaara *et al.* [174] is to put layers of polyhedra around the atoms with increasing number of vertices and size. Thereby the overlapping regions of these polyhedra are removed by excluding the vertices that are closer to a different atom. The mesh obtained with this procedure for a benzene molecule [155] is shown in Figure 4.1c.

When restricting oneself to tetrahedral elements, other design principles are possible: Since they are simplexes in three dimensions, they can be designed from general grids using, *e.g.*, Voronoi [122] or Delaunay [184] tessellations from a set of points with the re-

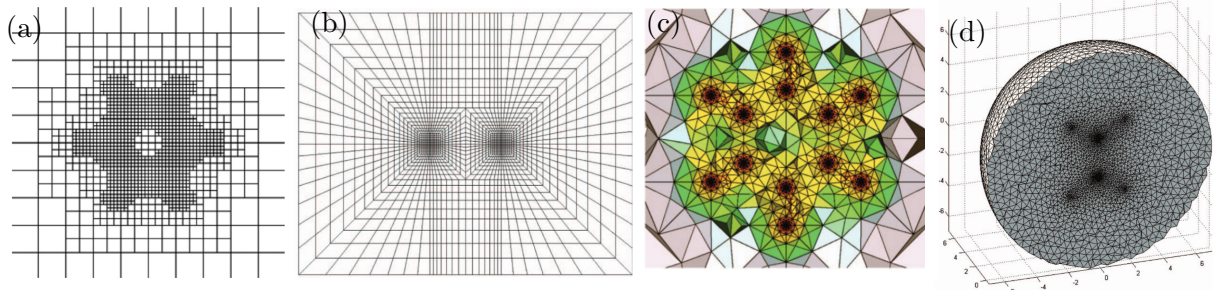


Figure 4.1: 2D cuts through 3D meshes for molecular systems obtained with different schemes for local refinement: (a) hexahedral elements adapted for the benzene molecules [155] (b) hexahedral mesh for a diatomic [154] (c) Polyhedral mesh for a benzene geometry [174] (d) Adaptive refined tetrahedral Mesh for ethylene. [154]

quired properties. Son and Chu [121, 125] constructed sets of points resembling molecular geometries by inserting  $N$  spherical grids with different radii  $r_i$  around the atoms and cutting off the overlapping regions. The respective radii are chosen as

$$r_i = \frac{il}{N - i + \frac{lN}{r_{\max}}} \quad i = 1, \dots, N \quad (4.2)$$

where  $r_{\max}$  is the radius of the largest sphere and  $l$  is a parameter smoothly changing between a linear  $l \rightarrow \infty$  and a  $1/r$ -mapping. For the angular distribution of grid points they suggested the use of Lebedev-grids [185] and a Womersley design [186, 187]. A more detailed discussion about the choices of grids is given in section 5.2.

A more entangled method is used by Alizadegan *et al.* [154]. They start with an initial guess for the wave function and create a grid whose distances are inverse proportional to the second gradient of the electron density

$$d \propto \left[ \max \left\{ \left| \frac{\partial^2 \rho}{\partial x^2} \right|, \left| \frac{\partial^2 \rho}{\partial y^2} \right|, \left| \frac{\partial^2 \rho}{\partial z^2} \right| \right\} \right]^{-1}. \quad (4.3)$$

which gives an estimate for the error due to linear approximation within each element. After solving the eigenvalue equation on this grid, they recompute another mesh on the basis of the new function, iterating this procedure several times. A cut through a mesh obtained by this procedure is shown in Figure 4.1d.

## 4.4 Boundary Conditions

Boundary conditions have not been addressed in this thesis so far for any of the methods but play an important role determining the properties of the solution. In many cases, the boundary condition (BC) leads to uniqueness of the solution or at least it determines the branch to be searched as, *e.g.* outgoing or incoming waves in case of the Helmholtz equation. The simplest case is Dirichlet-boundary, requiring the wave function to vanish at the boundaries of a finite region. In the FEM, this condition can be applied especially simple by setting the coefficients of the outermost shape functions to zero. This truncation, however, strongly influences the wave function and discretises the spectrum since only an exact number of oscillations is allowed in the respective region. To ensure a reasonably

low error in energy, large domains are required. Considering a particle with 1 eV kinetic energy, its wavelength is 23 bohr. To make the energy gap between two waves of the same angular momentum smaller than 0.1 eV, at least 10 oscillations should fit in the radial direction, requiring a box-size of more than 230 bohr which is a unreasonably large sphere while kinetic energies in the meV-range lead to even worse scenarios.

Besides the numerical restriction to a finite box also mapping schemes can be used as *e.g.*  $x = \tan(\frac{y}{2})$  that maps the range  $[-\infty : \infty]$  to  $[-\pi : \pi]$  [128]. However, using such a mapping directly may lead to arbitrarily high oscillations and thus to arbitrarily sharp features in the mapped range. Since the solution of unbounded differential equation occurs in many fields of physics and engineering, more sophisticated boundary conditions are available and the most important ones are presented in the following sections.

#### 4.4.1 Complex Absorbing Potential

The complex absorbing potential (CAP) is a method often found in the literature when describing quantum-mechanical problems with infinite extent [63, 64, 188]. In this scheme, an artificial potential that is usually of quadratic form

$$W_{\text{CAP}}(\mathbf{r}) = \begin{cases} -i\eta(\mathbf{r} - \mathbf{r}_0)^2 & , \mathbf{r} > \mathbf{r}_0 \\ 0 & , \text{else} \end{cases} \quad (4.4)$$

is added where the scaling  $\eta$  is a free parameter and  $\mathbf{r}_0$  is larger than the region where the solution is to be evaluated. Such a potential damps the reflection of the wave function at the boarders and thus enhances the quality of states obtained on a finite region [189, 190] and can be shown to be equivalent to the complex scaling schemes that enjoy some popularity as well [188, 190, 191]. The imaginary potential (4.4) leads to a non-hermitian term in the Hamiltonian and thus makes its eigenvalues complex whose real part corresponds to the energy of the respective state and the imaginary part is interpreted as its lifetime [191].

However, studies with different shapes of these potentials show that they influence the wave function not only close to the boarders and a proper design of the parameters is non-trivial [192]. To minimise the error due to the CAP, the parameter  $\eta$  can be chosen such that its dependency on the energy vanishes in first order, *i.e.*  $\eta \frac{dE}{d\eta} = 0$  [67, 192]. If the parameter is chosen inappropriately, reflections or unstable resonances, making them strongly basis-set dependent, can occur [192]. Moreover, a dependence of the error on the frequency was observed [193].

#### 4.4.2 Non-Reflecting Boundary Conditions

The term non-reflecting BC (or absorbing BC) describes a large class of BCs for problems on an infinite domain where it is subdivided into a finite computational domain and a residual infinite part that fulfils the requirement of not reflecting the solution back into the finite region of interest [194]. Thus, also the previously described R-matrix approach (section 2.2) as well as the infinite elements described in section 4.4.4 belong to this group of BCs. There are also recently proposed approaches that are called perfectly matched layer schemes [195–197].

Absorbing BCs can in principle be applied to any kind of system but their applications are particularly prominent for the Helmholtz equation [194, 198–200]. However, the problem of finding a reasonable non-reflecting BC is not yet solved for general case (*i. e.* independent on symmetry and for other equations such as the Laplace equation) and is currently under investigation [194, 200].

As an example for a non-reflecting BC, the mode-matching scheme [201] is presented here which yields a particularly simple formalism. In this scheme, the solutions of the Helmholtz problem in the finite inner region  $\Gamma$  and infinite outer regions  $\mathbb{R}^3 \setminus \Gamma$  are considered as two separate functions, each described by the equations

$$\nabla^2 \Psi_1(\mathbf{r}) + V(\mathbf{r})\Psi_1(\mathbf{r}) - E\Psi_1(\mathbf{r}) = 0 \quad (4.5)$$

and

$$\nabla^2 \Psi_2(\mathbf{r}) - E\Psi_2(\mathbf{r}) = 0 \quad (4.6)$$

whereby the outer function needs to satisfy the Sommerfeld condition [43]

$$\lim_{r \rightarrow \infty} r \left( \frac{\partial \Psi_2(r)}{\partial r} - ik\Psi_2 \right) \rightarrow 0 \quad (4.7)$$

along the radial direction  $r = |\mathbf{r}|$  in three dimensions. The quantities  $\Psi_1(\mathbf{r})$  and  $\Psi_2(\mathbf{r})$  are moreover coupled by

$$\Psi_1(\mathbf{r}_0) = \Psi_2(\mathbf{r}_0) \quad \text{and} \quad \nabla \Psi_1(\mathbf{r}_0) \mathbf{n} = \nabla \Psi_2(\mathbf{r}_0) \mathbf{n} \quad \mathbf{r}_0 \in \partial\Gamma, \quad (4.8)$$

where  $\mathbf{n}$  is the normal vector on  $\partial\Gamma$ . The eqs.(4.8) ensure continuity of the solution and the gradient normal to the boundary [201]. To ensure the Sommerfeld condition, one uses a respective basis in the outer region, *e.g.* Spherical waves. Using the mode-matching scheme with finite elements, the eqs.(4.5) result in matrices similar to eq.(3.26) that are coupled by the conditions (4.8) that enter the weak formulation since the application of Greens' first identity in eq.(3.22) leads to an extra term.

#### 4.4.3 The Boundary Element Method

The boundary element method (BEM) can be considered as a self-standing method for solving partial differential equations using the weak formulation [202, 203]. The BEM is based on Greens' theorem, the Gauß-Ostrogradskii (divergence) theorem as well as Stokes theorem according to which all properties of a system can be projected onto its boundaries [204]. In this method, thus, the partial-derivative equations are solved on the discretised boundaries only, leading typically to lower dimensional problems to be solved compared to volume-based methods such as the FEM. However, the BEM scheme suffers strongly from the restriction of being applicable only to linear systems for which a fundamental solution is known. In addition, it leads to dense, unsymmetric matrix equations [203] which are numerically costly. Still, this scheme enjoys up to now some popularity [205–207]. Its main advantages come into play when combined with the FEM [208] to obtain an accurate solution in the inner region and the boundaries are treated with the BEM. Considering an unbound domain as, *e.g.*, the problem of the outgoing electron, the infinite

domain  $\Gamma$  can be divided into a finite region  $\Gamma_i$  where the ionic ESP leads to a system-specific wave-function and the remaining domain  $\Gamma_o$  in which the time-independent SE reduces to the Helmholtz-problem whose fundamental solutions are well-known. Though the main conditions for the applicability of BEM are fulfilled for the problem of free electrons considered here [203, 209].

#### 4.4.4 Infinite Elements

The infinite element approach was developed in the 1980 for acoustical calculations and is specifically designed for the Helmholtz problem. Moreover, it can be regarded as an extension of the BEM. The general idea of the infinite elements is that the solution of the radial Helmholtz equation assuming spherical symmetry is known to be of the form

$$\Psi(r) = \left( \frac{a}{r} + \frac{b}{r^2} + \dots \right) e^{ikr}, \quad (4.9)$$

where  $k = |\mathbf{k}|$  is the absolute value of the momentum. Note that for the case of an outgoing photoelectron the prefactors  $a, b, etc.$  correspond to different different angular momenta as can be seen by comparison with the Bessel function. In the complete limit (for an infinite number of terms), any function fulfilling the Sommerfeld radiation condition [43] eq.(4.7) can be represented.

To use this asymptotic information, a single layer of elements is set onto the outer surface of the finite element region with shape functions of the form (4.9). To satisfy the continuity conditions, the front-face of these elements coincides with the outer face of the respective finite element, while their side faces have ray-like edges with a common centre in the middle of the finite element region as illustrated in Figure 4.2. In the graph,  $\Gamma$  denotes the outer surface of the finite element region and the solid lines correspond to the edges of an infinite element.

Over the decades several formulations of infinite elements were developed making the ansatz for the solution of the form

$$\Psi(\mathbf{r}) = \varphi(\mathbf{r}) e^{ik\mu(r)}, \quad (4.10)$$

where  $\varphi(\mathbf{r}) = f(r)\varphi_2(\mathbf{r}_\parallel)$  is a product of a transversal shape function  $\varphi_2(\mathbf{r}_\parallel)$  which depends only on coordinates  $\mathbf{r}_\parallel$  parallel to the front face  $\Gamma$  and a radial function depending only on the radial direction  $r$ . Further,  $\mu(r) = r - r_0$  where  $r_0$  is the distance from the origin of infinite elements to the surface of the FEM region. The function  $f(r)$  is a multipole expansion *i.e.* in terms of polynomials of  $\frac{r_0}{r}$ , where Jacobi-polynomials turned out to be

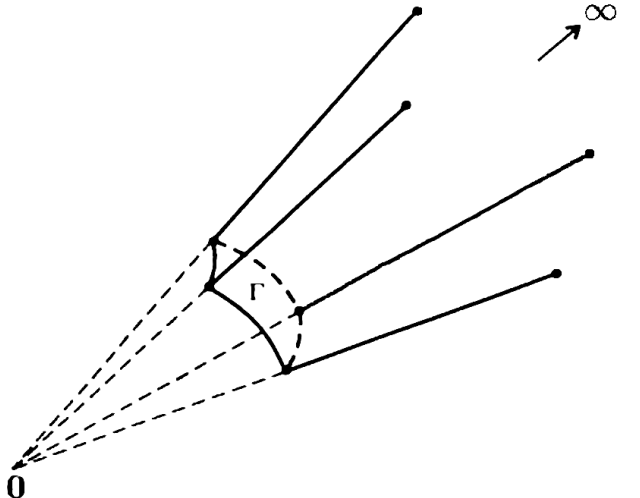


Figure 4.2: Sketch of an infinite element (solid lines). Its front face  $\Gamma$  coincides with the outer face of a finite element, the side faces are rays with a common centre. Figure adapted with modifications from [42]

the most stable basis [210, 211]. A number of different formulations have been introduced which differ in the form of the test functions.

As will be shown later, infinite elements result in a quadratic eigenvalue problem which is solved for the momentum  $k$  and its square, respectively. However, assuming that the difference between the eigenvalues of eq.(4.13) and the target energy of the outgoing electron is small, the quadratic eigenvalue problem can be approximated by the generalised eigenvalue problem (3.26) by setting  $k$  to the respective target momentum of the outgoing particle, reducing the computational cost.

## Burnett Elements

In the original Burnett formulation, the test functions are given in the form

$$\Phi(\mathbf{r}) = \varphi(\mathbf{r})e^{-ik\mu(r)}. \quad (4.11)$$

In the literature, usually the sign in the exponent is changed due to the use of another convention in the notation of the weak formulation eq.(3.22).

Important is, however, that in the equation later on the test and ansatz functions enter both with same oscillatory factor, introducing oscillations with  $e^{2ik(r-r_0)}$  in the Hamiltonian. Thus, the resulting eigenproblem can be formulated as a non-linear problem by treating these oscillations as an unknown. Alternatively, one sets  $k$  to the target value, resulting in an energy-dependent Hamiltonian. Even in the latter case, a quadratic eigenvalue problem remains which is non-hermitian. Moreover it was found that this formulation can lead to numerical instabilities [41] and to a wrong asymptotic behaviour.

To get rid of the oscillatory terms, in the unconjugated Burnett scheme the test functions can be chosen to coincide (in the notation used within this thesis) with the space of ansatz functions eq.(4.10) and results in a symmetric quadratic eigenvalue problem. However, the formulation of the Hamiltonian in this case is more complicated since the infinite integrals along the radial direction do not converge anymore [41, 212]. However, it can be shown that due to the symmetrisation of the kinetic energy term (see eq.(3.22)) additional surface integrals show up which lead to cancellation of the undefined terms [212]. However, numerical tests comparing the conjugated and unconjugated formulations showed that the unconjugated elements eq.(4.11) have better convergence properties [212].

## Asley-Leis Formulation

Even though the conjugated Burnett elements do not perform that well, the conjugated infinite element formulation is appealing and can be expected to be numerically advantageous due to the cancellation of the infinite oscillations in the Hamiltonian. Since the conjugated Burnett formulation seems to be not advantageous with the infinitely large contributions, in the Astley-Leis formulation the matrix elements are modified by an additional damping term in the infinite region. Since the space of ansatz functions (4.10) corresponds to the multipole expansion of the outgoing waves, it should however not be modified. To obtain a formulation with finite integrals with it, Astley suggested to chose test functions of the shape

$$\Phi(\mathbf{r}) = D(r)\varphi(\mathbf{r})e^{ik\mu(r)}, \quad (4.12)$$

where in three dimensions  $D(r) = \frac{1}{r^2}$  [40], leading to a non-symmetric Petrov-Galerkin scheme and a non-hermitian Hamiltonian.

Similar to the conjugated Burnett formulation, the resulting eigensystem does not have the energy as its eigenvalues but the generalised eigenvalue problem (3.26) formulated in chapter 3.5 changes to the quadratic eigenproblem

$$\mathbb{A}\mathbf{c} + ik\mathbb{B}\mathbf{c} - k^2\mathbb{C}\mathbf{c} = 0 \quad (4.13)$$

that is solved for the absolute value of the momentum  $k = |\mathbf{k}|$ . The respective matrix elements are

$$\mathbb{A}_{i,j} = \int \left( V(\mathbf{r})D(r)\varphi_i(\mathbf{r})\varphi_j(\mathbf{r}) + \frac{1}{2}D'(r)\varphi_i(\mathbf{r})\varphi'_j(\mathbf{r}) + \frac{1}{2}D(r)\varphi'_i(\mathbf{r})\varphi'_j(\mathbf{r}) \right) d\mathbf{r} \quad (4.14)$$

$$\mathbb{B}_{i,j} = \frac{1}{2} \int \mu'(r) \left( -D'(r)\varphi_i(\mathbf{r})\varphi_j(\mathbf{r}) + D(r) (\varphi'_i(\mathbf{r})\varphi_j(\mathbf{r}) - \varphi_i(\mathbf{r})\varphi'_j(\mathbf{r})) \right) d\mathbf{r} \quad (4.15)$$

$$\mathbb{C}_{i,j} = \frac{1}{2} \int (\mu'(r)\mu'(r) + 1)D(r)\varphi_i(\mathbf{r})\varphi_j(\mathbf{r}) d\mathbf{r} \quad (4.16)$$

where the prime is used as short-form of the spatial derivative and  $r = |\mathbf{r}|$  is the distance to the origin of the infinite elements, moreover the relation  $E = \frac{1}{2}k^2$  is used [42].

This formulation has been shown to be computationally robust for exterior acoustics [213, 214]. The introduced imaginary part of the eigenvalue can be considered as a broadening due to the finite lifetime. However, this lifetime is not meaningful since the damping function  $D(r)$  is arbitrary.

## Symmetrised Formulation

Besides those formulations mentioned above, further infinite element formulations are used [42]. As an example, a variation of the Burnett-elements was applied to the harmonic oscillator [52] and (bound state) DFT calculations [51] successfully. Since bound states do not show oscillations but rather an exponential decay, the exponential function in the ansatz functions are modified to  $-E_{IP}\mu(r)^2$  with the binding energy  $E_{IP}$ , respectively. However, the application of infinite elements to FEFs is to the best of my knowledge a novelty of this work.

Astley-Leis and Burnett infinite elements have the main disadvantage of a non-hermitian Hamiltonian. In this work, symmetric left and right basis functions are introduced, both being damped in the same manner:

$$\Phi(\mathbf{r}) = \Psi(\mathbf{r}) = D(r)^p \varphi(\mathbf{r}) e^{ik\mu(r)} \quad (4.17)$$

Here, as before,  $D(r) = \frac{1}{r^2}$  is taken but with the power  $p > 0$ . This provides more flexibility and ensures that the matrix elements are finite-valued and can be chosen to be, at least for small distances, similar to the analytic multipole expansion eq.(4.10). The basis formulation (4.17) changes the mass and potential energy matrices in a trivial way whereas the kinetic energy matrix, which is in the original Astley-Leis formulation non-hermitian,

becomes hermitian

$$\int (\nabla \Phi_i^*(\mathbf{r})) (\nabla \Psi_j(\mathbf{r})) d\mathbf{r} = \int D^{2p} \left( \left| p \frac{D'(r)}{D(r)} - ik\mu'(r) \right|^2 \varphi_i(\mathbf{r}) \varphi_j(\mathbf{r}) + p \frac{D'(r)}{D(r)} (\varphi_i(\mathbf{r}) \varphi_j(\mathbf{r}))' + ik\mu'(r) (\varphi_i(\mathbf{r}) \varphi_j'(\mathbf{r})) + \varphi_i'(\mathbf{r}) \varphi_j'(\mathbf{r}) \right) d\mathbf{r} \quad (4.18)$$

This is the main working equation in this work. Symmetric left and right bases ensure hermiticity of the problem and thus real-valued energies of the outgoing electron. In principle, any arbitrary small  $p > 0$  is enough to make the integrals over the infinite elements finite. Chosing it quite small one mitigates the suppression of fewer angular momenta as discussed in section 6.1.2.

## 4.5 Solving Large Eigenvalue Problems

In finite element applications such as those being proposed in this work, matrix equations with hundreds up to hundred thousands of dimensions need to be solved. This requires elaborate strategies, using the sparsity of these matrices.

The focus here is on solving the generalised eigenvalue problem (3.26) and the quadratic problem (4.13) respectively. However, efficient strategies are only known for regular eigenvalue problems of the form

$$\mathbb{A}\mathbf{x} = \lambda\mathbf{x}. \quad (4.19)$$

Hence, the more general forms will be rewritten to become (4.19) as discussed in section 4.5.1. Moreover, since the state of interest is an unbound state, one expects a high density of states. This, however, is a well-known problem in numerical mathematics since almost degenerate eigenvalues and especially their respective eigenvectors are very sensitive to small perturbations in matrix  $\mathbb{A}$ . Section 4.5.2 addresses these problems and a way for numerical stabilisation is sketched. Finally in section 4.5 few methods are presented showing how a small number of approximate eigenpairs can be obtained in a numerically efficient way from the usual eigenproblem (4.19).

For the computation of eigenpairs, many classes of solvers have been developed with various numerical properties. Besides direct solvers such as the Gauß-elimination, iterative solvers are to be mentioned that are especially well-suited for large but sparse equation systems. Besides the famous Jacobi- and Gauß-Seidel algorithms which converge only in certain cases, also the Davidson method [176, 215] and several Krylov subspace methods [216, 217] are commonly used. For finite element problems, the Krylov subspace solvers turned out to be a very efficient class [218, 219].

As discussed in the sections 4.5.1 and 4.5.2, the solution of a generalised eigenvalue problem involves undesirable matrix operations which destroy their sparse structure. As a popular choice for such classes of problems, the Krylov subspace is used. A  $q$ -dimensional Krylov subspace is generated by a vector  $\mathbf{x}$  and a matrix  $\mathbb{A}$  and has the form

$$\mathcal{K}_q(\mathbb{A}, \mathbf{x}) = \text{span} \{ \mathbf{x}, \mathbb{A}\mathbf{x}, \mathbb{A}^2\mathbf{x}, \dots, \mathbb{A}^{q-1}\mathbf{x} \}. \quad (4.20)$$

If  $\mathbb{A}$  is sparse, the evaluation of these expressions is only of order  $\mathcal{O}(d)$ , where  $d$  is the dimensionality of  $\mathbf{x}$ . The vectors obtained with large powers of  $\mathbb{A}$ , however, become more

and more linearly dependent. To prevent this, the vectors usually are orthonormalised inbetween. The orthogonalisation method being used distinguishes different Krylov subspace methods such as the Arnoldi [220] or Lanczos schemes [221]. In this work, the Krylov-Schur algorithm is used [222, 223]. An important issue in this scheme is a good choice for  $\mathbf{x}$  which crucially determines the speed of convergence. If a reasonable starting-vector cannot be guessed, the space  $\mathcal{K}_q$  needs to be extended by increasing  $q$  iteratively. To keep the dimensionality low, in this algorithm the subspace iteration is restarted after  $q$  reached a certain value, starting with a better guess  $\mathbf{x}$ .

#### 4.5.1 Generalised Eigenproblem

The most straightforward way to reformulate the generalised eigenvalue problem

$$\mathbb{A}\mathbf{x} = \lambda\mathbb{B}\mathbf{x}, \quad (4.21)$$

where left left and right bases are not orthonormal with the overlap matrix  $\mathbb{B}$  is the invert the matrix  $\mathbb{B}$ , obtaining the regular Eigenproblem  $\mathbb{B}^{-1}\mathbb{A}\mathbf{x} = \lambda\mathbf{x}$ . This inversion corresponds to the orthogonalisation of the left basis with respect to the right one but is possible only as long as  $\mathbb{B}$  is invertible and not too large since inversion is a demanding operation. Moreover, the initial matrices are sparse but  $\mathbb{B}^{-1}\mathbb{A}$  looses its sparseness [218].

To prevent the appearance of dense matrices, mathematical computer libraries often do not operate with the matrices themselves but rather with a set of vectors on which these matrices act [218]. The most popular scheme of this kind is the Rayleigh-Ritz projection where the initial problem is reduced to a smaller subspace  $\mathcal{V}_j = \text{span}\{\mathbf{v}_1, \dots, \mathbf{v}_j\}$  of dimensionality  $j$ , spanned by appropriate vectors  $\mathbf{v}_i$ .

Projecting the eq.(4.21) onto  $\mathcal{V}_j$  yields the new system  $\Sigma_j \mathbf{s} = \theta \Theta_j \mathbf{s}$  where  $\Sigma_j = \mathbb{V}_j^T \mathbb{A} \mathbb{V}_j$  and  $\Theta_j = \mathbb{V}_j^T \mathbb{B} \mathbb{V}_j$ . The matrix  $\mathbb{V}_j$  is unitary with the rows  $(\mathbb{V}_j)_i = \mathbf{v}_i$ . After solving this dense but small problem, the original eigenvectors can be approximated as  $\mathbf{x}_j = \mathbb{V}_j \mathbf{s}_j$  and  $\lambda = \theta_j$ . The obtained eigenpair is a good approximation to the actual one as long as the subspace  $\mathcal{V}_j$  contains the respective solution or contains a vector which is at least close to it.

#### 4.5.2 Stabilisation of Eigenproblems

Independent of the efficiency and robustness of the eigensolver in use, seeking solutions of the SE for free particles in continuum means that eigenenergies are very close to each other or even highly degenerate. Such dense-lying eigenvalues lead to numerical difficulties and especially the eigenvectors are known to be unreliable in this case. In practice, this means that the iterative schemes do not converge anymore, requiring a reformulation of the mathematical problem.

One way to circumvent these instabilities is to reformulate it as a minimisation problem [26]. Therefore eq.(4.1) is rewritten as  $(\frac{1}{2}\mathbb{A} + \mathbb{V} - E\mathbb{M}) \mathbf{c}_i = 0$  and is set prior to minimisation where the parameter  $E$  is the target energy. Since this does not give an ambiguous solution, one minimises the residual of the desired solution

$$\min_{\|\mathbf{x}\|=1} \left\{ \left\| \left( \frac{1}{2}\mathbb{A} + \mathbb{V} - E\mathbb{M} \right) \mathbf{x} \right\| \right\}. \quad (4.22)$$

Using the  $L_2$ -norm, it is equivalent to finding the smallest eigenvalue of

$$\left(\frac{1}{2}\mathbb{A} + \mathbb{V} - E\mathbb{M}\right)^\dagger \left(\frac{1}{2}\mathbb{A} + \mathbb{V} - E\mathbb{M}\right) \mathbf{x}_i = \theta \mathbf{x}_i, \quad (4.23)$$

where  $\theta$  is a measure for the error in energy. Whereas eq.(4.23) is only an approximation to the original problem, it has the advantage that it is a quadratic expression in the matrices which lead to a more stable behaviour [26].

Similar schemes which are reformulations of the original problem are often referred to as spectral transformations [218]. One example is the harmonic extraction, where the eigenvalues of original expression (4.21) are first shifted such that the target value is 0, leading to the equation

$$(\mathbb{A} - \tilde{\lambda}\mathbb{M})\mathbf{x} = (\lambda - \tilde{\lambda})\mathbb{M}\mathbf{x} \quad (4.24)$$

where  $\tilde{\lambda}$  is the target value of the original problem. Then, the equation is multiplied by  $\mathbb{A} - \tilde{\lambda}\mathbb{M}$ , resulting in the equation

$$(\mathbb{A} - \tilde{\lambda}\mathbb{M})(\mathbb{A} - \tilde{\lambda}\mathbb{M})\mathbf{x} = (\lambda - \tilde{\lambda})(\mathbb{A} - \tilde{\lambda}\mathbb{M})\mathbb{M}\mathbf{x} \quad (4.25)$$

which is observed to lead to faster convergence for Krylov-subspace methods [218, 224].

Other spectral transformations are the spectral folding [218] where the left and right sides of eq.(4.24) are squared respectively which often leads to higher stability but the squaring of eigenvalues leads to ambiguities with respect to the eigenvalues  $\lambda$  of the original problem. The scheme that turned out to be most beneficial for the matrices used in this work is the shift-and-invert scheme where the inverted problem of eq.(4.24), *i.e.*

$$(\mathbb{A} - \tilde{\lambda}\mathbb{M})^{-1}\mathbb{M}\mathbf{x} = \frac{1}{\lambda - \tilde{\lambda}}\mathbf{x}, \quad (4.26)$$

is solved. The formulation (4.26) has the advantage that the transformed eigenvalues  $\frac{1}{\lambda - \tilde{\lambda}}$  are well-separated and on the extrema of the new spectrum, *i.e.* they approach  $+\infty$  and  $-\infty$  if  $\tilde{\lambda}$  is inbetween two eigenvalues. Since the Krylov-scheme is especially efficient when the largest or smallest eigenvalues need to be found, this leads to faster convergence and to a more stable procedure due to the separation of eigenvalues [222]. A more generalised transformation is the Cayley-transform which has two parameters  $\tilde{\lambda}$  and  $\tilde{\tilde{\lambda}}$  and yields the usual eigenvalue problem

$$(\mathbb{A} - \tilde{\lambda}\mathbb{M})^{-1}(\mathbb{A} + \tilde{\tilde{\lambda}}\mathbb{M})\mathbf{x} = \frac{\lambda + \tilde{\tilde{\lambda}}}{\lambda - \tilde{\lambda}}\mathbf{x}. \quad (4.27)$$

Finally, a regularisation of eigenvalue problems can be performed using matrix preconditioners. Many different types of preconditioners are developed [225] but most of them are efficient only for a small class of problems. For instance, algorithms especially well-suited for matrices originating from FEM-problems have been suggested [226, 227], which can be even adapted to a FEM structure [228, 229] or to a particular physical problem [199]. Often their performance notably depends on the eigenproblem solver [230]. This fact makes their efficient use more intricate and can easily lead to higher costs than the actual benefit.

In this thesis, the shift-and-invert scheme (4.26) is used for all the calculations obtained and discussed in chapter 6.

# 5 | Applied Protocol

The method applied here is a combination of three concepts described in chapter 2. It is based on the time-independent DO formalism where the electronic structure is computed by means of the OTRSH density functional. The FEF is obtained by the finite/infinite element method as described in chapter 4. This combination represents a novelty of this work, since the DO approach has not yet been used together with OTRSH TDDFT, which is most suited among different functionals for PES calculations. The last but most important is the application of the finite and infinite element methods to obtain FEFs. To the best of my knowledge this method is used to solve such quantum-mechanical problem for the first time.

In the first section of this chapter, the computation of the wave functions of initial (unionised) and final (ionised) states as well as the general procedure used to compute the DOs is described. Thereafter, in section 5.2 the setup of the finite/infinite element system that is used to compute the free electron function as well as the dipole matrix element are explained which is implemented in the program `FreeWilly` [55] in the framework of this thesis.

## 5.1 Bound State Functions

The DO formalism as it is described in section 2.3 can be used with any electronic structure method which can predict excited state energies and wave functions such as configuration interaction [78], generalised active space configuration interaction [63], equation-of-motion coupled cluster [67, 231], complete and restricted self-consistent field [32, 47, 79, 80] or TDDFT as given in Table 2.1. In this work, density functional theory (DFT) is used for ground state calculations and its time-dependent counterpart TDDFT to compute excited state energies. The DFT formalism which is briefly introduced in the sections 5.1.1 and 5.1.2 has shown to be accurate and numerically cheap.

### 5.1.1 Ground State Density

The DFT is formally based on the Hohenberg-Kohn theorems [44] which state that the ground-state electron density  $\rho(\mathbf{r})$  determines the potential in the SE and with this also the wave function. Moreover, the energy of the ground state can be found variationally. Thus, the electron density contains all information needed and the computation of the  $N$ -electron wave function can be omitted. Since the Hohenberg-Kohn theorems do not point out a way how to determine the electron density without knowing the wave function, usually the Kohn-Sham scheme [45] is used. In this framework, the electrons are described as

non-interacting particles in a respective pseudo-potential that is constructed such that the Kohn-Sham density coincides with the real ones. Since the particles do not interact with each other, the Kohn-Sham orbitals  $\Psi_j(\mathbf{r})$  can be obtained from the one-particle SE

$$\left( -\frac{1}{2} \nabla^2 + V_{\text{eff}}(\mathbf{r}) \right) \Psi_j(\mathbf{r}) = \epsilon_j \Psi_j(\mathbf{r}), \quad (5.1)$$

where  $\epsilon_j$  is the energy of the respective Kohn-Sham orbital  $\Psi(\mathbf{r})$  and the effective potential

$$V_{\text{eff}}(\mathbf{r}) = V_{\text{ext}}(\mathbf{r}) + \int \frac{\rho(\mathbf{r}')}{|\mathbf{r} - \mathbf{r}'|} d\mathbf{r}' + V_{\text{xc}}(\mathbf{r}) \quad (5.2)$$

can be separated into the external potential  $V_{\text{ext}}(\mathbf{r})$ , which consists of the attractive nuclear ESP and external fields, the electrostatic interaction of the particles with a charge density  $\rho(\mathbf{r}) = \sum |\Psi_i|^2$  and the exchange-correlation potential  $V_{\text{xc}}(\mathbf{r})$  which contains the complexity of the interelectronic interaction [232]. The exchange correlation potential  $V_{\text{xc}}(\mathbf{r})$  contains, besides contributions from exchange and correlation, also correction for the error of kinetic energy present due to the fact that the Kohn-Sham wave functions differ from the real orbitals [233].

The exact exchange-correlation potential  $V_{\text{xc}}(\mathbf{r})$  is not known, giving rise to different variants of approximate functionals, each suited for particular problems and applications. However, usually the exchange-correlation is split into an exchange and a correlation functional for which separate approximations are used. The exact exchange potential acting on an orbital  $\Psi_i(\mathbf{r})$  has the form

$$V_{x;j}(\mathbf{r}) \Psi_i(\mathbf{r}) = - \int \frac{\Psi_j^\dagger(\mathbf{r}') \Psi_i(\mathbf{r}')}{|\mathbf{r} - \mathbf{r}'|} d\mathbf{r}' \Psi_j(\mathbf{r}) \quad (5.3)$$

and thus is non-local [233]. The term exact indicates here that, using the exchange potential eq.(5.3), the self-interaction error of the Coulomb interaction (*i.e* the second term in equation eq.(5.2)) cancels out completely. In DFT, usually the exchange energy is approximated as a local functional of the density and its derivative, leading to the so-called local density approximation and gradient corrected functionals [232]. The Becke [234] exchange-functional used in this work has the form

$$E_x = \frac{3}{2} \left( \frac{3}{4\pi} \right)^{\frac{1}{3}} \sum_{\sigma} \int \rho_{\sigma}(\mathbf{r})^{\frac{4}{3}} d^3\mathbf{r} - \beta \sum_{\sigma} \int \rho_{\sigma}(\mathbf{r})^{\frac{4}{3}} \frac{x_{\sigma}(\mathbf{r})^2}{1 + 6\beta x_{\sigma} \sinh^{-1}(x_{\sigma}(\mathbf{r}))} d^3\mathbf{r}, \quad (5.4)$$

where the first summand corresponds to the local density approximation and the second is a semi-empirical gradient correction,  $\sigma$  denotes the spin orientations and  $x_{\sigma}(\mathbf{r}) = |\nabla \rho_{\sigma}(\mathbf{r})| / \rho_{\sigma}^{\frac{4}{3}}$ . The gradient correction in this functional is constructed such that the asymptotic behaviour of the exchange energy and electron density follow

$$\lim_{r \rightarrow \infty} E_x^{\sigma}(\mathbf{r}) = - \frac{1}{|\mathbf{r}|} \quad (5.5)$$

$$\lim_{r \rightarrow \infty} \rho(\mathbf{r}) = e^{-a_{\sigma}|\mathbf{r}|} \quad (5.6)$$

with  $a_{\sigma}$  is a constant related to the ionisation potential of the system under study [234].

The prefactor of the gradient correction,  $\beta$ , was determined by fitting to several atomic noble-gas systems and is set to be  $\beta = 0.0042$  a. u. [234]. However, this parameter is not universal and errors in the asymptotic behaviour eq.(5.5) can occur for general systems.

The correlation potential finally is defined as the functional derivative of the correlation energy with respect to the electron density  $V_c(\mathbf{r}) = \frac{\partial E_c[\rho]}{\partial \rho(\mathbf{r})}$ . In the case of the LYP-correlation energy functional applied here, the correlation energy is estimated based on the Hartree-Fock approach and fitted to experimental data using two parameters using various closed and open shell systems [235].

### 5.1.2 Properties of Excited States

Since the ground-state density fully specifies the system's Hamiltonian, it contains information on the excited states which can be extracted from the response of the density to the periodic external fields via the time-dependent DFT (TDDFT) which is based on the Runge-Groß theorem [236]. Using the configuration interaction approach, an excited state wave function  $|\Psi^{\text{exc}}\rangle$  is written as

$$|\Psi^{\text{exc}}\rangle = \sum_{ia} c_{ia} |\Psi_i^a\rangle \quad (5.7)$$

where  $|\Psi_i^a\rangle$  are SDs in which the  $i$ -th occupied orbital is replaced by the virtual orbital  $a$  and  $c_{ia}$  are coefficients whose absolute squares sum up to one. Commonly, when referring to TDDFT, the respective linear-response scheme is meant [237].

It is a first order perturbation expansion and can be used to obtain the energies and wave functions of excited states using the so-called Casida-equation [238]

$$\begin{bmatrix} \mathbb{A} & \mathbb{B} \\ \mathbb{B}^\dagger & \mathbb{A}^\dagger \end{bmatrix} \begin{bmatrix} \mathbf{X} \\ \mathbf{Y} \end{bmatrix} = \omega \begin{bmatrix} \mathbb{1} & 0 \\ 0 & -\mathbb{1} \end{bmatrix} \begin{bmatrix} \mathbf{X} \\ \mathbf{Y} \end{bmatrix} \quad (5.8)$$

where the matrix elements are

$$\mathbb{A}_{ia,jb} = \delta_{ij}\delta_{ab}(\varepsilon_a - \varepsilon_i) + \int \int d\mathbf{r} d\mathbf{r}' \frac{\Psi_i(\mathbf{r})\Psi_a(\mathbf{r})\Psi_j(\mathbf{r}')\Psi_b(\mathbf{r}') - \Psi_i(\mathbf{r})\Psi_j(\mathbf{r})\Psi_a(\mathbf{r}')\Psi_b(\mathbf{r}')}{|\mathbf{r} - \mathbf{r}'|}, \quad (5.9)$$

$$\mathbb{B}_{ia,jb} = \int \int d\mathbf{r} d\mathbf{r}' \frac{\Psi_i(\mathbf{r})\Psi_a(\mathbf{r})\Psi_b(\mathbf{r}')\Psi_j(\mathbf{r}') - \Psi_i(\mathbf{r})\Psi_b(\mathbf{r})\Psi_a(\mathbf{r}')\Psi_j(\mathbf{r}')}{|\mathbf{r} - \mathbf{r}'|}. \quad (5.10)$$

Here  $i, j$  denote occupied and  $a, b$  virtual states and  $\mathbb{1}$  is the unity matrix,  $\varepsilon_\alpha$  are the energies of the Kohn-Sham orbitals  $\Psi_\alpha(\mathbf{r})$ . The indices  $i, j$  and  $a, b$  denote occupied and virtual orbitals with binding energy  $\varepsilon_i, \varepsilon_a$  respectively [237]. The Casida equation (5.8) is a non-hermitian eigenvalue problem whose eigenvalues  $\omega$  correspond to the transition energies and the eigenvectors contain the transition coefficients  $c_{ia}$  from eq.(5.7). The different blocks in equation (5.8) have different physical interpretation. Because of the negative sign of the transition energy counterpart of the eigenvector  $\mathbf{Y}$  corresponds to negative excitation energies and can be assigned to de-excitations from virtual orbitals. This makes no physical sense if the reference state is a ground state [237] however for the excited states corresponds to orbital relaxation. Since the matrix  $\mathbb{B}$  contains usually only small elements, it is often set to zero which is referred to as Tamm-Danoff approximation

and reduces the original equation to a hermitian equation of half dimensionality with only small loss in accuracy [238].

### 5.1.3 OTRSH-scheme

One main disadvantage of the DFT-formalism is that the approximate exchange functional lead to wrong asymptotic behaviour of the electron density. The local density approximation leads to an exponential decay instead of  $\frac{1}{r}$  and  $\frac{1}{r^4}$  for the exchange and correlation terms respectively [46] which is improved significantly with gradient-corrected functionals but usually still yields spurious behaviour [232]. This issue is known as self-interaction error because the approximate exchange potentials do not eliminate the interaction of an electron with itself at large interaction distances. This is opposite to the exact exchange potential eq.(5.3), where such elimination exists. This wrong behaviour affects the obtained wave functions and thus the orbital energies and implicitly influences other system properties [18].

To reduce this error, so-called range-separated hybrid functionals are used, in which the DFT-exchange term as, *e.g.*, the Becke functional (5.4) is used for small interelectronic distances only, while at larger distances, where correlation effects are not that important, the Hartree-Fock exact-exchange (5.3) is used [239]. The interchange between the exact and approximate exchange functionals is done by some smooth function, for instance

$$\frac{1}{r} = \underbrace{\frac{\alpha + \beta \text{erf}(\omega r)}{r}}_{\text{exact exchange}} + \underbrace{\frac{1 - \alpha - \beta \text{erf}(\omega r)}{r}}_{\text{DFT exchange}}, \quad (5.11)$$

where  $\alpha + \beta = 1$  and  $\omega$  are parameters to be chosen. These parameters are density- and thus system dependent. Besides taking the standard parameters that are fitted for a set of testing-systems, *ab-initio* schemes for choosing  $\alpha$  and  $\omega$  are available which are referred to as optimally-tuned range-separated hybrid (OTRSH) density functionals. Using such an approach, the Koopmans' theorem can be ensured by minimising following functional with respect to  $\alpha$  and  $\omega$  [46]

$$J(\alpha_{\text{opt}}, \omega_{\text{opt}}) = \min_{\alpha, \omega} \{|E_N(\alpha, \omega) - E_{N-1}(\alpha, \omega) - \varepsilon_{\text{HOMO}}|\} \quad (5.12)$$

where  $E_N$  is the energy of the  $N$ -electron state and  $\varepsilon_{\text{HOMO}}$  corresponds to the binding energy of the highest occupied molecular orbital (HOMO). Such a procedure improves the asymptotic behaviour of the density and with this the orbital energies. The latter is important especially for the photoelectron spectra and usually improves the calculated ionisation potentials. This procedure is in general providing several  $(\alpha, \omega)$  pairs.

Another property to be ensured during the optimisation is the derivative discontinuity [240–242]. The exact exchange-correlation energy should be a straight line when varying the number of electrons from  $N$  to  $N - 1$ . The slope of that line corresponds to the binding energy of the respective electron that is removed and thus is discontinuous at integer numbers of electrons. The approximate exchange correlation functionals, however, usually do not fulfill this condition having curvilinear dependence of energy with a wrong derivative jump or no discontinuity at all. The criterion for  $E_{\text{xc}}(N)$  to be a straight line is used additionally to choose the best pair  $(\alpha, \omega)$  for the particular system.

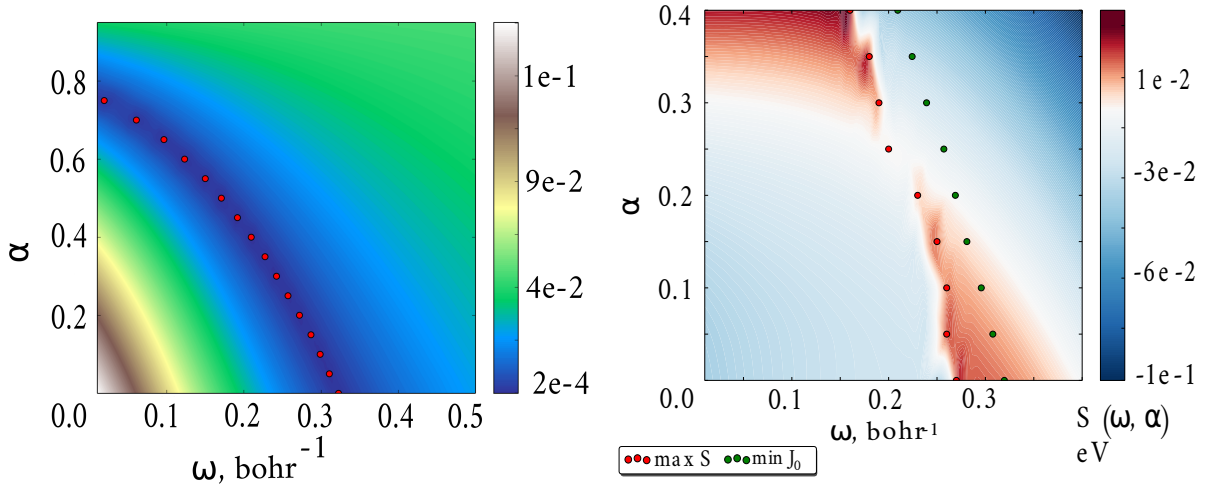


Figure 5.1: lowest eigenvalue of the stability matrix of benzene as function of  $\alpha$  and  $\omega$ . Largest stability and minimal  $J(\alpha, \omega)$  yield different solutions.

In this work, for the optimization procedure the Gaussian package G09 [54] was used with the 6-31G(d) [243, 244] basis set and the LC-BLYP exchange-correlation functional [245]. The ground state DFT calculation, optimisation of geometries has been conducted with a locally modified version of NWChem [53], employing the basis set def2-TZVP [246] without symmetry restrictions.

The application of the functional eq.(5.12) to the benzene molecule for different parameters  $\alpha$  and  $\omega$  results in a deviation from Koopman's theorem as illustrated in the left panel in Figure 5.1. This behaviour is prototypical for this functional when varying the parameters  $\alpha$  and  $\omega$ . As the Figure 5.1 illustrates, leads the imposition of Koopmans' theorem not to a unique set of parameters. Instead, a larger constant exact exchange  $\alpha$  can be compensated by a smaller  $\omega$ , *i.e.* the non-constant contributions are added for a larger radius. Another important quantity is the stability matrix which corresponds in TDA! to the matrix  $\mathbb{A}$  in the Casida equation (5.8). Its lowest eigenvalue corresponds to the transition from the HOMO to LUMO and should be, as such, positive. In contrast to the behaviour of the  $J$ -functional eq.(5.12), the lowest eigenvalue of the stability matrix has no such prototypical dependence on  $\alpha$  and  $\omega$  as the comparison of the right panel in Figure 5.1 with Figure A.6 shows where the respective HOMO-LUMO gap for the  $S_8$ -molecule is shown. Further, the choice of a particular set of parameters from the minimal parabola of the right panel of Figure 5.1 has a strong influence on the excitation energies and leads even to negative excitaiton energies for some molecules. Here, as a second criterion for the optimal parameters, the derivative discontinuity is chosen. figure How to indicate that the optimisation and cration of figures was not done by me? The parameters resulting from this are  $\alpha = 0.00$  and  $\omega = 0.32$ .

### 5.1.4 Obtaining the Electrostatic Potential and Dyson orbitals

The ESP used in this work is obtained with a modified version of NWChem [53] where the points, at which this potential should be computed can be specified by the user. Setting these points to the quadrature points of the integration scheme in the FEM calculations requires some extra effort but has the great advantage that no interpolation of the potential

is required. However, **NWChem** can compute the values only up to a finite minimum distance to the nuclei due to numerical reasons. The missing values are approximated as  $Z/r$  where  $Z$  is the respective nucleus charge and  $r$  is the distance of the quadrature point to the closest nucleus. Figure 5.2 shows the quality of such an interpolation comparing the calculated ESP for three singly ionised systems with the two limiting cases at large and small distances from the nucleus. It can be seen that the  $Z/r$  dependence approximates the ESP close to the nucleus very well. An interpolation of the data on the complete domain in **FreeWilly** [55] requires an interpolation-scheme for scattered data such as RBF interpolation [132–134], inverse distance interpolation [247, 248] or similar methods [249–251]. However, these methods were found to be sensitive to the parameters and do not result in a smooth ESP due to spurious oscillations between the quadrature points.

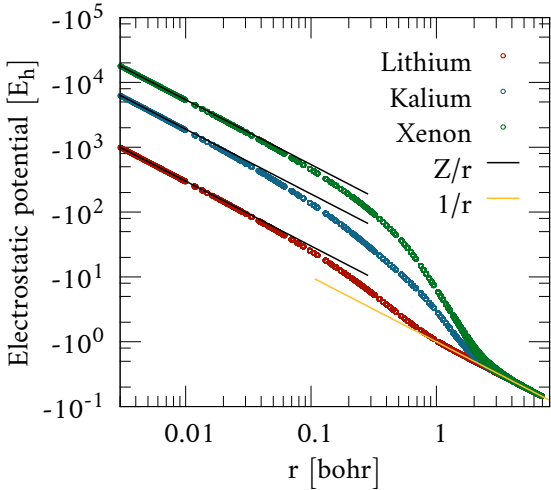


Figure 5.2: Double-logarithmic plot of the ground state ESP for  $\text{Li}^+$  (red circles;  $Z = 3$ ),  $\text{K}^+$  (blue circles;  $Z = 19$ ) and  $\text{Xe}^+$  (green circles;  $Z = 54$ ) as a function of distance from the nucleus and its limiting cases at large ( $1/r$ ) and small ( $Z/r$ ) distances.

expansion for a number of excited states) as well as the atomic overlap matrix are interfaced to the in-house software **DYSON** [32] (G.Grell) that computes the DOs. Throughout this work, the initial state is chosen to be the ground state of the respective neutral  $N$ -electron system that is represented with one slater determinant  $|\Psi_i^N\rangle$  whereas the final state can be the ground or excited state of the ion, having the general CI-expansion eq.(5.7). [how about notation: Now I have two different  \$i\$ : which to change? General change in notation?](#) Thus, the DO  $|\Psi^{\text{DO}}\rangle$  eq.(2.16) ?? need other eq. for reference!? can be written as

$$|\Psi^{\text{DO}}\rangle = \sum_{ia} c_{ja} \langle \Psi_i^N | \Psi_{ja}^{N-1} \rangle. \quad (5.13)$$

Knowing the overlap matrix of the atomic orbitals, the overlap integral eq.(5.13) is reduced to a summation of the transition coefficients  $c_{ja}$  [32] which are obtained as eigenvectors of the Casida equation eq.(5.8).

## 5.2 Free Electron Function

The main goal of this thesis is the development of a FEF representation using a finite element scheme that is implemented the program **FreeWilly** [55] in the framework of this thesis. It is based on the library **Libmesh** [56] which itself uses several libraries for the required linear algebra [57, 59, 254] and the mesh-setup [255, 256]. As discussed in section 4, the most crucial step in a FEM simulation is the setup of the grid. The **FreeWilly**-code implements several closely related schemes, with are described in section ???. Moreover, for comparison purposes here plane wave functions written in a truncated Coulomb basis are used to estimate the PES intensities in the DO formalism. This method has shown to yield good agreement with experiment for various molecules [34, 35, 47].

### 5.2.1 Coulomb Waves

An established representation of the FEF in the Dyson formalism is the expansion of a plane wave in Coulomb wave functions [34, 35, 107]. Such an approach is used here for comparison with the results obtained using a photoelectron function as computed with an finite element/infinite element method. The results using a Coulomb wave as FEF presented here are obtained making use of the **ezDyson** v. 3.0 [34] program in which integration of the dipole transition moment eq.(2.16) is performed using a uniform cuboidic grid. The particular parameters for these grids are chosen such that they are converged to avoid a significant influence due to integration errors. In particular, for the atomic lithium here a cubic box with a diameter of 4 Å and 160 grid points is chosen. For carbondioxide, the grid was choosen to be 8 Å along the molecular axis and 8 Å, with 360 and 200 grid points respectively. The grid for benzene has a height (orthogonal to the molecular plane) of 8 Å and a diameter of 12 Å in both directions of the molecular plane with 380 points in each direction. To reduce the computational effort, moreover, all transitions for which the norm of the corresponding DO is below ... *Where do I find this number?* are neglected.

### 5.2.2 Setup of the Grid

In the program **FreeWilly**, the finite elements are constructed using a set of points via Delaunay triangulation with the library **tetgen** [255]. The distribution of these points is responsible for the quality of the obtained solution via many parameters in a non-trivial way. While choosing these parameters one should account for:

- **The molecular geometry** The grid point density should be large close to the atomic nuclei and coarser at larger distances.
- **The kinetic energy** (wavelength of the outgoing wave) of the photoelectron which determines the maximum distance between two grid points
- **The largest angular momentum of the Dyson orbital** determines the largest angular momentum of the photoelectron to be resembled assuming that the dipole selection rules  $\Delta l = \pm 1$  hold. This is in general not strictly true.

To account for these properties in the best way, here two algorithms are used, based on a scheme suggested by Son and Chu [125] but using different functions for the distribution of points. In this scheme, the molecular region is composed of spheres with different radii, centred at the nuclei and whose overlapping regions belonging to different atoms are cut

off. Thus, the setup of a point distribution is subdivided into three parameters to be found: The radii of the individual spheres, the distribution of points on these spheres and the number of points per sphere.

To yield a reasonable mesh, the maximal radii  $r_{\max}$  of these spheres need to be larger than the bond lengths to avoid interatomic gaps in molecules. Using such a scheme, the global grid is determined by the size of the largest sphere  $r_{\max}$ , the number  $N$  of spheres being used for each atom as well as the distribution of the radii of spheres and angular distributions of points on each sphere, respectively. For the radii of  $N$  spheres, Son and Chu [121] suggested the following scheme

$$r_i = \frac{iq}{N - i + \frac{qN}{r_{\max}}} \quad i = 1, \dots, N \quad (5.14)$$

where  $q$  is a parameter that determines the distance between the most inner spheres. Using this function, the smallest spheres ( $i \ll N$ ) are scaled linearly, having distances  $r_{\max}/N$  between the closest spheres whereas the radii of the largest spheres depends non-trivially on the parameters but can become very large if  $q$  is small. In the limit of infinitely large  $q$ , eq.(5.14) corresponds to a uniform distribution of spheres.

To obtain better control of the distances between the inner spheres and the maximum distance which needs to be considerably smaller than the wave length, the formula

$$r_i = \frac{iq}{\left(\frac{N}{i}\right)^s \left(\frac{Nq}{r_{\max}} - 1\right) + 1} \quad i = 1, \dots, N \quad (5.15)$$

is suggested in this work. It has two degrees of freedom  $q$  and  $s \geq 1$ , where the condition  $N > \frac{r_{\max}}{q}$  needs to be fulfilled to ensure positive radii. Here  $q$  is the asymptotic distance between two spheres whereas the distance of inner spheres can be tuned by the power  $s+1$  so that the inner spheres become very dense.

In addition to a radial distribution that resembles the radial structure of the wave function, also a proper angular distribution of the points is required. The problem of distributing points regularly on a sphere is non-trivial. Depending on the measure being used, several schemes are proposed. A popular choice in earth sciences are so-called geodesic grids [257–259], but their construction allows only for exponentially growing mesh-sizes and thus they are not of interest here. Instead, in the implemented protocol several point-sets of stemming from quadrature rules of numerical integration schemes of a given order on a sphere. The order in these schemes corresponds to the largest spherical harmonic that can be exactly integrated, leading to Lebedev-grids [185, 260] and spherical t-designs [261, 262]. These distributions are found more often in quantum-chemical contexts [263–266] and will be used in this thesis. Further, several point-sets implemented in **FreeWilly** represent point distributions corresponding to extrema of certain quantities such as the minimum of the Riesz s-energy[267] or other geometric properties [268–270]. The computation of the above-mentioned point-sets is very demanding to compute and thus are hard-coded in the current implementation. For comparison, finally also the spherical Fibonacci mapping [271, 272] is implemented. It yields a less regular point-distribution but is computationally much easier to obtain and, in contrast to the distributions described above, can be obtained for any number of points. However, since in finite element theory

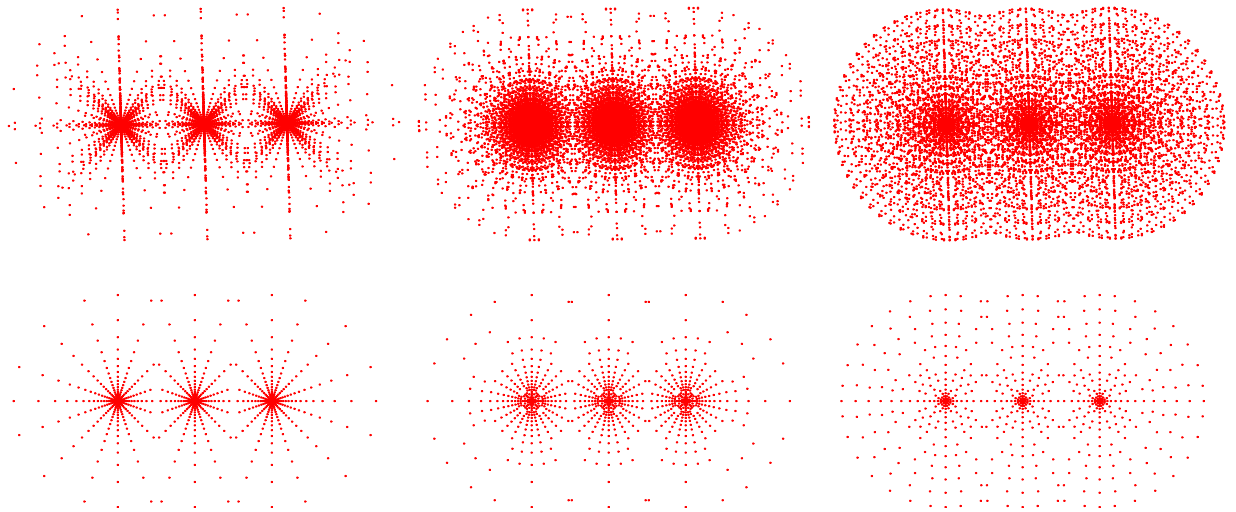


Figure 5.3: Examples of point-distributions for a CO<sub>2</sub>-molecule with  $r_{\max} = 3$  a.u. and  $N = 18$  spheres, in the upper row the full mesh and in the lower row the cuts through the molecular plane are presented. left: constant number of points  $M$  per sphere, radial scheme eq.(5.14) with  $q = 0.7$ ; centre: radial scheme eq.(5.14) with number of points according to eq.(5.17) with  $q = 0.7$ ; right: radial distribution from eq.(5.15) with  $q = 0.7$ ,  $s = 2$  and number of points per sphere according to eq.(5.16)

the sphere neither needs to be really round nor is there any global functional defined on it, the quality of a particular distribution might be not critical here.

Finally, not only the scheme used to distribute the points on the spheres, but also the number of points to be distributed is of importance. In [121] the number of points  $M$  for each sphere is chosen to be a constant parameter. Application of such a scheme is shown in Figure 5.3 in the left panel. However, it can be seen that this leads to unbalanced distances between radial and spherical neighbours. To obtain a more regular mesh, for which the radial distances between points are comparable to the distances along the sphere, here for both radial distributions, eq.(5.14) and eq.(5.15), the criterion  $d_{\text{spheric}} = \sqrt{\frac{4\pi r_i^2}{M_i}} \approx r_i - r_{i-1}$  where  $d_{\text{spheric}}$  is the average distance between two points on the sphere  $i$ . For the above described radial schemes, this results in

$$M_i = \frac{4\pi}{\left(1 - \frac{i-1}{i} \frac{N-i+\frac{lN}{r_{\max}}}{N-i+1+\frac{lN}{r_{\max}}}\right)^2} \quad (5.16)$$

for the first scheme, denoted as *son* in the following, and

$$M_i = \frac{4\pi}{\left(1 - \frac{i-1}{i} \frac{\left(\frac{N}{i}\right)p\left(\frac{lN}{r_{\max}}-1\right)+1}{\left(\frac{N}{i-1}\right)p\left(\frac{Nl}{r_{\max}}-1\right)+1}\right)^2} \quad (5.17)$$

for the radial mapping eq.(5.15) which will be referred to as *tm* in the following sections. Since some of the spherical schemes described above allow only for certain numbers of points each, here, the best approximation is used respectively.

Using this procedure, the molecular mesh is determined by the molecular geometry the largest radius  $r_{\max}$ , the radial distribution (*son* or *tm* with parameters  $s$  and  $q$ ) and the spherical point distribution. Importantly, the number of points per sphere is fixed and is

illustrated in the Figure 5.4 b) for a given set of parameters. Figure 5.4 a) shows the size

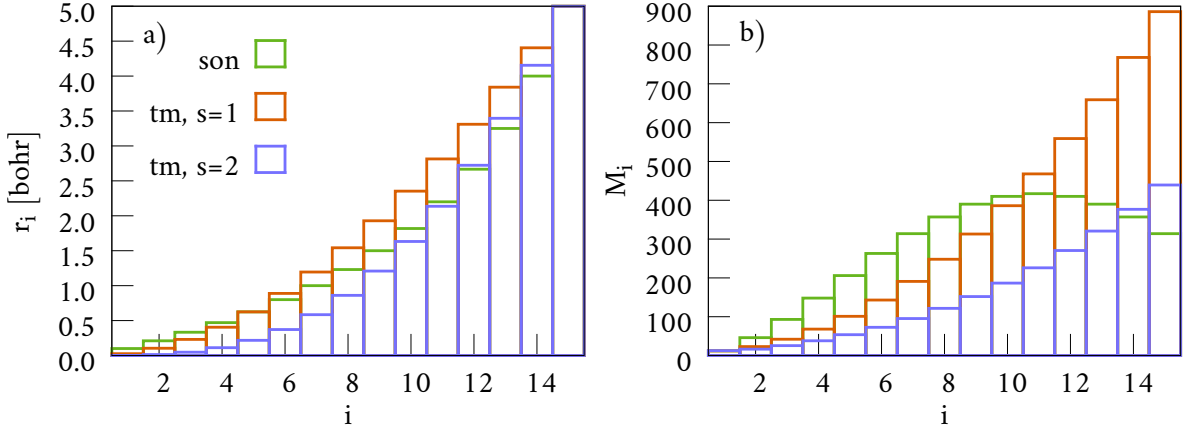


Figure 5.4: Comparison of the radius (left) and number of points (right) of the  $i$ . sphere using  $N = 15$ ,  $r_{\max} = 5$  and  $q = 2$ . The radial scheme son corresponds to eq.(5.14) and tm to eq.(5.15). For the number of points per sphere, the eq.(5.17) and eq.(5.16) are used, respectively.

of the radii of the individual spheres which follow in all three cases a similar scheme. It is important to note therein that the parameter  $q$  has a different interpretation in the different radial schemes and thus a direct comparison of the son and tm-schemes is not possible. In contrast to the distribution of radii, the number of points  $M$  on sphere number  $i$  is qualitatively different for the different radial distributions as Figure 5.4 illustrates. Here, especially the decay of  $M$  for the largest spheres in the son-scheme should be noted which is an indication that this function is not well-suited for the representation of a FEF.

Numerical tests on these schemes show, however, that the different schemes introduced above lead to finite element meshes of similar quality (see section A.1.1). The tests presented in the following are done on a single atom using a box-size of  $r_{\max} = 7$  bohr and  $N = 20$  spheres. As radial distribution, the tm-mapping eq.(5.15) is used for the schemes denoted as *const* and *tm* whereas eq.(5.14) map is used for the scheme *son*. The number of points per sphere is  $M_i = 74$  for all spheres for the *const* scheme and according to eq.(5.16) and eq.(5.17) for the others, respectively. The parameters for the radial mapping are chosen as  $q = 1.8$  and  $s = 2.6$ . In Figure 5.5, the distribution of the ratio of the longest edge to the height of the smallest side is shown, similar graphs for further quantities indicating the quality of the tetrahedra are given in A.2 in supplement and show a very similar behaviour. Thus, the quality of the generated tetrahedra is very similar for the three schemes which is, in parts, due to the modifications applied by *tetgen* but can be moreover explained by the adaptive number of gridpoints per sphere according to eq.(5.16) and eq.(5.17) which ensures some regularity of the point distribution. In this work, unless specified, the tm-scheme is used in the following since it provides more control about the distances between the outer region and thus is better suited for the description of FEFs. Similar studies are done for the properties of the solutions obtained using the different spherical grids introduced above which are shown in section ???. However, the results show only minor differences between the different schemes. In this work unless otherwise noted, the Lebedev scheme is used which provided a higher density of states (DOS) than the other schemes in this test.

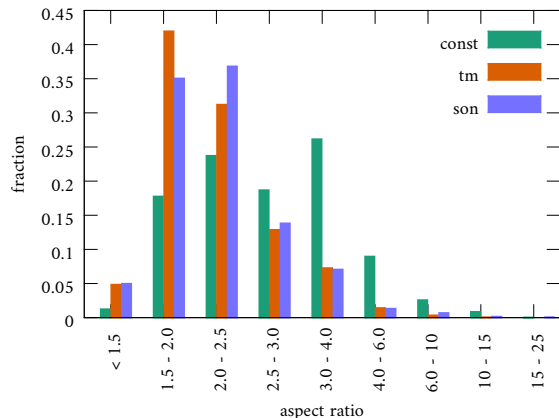


Figure 5.5: Distribution of aspect ratio (longest edge length divided by the smallest side height). Be aware that the ranges of the different bins differ.

# 6 | Results and Discussion

Since the method developed in this work combines several techniques that have not been used together so far and quantum-mechanical continuum-function are not treated with the infinite elements technique so far, several conceptual questions need to be clarified before computing actual PESs. In section 6.1, infinite elements are compared with Dirichlet BCs and their respective influence on the properties of the wave function is studied. These calculations are performed using atomic lithium and hydrogen as test system. Especially the case of hydrogen is of interest here since analytic solutions to compare with are available. Thereafter, in section 6.3, the energy-dependence of the cross section for the valence transition of lithium as well as several transitions of carbondioxide are studied, comparing several theoretical approaches with experimental data. Moreover, the PESs of CO<sub>2</sub> and benzene as computed with several theoretical approaches are shown.

## 6.1 Comparison of Boundary Conditions

In section 4.4, several BCs which give rise to different properties for the solution have been briefly overvied. Detailed studies on absorbing BCs, non-reflecting BCs as well as complex absorbing potentials can be found in literature [193, 194, 273–275]. In this work, Dirichlet boundaries and infinite elements are studied in more detail and the properties of the respective results are compared. Even though the validity of Dirichlet BCs is questionable for unbound problems, they are easy to apply and their physical consequences provide quite straightforward interpretation of the results. Thus, they provide a good comparison for the study of infinite elements, whose properties are not studied in this context yet. The infinite elements are the main objective of this work. Since they provide a reasonable description for outgoing particles, they allow for a small simulation region, even if the wavelength is very large. Moreover, they have the correct asymptotic behaviour and hence are expected to produce a good representation of continuum solutions. In section 6.1.1, systematic tests are made, studying the dependence of the eigenenergies as well as the properties of the wave function on the parameters of the numerical grid used. Thereafter, in section 6.1.2, further tests with infinite elements show the influence of these boundary conditions on the solution. Since it turns out that the solutions obtained with infinite elements are very sensitive to the parameters of mesh and simulation box, this study is performed more extensively.

### 6.1.1 Dirichlet Boundary Condition

Dirichlet boundaries are conceptually the easiest BCs but are known to have a large influence on the solution, especially for continuous functions since they reflect outgoing waves fully. Moreover, its requirement for the solutions to vanish at the boundaries results in an artificial discretisation of the spectrum similar to that of bound states. This leads to a banded spectrum, with the energy gap between two states being dependent on the simulation box size.

To understand the general properties of solutions for Dirichlet BC and to formulate requirements to the mesh quality, the method has been first tested on the hydrogen-like system with  $1/r$  ESP. To do so, the radius of the simulation box  $r_{\max}$  and the number of spheres,  $N$ , see eq.(5.15) has been varied to get convergent results. In Figure 6.1 a), the deviation in the energy of 15 solutions is shown for different  $r_{\max}$  (see eq.(5.15)), the number of spheres is kept constant at  $N = 20$ . The comparison with the red line that represents a  $\text{const}/r^3$  dependence, shows that the error is inverse proportional to the volume of the box which is a well-known result for particles in a box with infinite potential walls. The number of spheres is kept constant at  $N = 20$ . The influence of radial grid density on the energies is shown in the panels c) and d) of Figure 6.1 where the number of spheres is varied for two different box-sizes,  $r_{\max} = 4$  and  $r_{\max} = 10$  bohr, respectively. In these figures several branches of solutions can be seen that correspond to different angular momenta. For smaller radii ( $r_{\max} = 4$  bohr, panel c)), these branches are well-separated but become closer and interfere with each other at larger radii ( $r_{\max} = 10$  bohr, panel d)). Following the expectations, the energies of the respective branches decay when the number of grid points. At  $N = 18$  for  $r_{\max} = 4$  bohr the results converge and do not change much with further increase of  $N$ . However, for  $r_{\max} = 10$  bohr the convergence is much slower and cannot be reached for  $N < 60$ . In principle, the continuum spectrum should have infinite degeneracy containing FEFs corresponding to arbitrary angular momenta and since larger boxes provide higher density of states it may be considered desirable to take as large simulation boxes as possible. This in general also agrees with the common logic for quantum mechanical calculations. However, the density of states is not the only important quantity: The PES intensities being the main objective in the present work are calculated using the DO. Due to the aufbau principle, usually the atomic states with quite low angular momentum are populated. *E.g.* in molecules and atoms consisting of second period elements one can expect only  $s$  and  $p$  atomic functionals to be populated in the lowest excited electronic states. Thus, one can expect that FEFs only up to  $l = 2$  could contribute to PES intensities if the dipole selection rules hold. That is why to reproduce reliable intensities, the computational scheme should favour solutions with low angular momentum.

The panels e) and f) of Figure 6.1 show the projections of the solutions to the spherical wave functions with respective kinetic energy and different angular momentum, where the partial wave contribution is defined as

$$\sum_m |\langle \Psi_n | \Psi_{k,l,m}^{\text{Sph}} \rangle|^2. \quad (6.1)$$

Here  $|\Psi_{k,l,m}^{\text{Sph}}\rangle$  is the spherical wave eq.(3.2) with angular momentum  $l$  and its projection

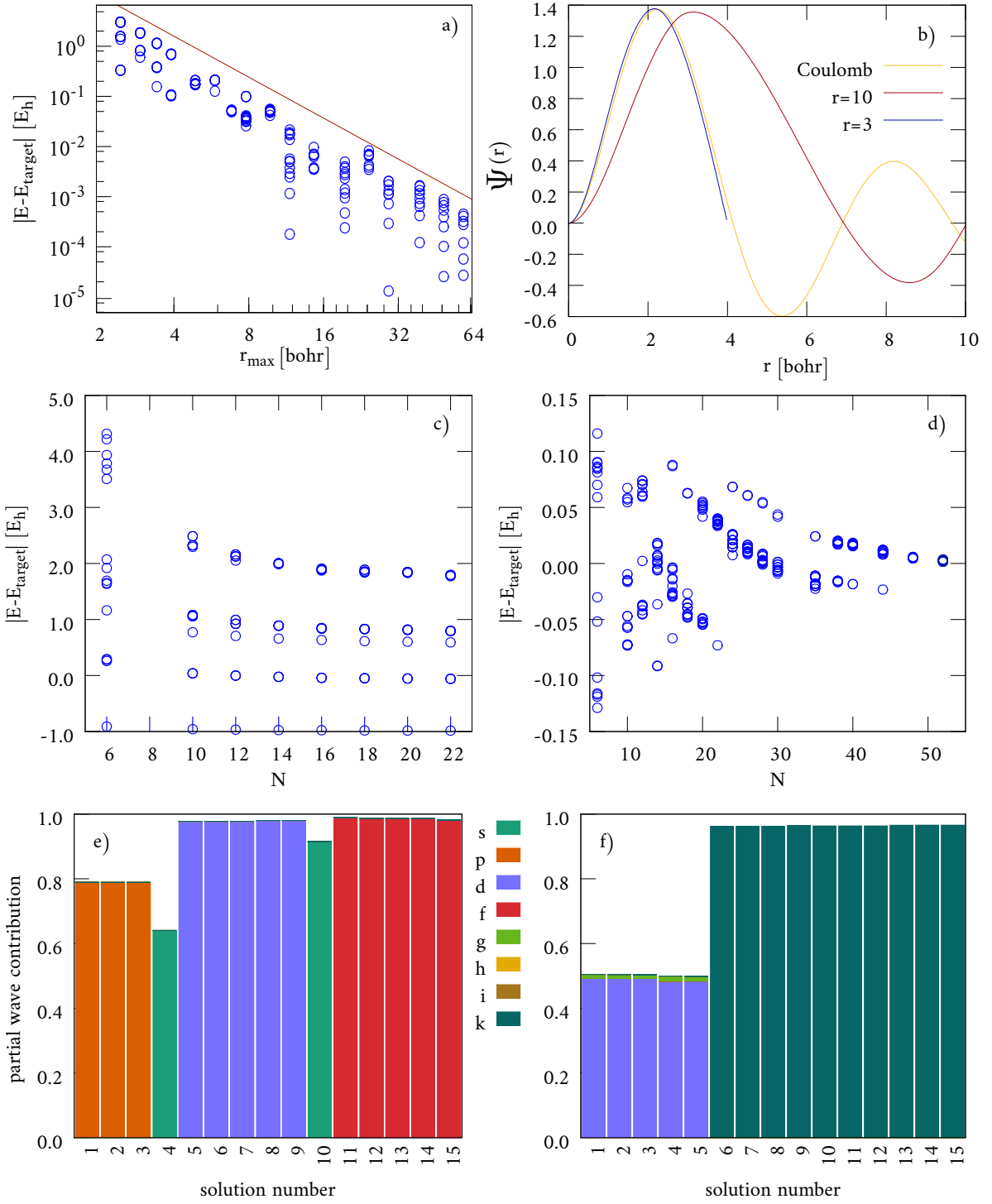


Figure 6.1: Results obtained with Dirichlet BCs using different box sizes: a) double-logarithmic plot from the deviation in energy for the solutions closest to the target energy  $E_{\text{target}} = 0.566$  Hartree as a function of the radius of the simulation box; b) real part of  $d$ -wave functions obtained with different boxes ( $r_{\max} = 4$  bohr and number of spheres  $N = 18$ , blue line and  $r_{\max} = 10$  bohr and  $N = 38$  spheres, red line); Coulomb wave (yellow line) is also presented for comparison; c) and d) show the deviation in energy for box radii of 4 and 10 bohr, varying the number of spheres (radial grid density, see eq.(5.15)) in the box; e) and f) show the partial wave contributions eq.(6.1) having different angular momenta for the the respective solutions with  $r_{\max} = 4$  and  $N = 16$  (left) as well as  $r_{\max} = 10$  and  $N = 38$ , respectively.

onto the quantisation axis  $m$  and  $|\Psi_n\rangle$  denotes the respective numerically obtained solution. The comparison is done against the spherical waves and not against Coulomb waves, since confluent hypergeometric functions are difficult to converge for larger  $r$  and they are much more computationally demanding.

The testcalculations have shown that for the given energy of the photoelectron of  $E = 0.566$  Hartree the obtained solutions have a well-defined angular momentum only for small boxes where the critical radius is in the order of  $r_{\max} = 10$  bohr. For larger computational domains, the states are mixed and have large contributions from much higher angular momenta and are very sensitive to different parameters such as the number of spheres  $N_i$  and the parameters  $s$  and  $q$  in eqs.(5.15) and (5.14) respectively. Moreover, for example the comparison of the Figures 6.1 e) and f) shows that solutions with larger boxes tend to have higher angular momenta which is an important argument in favour of smaller boxes since for most atomic systems angular momenta larger than 4 are not of interest for practical calculations. This tendency can be understood when considering the radial SE [Lifshitz ]

$$\frac{\partial^2}{\partial r^2} R(r) + \left( 2(E - V(r)) - \frac{l(l+1)}{r^2} \right) R(r) = 0 \quad (6.2)$$

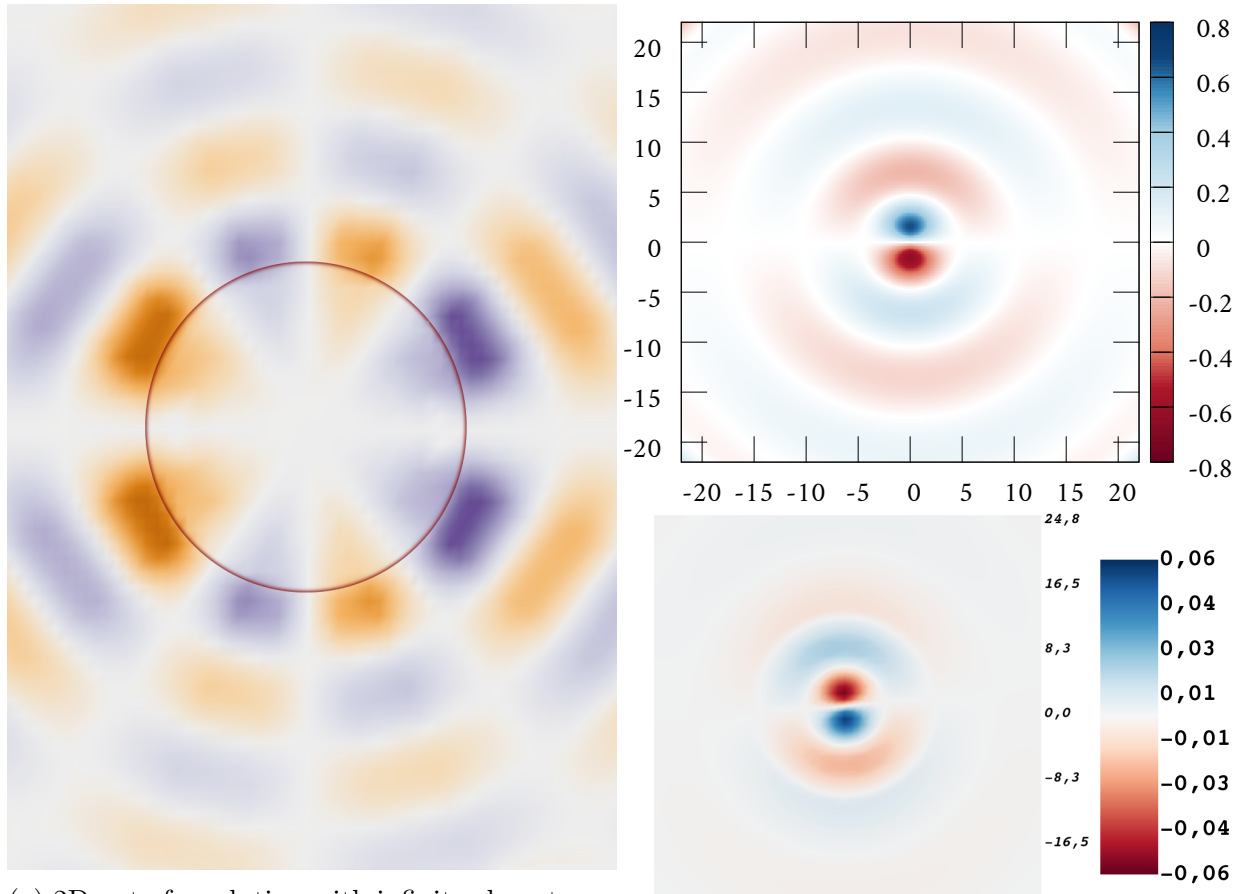
where  $R(r)$  is the radial solution and  $E - V(r)$  is identified as kinetic energy. Thus, given a particular kinetic energy, the radial oscillations are reduced by a larger angular momentum. This leads to the interpretation that a particle can ‘distribute’ its kinetic energy between the radial (outgoing) and spherical contributions. In turn, however, needs a wave with large angular momentum more space and thus these solutions are suppressed in smaller computational domains.

In Figure 6.1 b), two solutions with  $l = 2$  along one axis are shown (the fifth one for  $r = 4$  and the first one for  $r = 10$  which are shown in 6.1 e) and f) as well) for two different box-sizes and compared to the Coulomb wave, being the exact solution for the  $-1/r$  potential. As one can see, depends the reproducability of the radial structure strongly on the size of the box.

### 6.1.2 Infinite Elements

The method making use of infinite elements has more different parameters which can be crucial for the stability of the solution than the Dirichlet BC. Investigations of these dependences is the subject of the present section.

In Figure 6.2b, a 2D-cut of a solution obtained with infinite elements for the Hydrogen atom is shown, the red circle indicates the region of finite elements. The features shown in Figure 6.2b are prototypic for the properties that are found for the infinite elements here. It is clearly visible from the graph that the infinite region resembles the asymptotic behaviour, showing the expected regular oscillations of an outgoing wave. However, the angular momentum is quite large, leading to only small contributions in the finite element region.



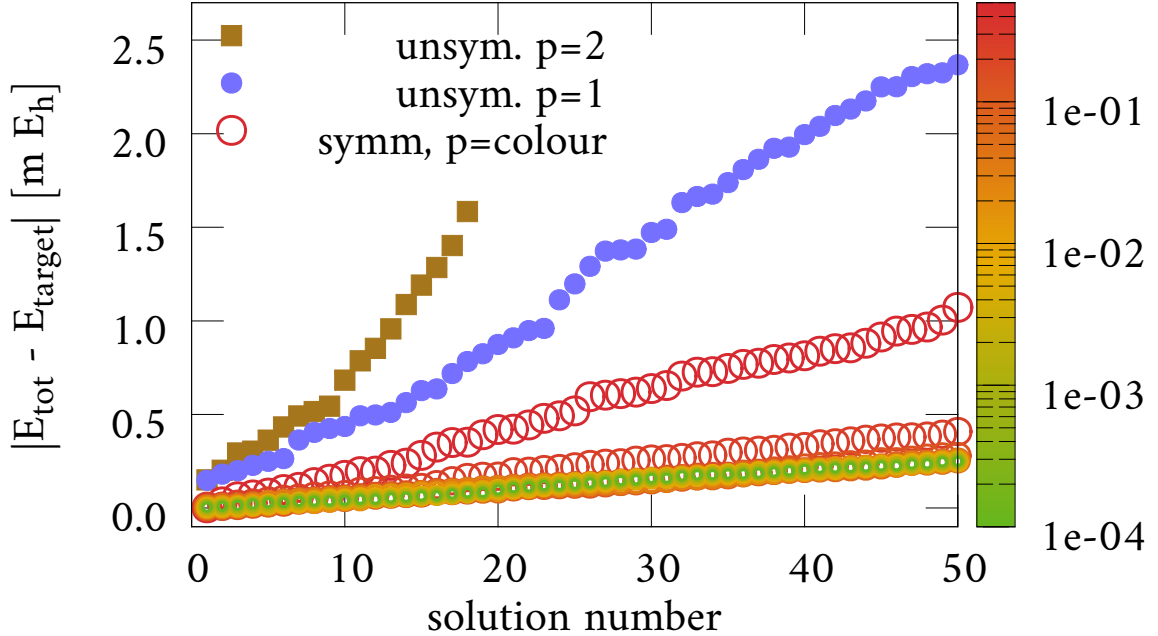


Figure 6.3: The first 50 eigenvalues obtained with the original Astley-Leis formulation (imaginary part not shown) and with the symmetrised form eq.(4.17).

### Comparison of Formulations

Before having a closer look at the convergence of different parameters, first the formulation of infinite elements to be used later is investigated. Since the unconjugated Burnett-formulation was not very successful [42], the conjugated formulations of Burnett and Astley-Leis both have interesting features to use for quantum mechanical problems. Since the conjugated Burnett elements lead to infinitely large matrix elements, here the Astley-Leis elements (4.12) are compared with the symmetrised form (4.17) using different powers  $p$ . Moreover, to study the influence of the damping function in the Astley-Leis formulation (4.12) in more detail, also a test function space similar to eq. (4.12) but using the squared damping function  $D(r)^2$  instead of  $D(r)$ .

The 50 real solutions whose energy is closest to the target value of 15.44 eV ( $0.5675 E_h$ ) obtained with the original Astley-Leis formulations with the damping function taken to the powers  $p = 1, 2$  as well as the symmetrised formulation (4.17) suggested in this thesis with powers  $p < 0.5$  are shown in Figure 6.3. For the unsymmetric formulations only the real part is shown which is assigned to the physical energy of the respective state. The results shown in Figure 6.3 show clearly that the obtained density of states decreases with the power  $p$  and converges for  $p \approx \frac{1}{8}$  for the given parameters (the radial mapping scheme (5.15) is used with  $N = 25$ ,  $l = 0.5$ ,  $p = 2.5$  and  $r_{\max} = 7$  bohr.).

The dependence of the obtained spectrum of the Hamiltonian on the power of the damping function shows that, at least for FEFs, the asymptotic behaviour is crucial for the properties of the wave function. The dependence converges for  $p = 1/8$ , see also Figure A.3 in supplement. Moreover, even for small powers  $p \approx 10^{-4}$ , no numerical instabilities are observable so that there is some freedom in this parameter and it does not need to be optimised for different systems individually. The observations made on the

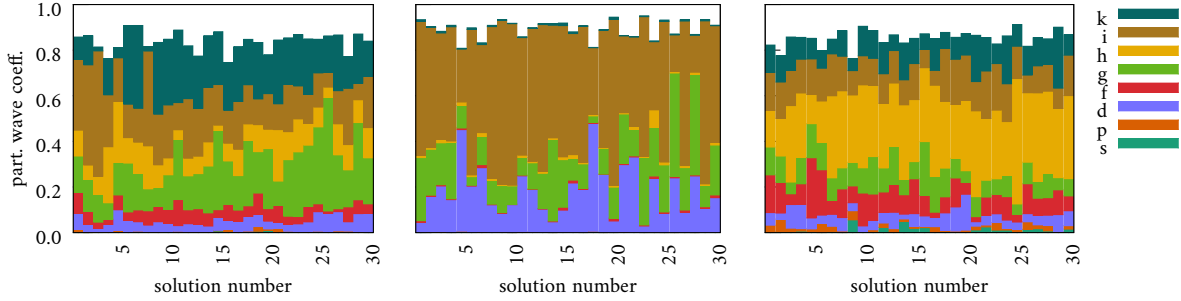


Figure 6.4: Decomposition of the first 30 solutions into spherical waves with angular momenta up to  $l = 7$ . Left: Astley-Leis-formulation ( $p = 1$ ), middle: symmetrised form ( $p = 0.5$ ) right: symmetrised form ( $p = 10^{-4}$ ).

convergence-properties using the spectrum in Figure 6.3 are supported by the projections of the solutions on spherical waves of which some are shown in Figure 6.4.

As shown in the Figure 6.4, the nature of the states obtained is in all cases strongly mixed in the quantum number  $l$  with significant contributions even for  $l > 7$ . However, the relative contributions of the angular momenta critically depends on the power  $p$ , making a reasonable choice of this parameter important. Further it is expected that the convergence of  $p$  depends on further parameters such as the box-size and kinetic energy of the photoelectron which is, however, not studied here in more detail. Instead, in the following the power of the damping function  $D$  is chosen to be  $p = 0.0001$  if not specified differently. This value is far in the convergence region of Figure 6.4 and thus is hoped to be reasonable also for other systems.

### Radius of the Finite Element Region

Similarly to the Dirichlet BCs discussed in section 6.1.1, also for infinite element the size of the finite element region has a strong influence on the solution, even if the dependency is weaker as can be seen in Figure 6.5 where the energy of the energies closest to the target value is plotted for different box sizes. However, the energy-dependence on the box-size is much weaker than in the case of Dirichlet BCs as the comparison with the  $\frac{1}{r^3}$ -curve in Figure 6.5 and 6.1 (a) shows. Moreover, the error in energy is in general much lower with infinite elements which is a further indicate for the higher accuracy of infinite elements compared to the Dirichlet boundaries. On the other side, also the angular momenta of the solutions are larger than those occurring with Dirichlet BC at the same box-size. This behaviour is observed to depend also on the formulation of infinite elements. Respective tests show, *e.g.*, that the mixing of angular momenta is stronger for smaller damping powers  $p$ . This coupling of different angular momenta can be explained by the very density of the spectrum which increases with the radius as shown *e.g.* in Figure 6.6 but increases also with descending damping as illustrated in Figure 6.4.

This behaviour can be understood when recapitulating the influence of small perturbations (*e.g.* due to numerical cut-off) in form of a matrix  $\mathbb{E}$  of an hermitian matrix to its eigenvectors  $\mathbf{u}_i$  which has the form [276, 277]

$$\mathbf{u}'_i = \sum_{j \neq i} \frac{\mathbf{u}_j^\dagger \mathbb{E} \mathbf{u}_i}{\lambda_i - \lambda_j} \mathbf{u}_j \quad (6.3)$$

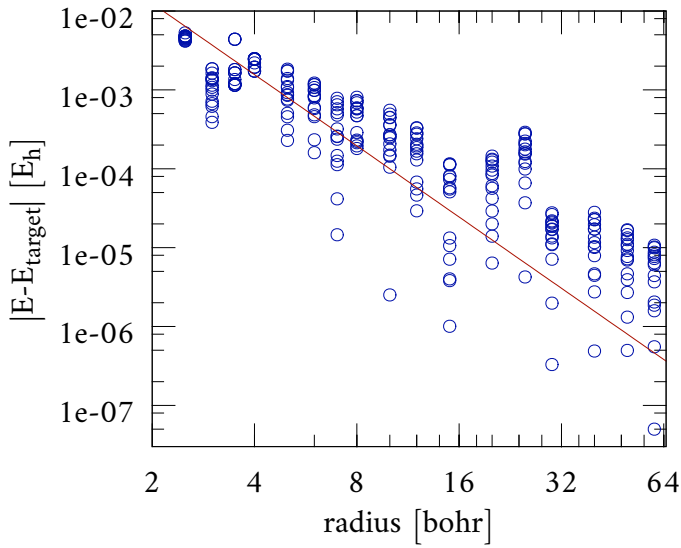


Figure 6.5: Double-logarithmic plot of the error in energy for different radii of the finite element region.

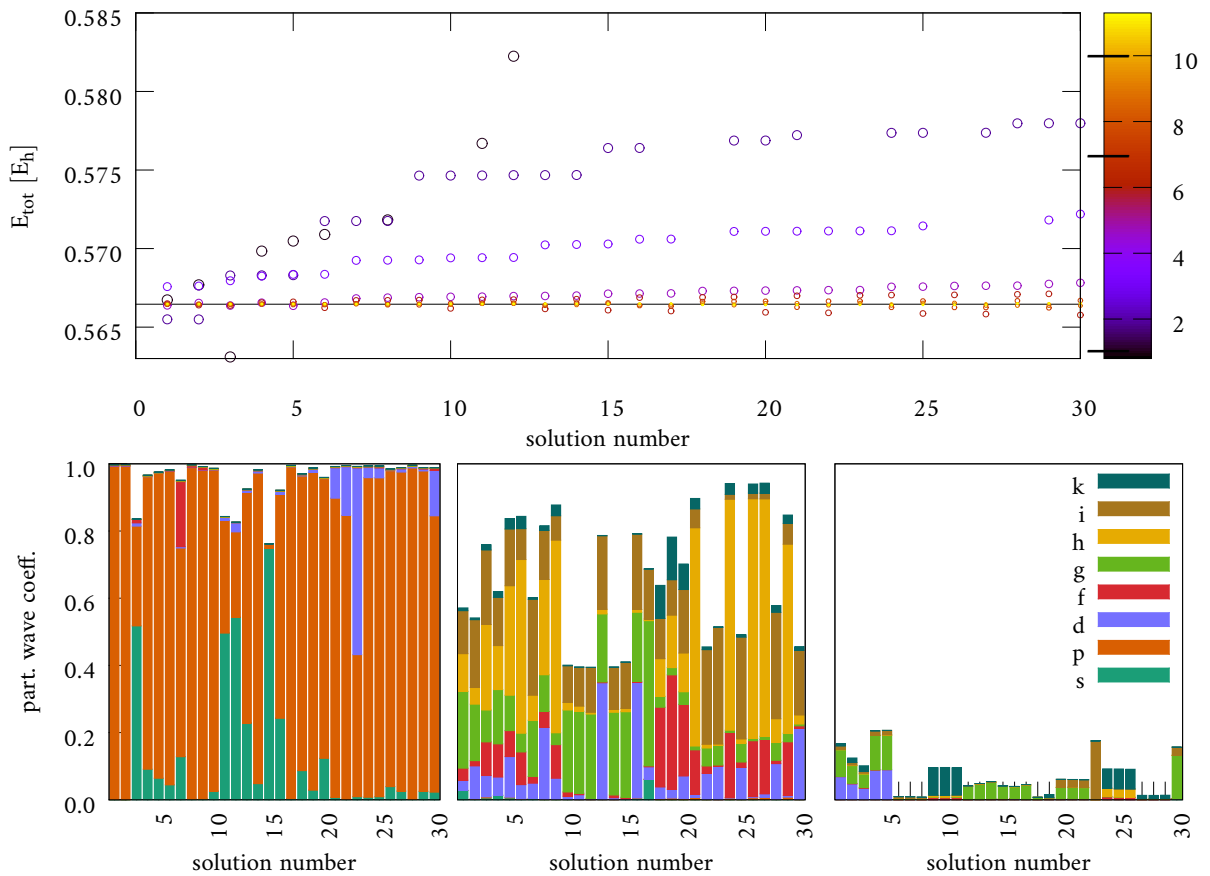


Figure 6.6: The eigenenergies for different box sizes (coloured dots in the upper panel) where the box size is denoted by the colour in atomic units. The lower panel shows the decomposition of the solutions into spherical waves for three box sizes, marked by a star in the colour bar respectively.

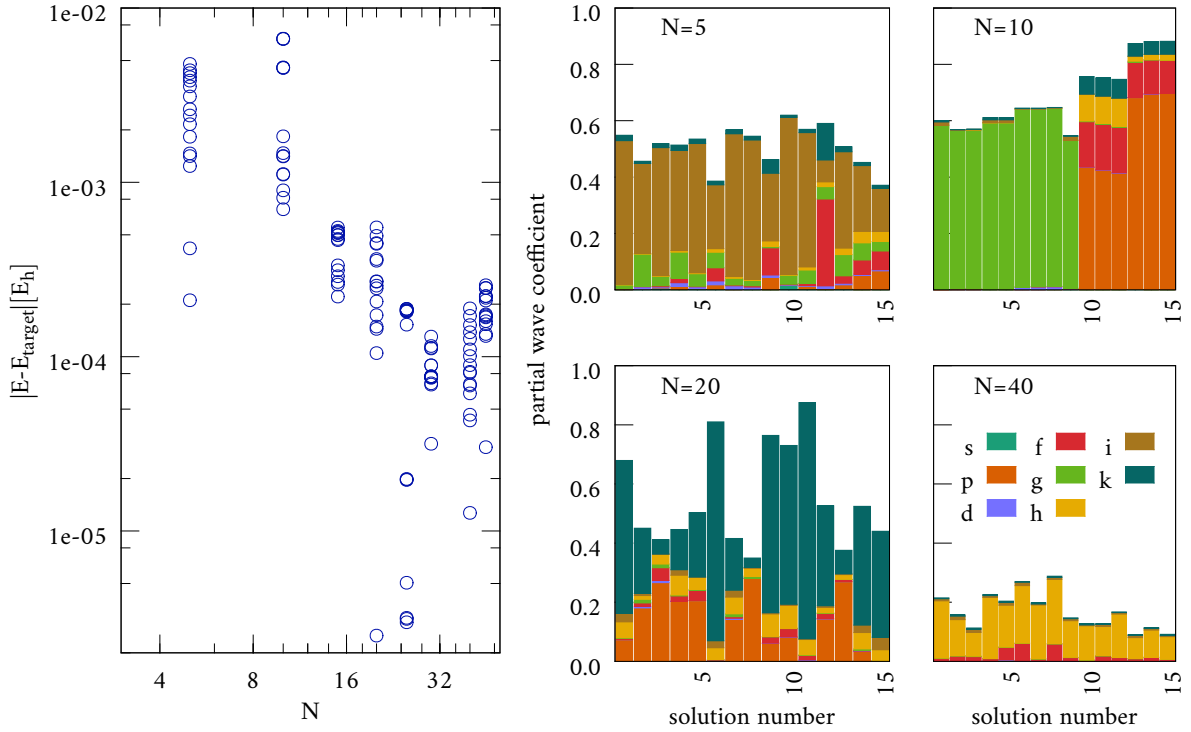


Figure 6.7: The energy (left panel) and partial wave coefficient (6.1) for different number of spheres  $N$  using infinite elements. The radius is  $r = 10$  bohr.

where  $\lambda_i$  is the eigenvector corresponding to  $\mathbf{u}_i$ . From eq. (6.3) now the coupling of angular momenta and strong dependence on the parameters for a dense spectrum, *i.e.* small  $\lambda_i - \lambda_j$  becomes obvious.

## Density of Spheres

Increasing the number of spheres has, as expected, some influence on the energies but also changes the angular momenta of the solutions. Similar to the behaviour found for Dirichlet BCs, also when using infinite element BCs a larger number of spheres leads to larger angular momenta as the comparison of the partial wave coefficients in Figure 6.7 for different numbers of spheres shows. Moreover, the error of the energy shown on the left side of Figure 6.7 indicates that the shown configurations are far from saturation. However, since high angular momenta are not desireable, a smaller number of spheres is better suited even though it is not converged. Moreover, the behaviour of the properties of the solutions when changing the number of spheres is not very systematic in the range shown. As an example, for  $N = 10$  the energies are much more separated than is reflected also in the angular momenta which show a much weaker mixing than for the other configurations shown. Not only the unsystematic behaviour, the strong dependence of the angular momentum on the number of spheres as such is surprising since, in principle, the radial and angular nodes should be represented with a similar quality.

## Radial Order

Using the infinite element scheme, an additional parameter is the order of the radial polynomial  $f(r)$  in eq. 4.10. The increasing angular momentum with the radial order

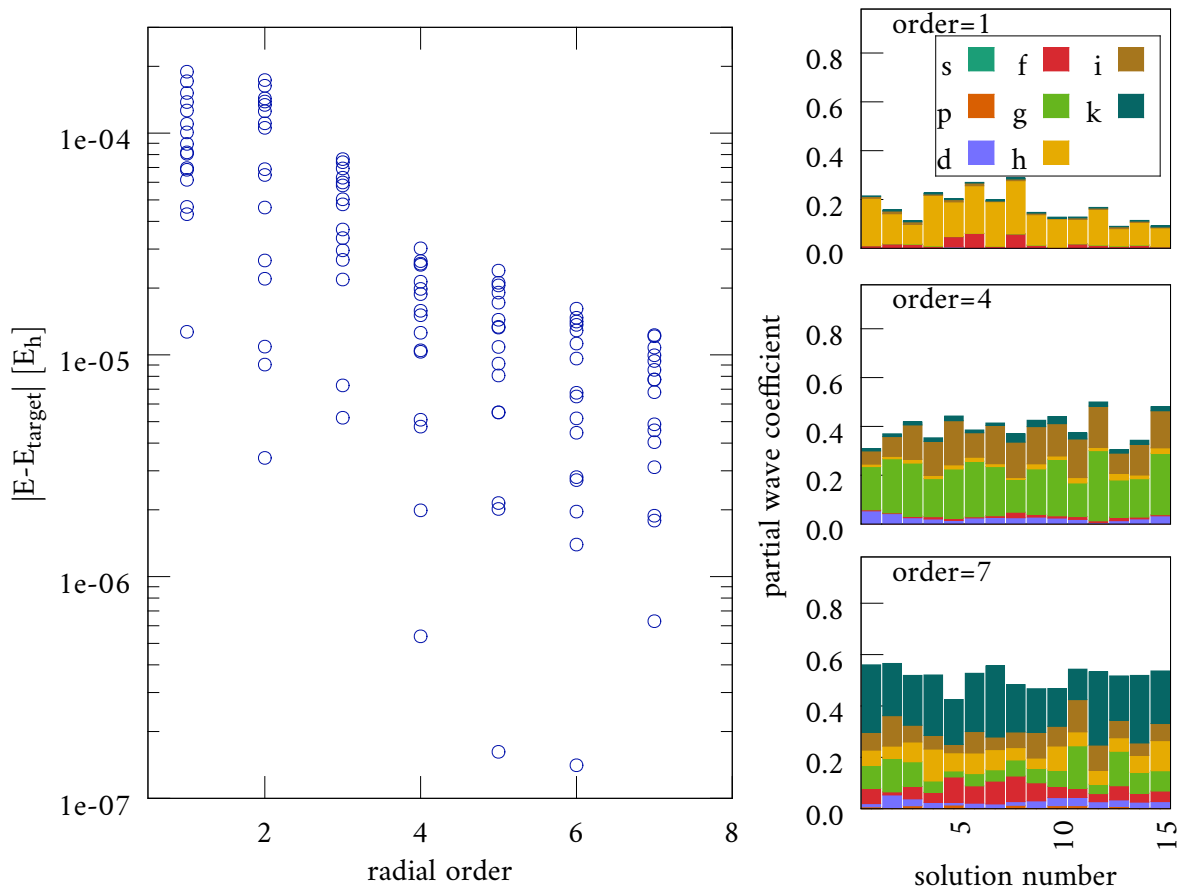


Figure 6.8: The error in energy for 15 solutions obtained with a box with radius  $r = 10$  and  $N = 40$  spheres using different orders of the multipole expansion  $f(r)$ , see eq. (4.10).

is, in contrast to the behaviour studied in section 6.1.2, not surprising. As mentioned in section 4.4.4, the first order infinite element term corresponds to the radial behaviour of an  $s$ -wave whereas higher radial orders describe the faster decaying waves with respectively larger angular momentum. Thus, choosing a low radial order ( $o = 1$ ) leads to a better representation of low angular momenta and thus is favoured in this context.

### 6.1.3 Conclusion on Boundary Conditions

The study of different system-parameters presented in the previous sections has revealed several properties of the finite element setup. An important conclusion of these tests is that a higher density of eigenenergies, which is considered as an indication for a more exact representation of the wave function, in general leads to the appearance of larger angular momenta and, at some point, to strong coupling of different angular momenta. Such a relation is expected for the box-size since a large angular momentum is accompanied by a larger radius, whereas the strong dependence on the number of spheres shown in Figure 6.7 was not clear in the beginning.

Hence, these studies show that a systematic setup of reasonable parameters is non-trivial and needs to ... the compromise between a dense spectrum and reasonable radial dependence of the wave function on the one side low angular momenta and well-behaved solution on the other side. It is important to note the importance of the systematic character for such a setup since the computation of a single PES requires the computation of photoelectrons whose kinetic energy may vary over orders of magnitude and thus the box needs to be adapted to this.

## 6.2 Numerical Benchmarks and Stability Tests

### 6.3 Energy-dependence of the Cross-Section

The relative heights of different features in PESs are dependent on the energy of the incoming photons. This dependence is small if the kinetic energy of the outgoing electron is high, but for low kinetic energies, *i.e.* below  $\approx 10\text{ eV}$ , the reproduction of the correct energy-dependence is important for a theoretical method to be able to predict the intensities in the PESs reliably. In the DO formalism, this dependency is accounted for via the dipole moment integral of the photoelectron with the DO in eq.(2.16). The main influence of this integral is the fact that the oscillations in the FEF become faster with increasing kinetic energy and thus, the overlap with the DO, which usually has only few nodes, decreases. The slope of the decay with increasing photon energy thus contains information about the size of the DO because for a broad and unstructured DO, the oscillations cancel most contributions out whereas a strongly localised DO is less sensitive to the wavelength. Thus, the dependence of the intensity of a peak on the photon energy contains information on the nature of the transition. Hence, it is another important property that is studied in several experimental and theoretical works [278–280]. In this work, the cross section of the valence-transition of lithium as well as [four!](#)? transitions of  $\text{CO}_2$  are studied.

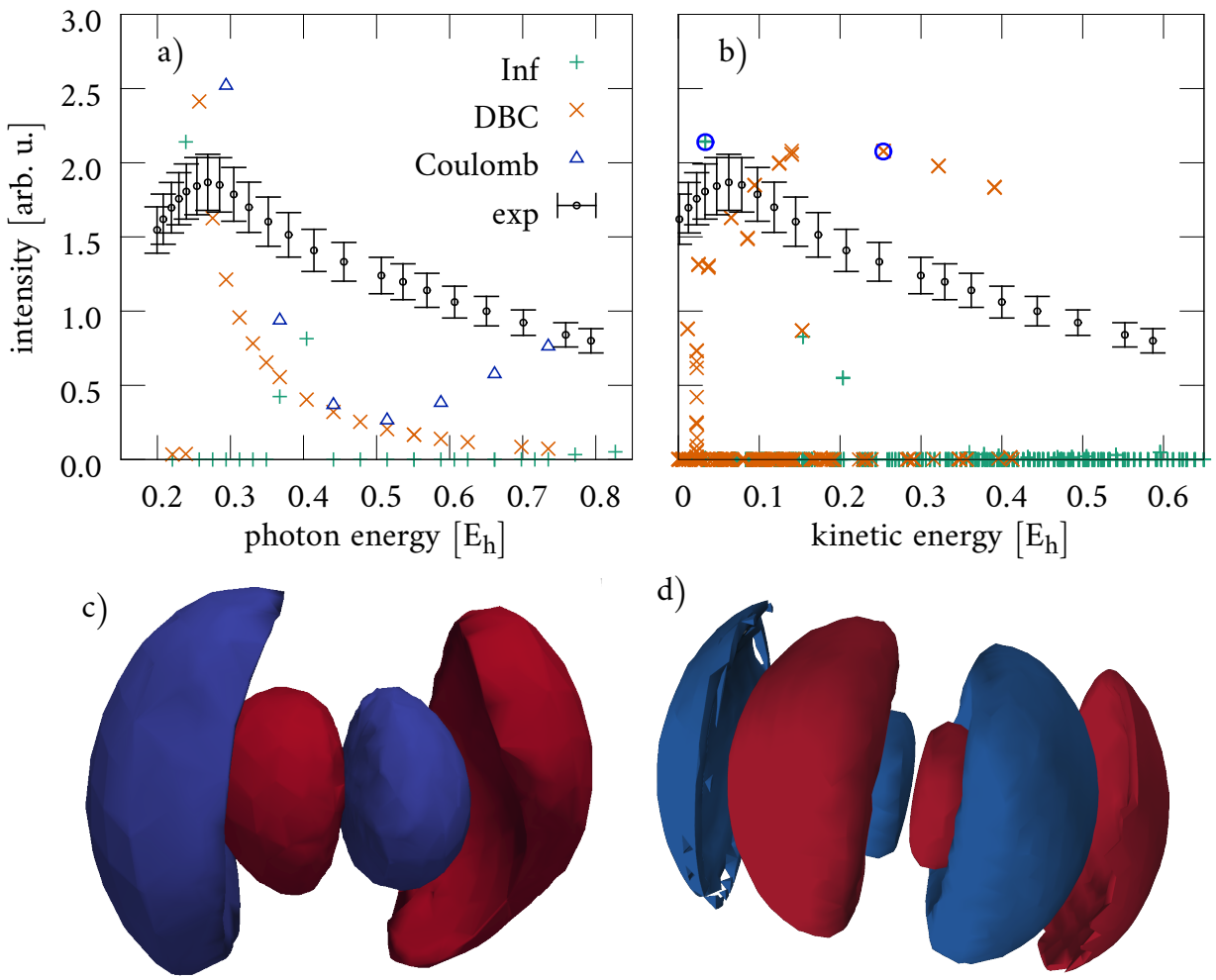


Figure 6.9: The photoelectron cross section of the lithium atom as a function of the photon energy obtained the FEM (Dirichlet BCs (DBC) and infinite elements (inf)) and the Coulomb wave expansion (Coulomb), compared to experiment [279]. Left panel: The intensity is computed as sum over the intensities of 80 FEFs; Right panel: The intensities of single FEFs are shown. Top panel: contour plots of the FEFs with the largest contributions. Left: with Dirichlet BC, right: with infinite elements. The respective transitions are marked with a circle in the plot.

In Figure 6.9, the intensity of the valence transition of lithium (binding energy of  $E_b = 0.2067$ ) is shown as a function of the photon energy. Since the kinetic energy (and thus the wavelength) of the particle spans over a very broad range, the setup for the computation of the FEF needs to be adapted to the particular kinetic energy. As the studies in section 6.1 showed, is the box-size very critical to the properties of the solution. It may not be too small to ensure a reasonable error in energy, but should not be too large to have considerable contributions of low angular momenta that is crucial for the computation of intensities. To account for this, for the calculations presented in Figure 6.9, the box-size was choosen to be  $0.8\lambda$  in case of Dirichlet BC and  $0.5\lambda$  for infinite elments, where  $\lambda$  is the asymptotic wavelength (*i.e.* reached outside the influence of the Coulomb potential) of the respective target energy. The box-size smaller than  $\lambda$  in case of Dirichlet BCs is too small for a reasonable error in energy but show, since the wavelength is considerably smaller in the presence of a Coulomb potential, still some radial nodes. For all setups,  $N = 18$  spheres and the radial mapping scheme  $tm$ , eq.(5.15), with the

parameters  $q = 2.5$  and  $s = 1.2$  was used, respectively. For the infinite elements the radial polynomial is truncated after the first order to suppress higher angular momenta.

The intensities obtained with the finite element scheme are presented in two different ways in Figure 6.9. In the left panel, the 80 energetically closest intensities are summed up whereas in the right panel the individual intensities are shown. The theoretical results are scaled to be in good agreement with the experimental data. For the results obtained with the Dirichlet BCs, the summed intensities (left panel of Figure 6.9) show a systematic but qualitatively wrong behaviour which can be explained by the box which is considerably too small to ensure the correct shape of the wave-function. However, the intensities of the single transitions (right panel of Figure 6.9) have a different progression. The qualitative difference between these schemes can be explained by the fact that in the right pannel at lower kinetic energies many transitions contribute with a considerable intensity whereas at higher kintetic energies only few solutions contribute. Moreover, the transitions can be strongly reordered between the graphs since deviations between the target energy and eigenenergy of up to 0.11 Hartree occur.

The results obtained with infinite elements show a less systematic behaviour: Among the hundreds of solutions computed, only three contribute significantly to the cross section. The scaling factor of the transitions shown in the right panel of Figure 6.9 are 0.7 for the soltions obtained with the Dirichlet BC and 0.4 for those computed with infinite elements, thus their relative scale is in the same order of magnitude. These results show that, even for a small computational domain as it is used here, only a poor agreement with the experiment is achievable. In case of Dirichlet BCs, the bad agreement with the experimental data can be explained by the size of the box which restricts the solution to low angular momenta but introduces a large error in the shape of the wave function and thus influences the dipole matrix elements considerably. A study with a more reasonable radius of  $r_{\max} = 3.5\lambda$  was conducted as well and is shown in Figure A.4. However, even though the eigenenergies are denser and the wave function are more flexible, only few transitions with considerable intensity were obtained. Another important question concerns the normalisation of the wave function.

In the case of infinite elements, too few transitions contributing to the intensity are obtained for an analysis of their kinetic-energy dependence. However, this shows that even for such a small box, the angular momentum is in general too high to give considerable contributions, at least for  $s$ -type DOs.

- Explain, why a systematic setup over such a wide range of kinetic energies is not possible for the given scheme. This problem can be seen esp. for DBC comparing left and right of 6.9.

This should be already the main reason for the unsystematic results!?

The intensities obtained with the Coulomb wave function are, similar to the results obtained with the FEM and Dirichlet BC, in poor agreement with the experimental data. Since the ESP of lithium is very close to that of hydrogen, this is surprising. Moreover, the shape makes no sense at all.

For the computation of the overlap integral, only the finite region is taken into account since outside of it the DO vanishes and thus the outer region would not lead to further contributions. In this region usually, the wave function is normalised to one which is,

especially in the case of Dirichlet boundary conditions, the usual normalisation. However, if the intensities obtained with different box-sizes are to be compared, two wave functions that coincide in the central region but are computed on differently large regions would result in different intensities. To account for this, here the wave functions are normalised to the volume, *i.e.*

$$\int_V |\Psi_n(\mathbf{r})|^2 d\mathbf{r} = \int d\mathbf{r} = V \quad (6.4)$$

where  $V$  is the volume of the finite element region.

For the second testing-system, here first the PES as a whole should be discussed.

- assign transitions
- The first IP is reproduced well, due to OTRSH-scheme used.
- The positions of the other bands are stretched
- A considerable part of the features not reproduced, since vibronic progression is not studied here;
- SA and DOS are similar (?) integration changes heights -*i*. improves agreement with experiment.

For the first two transitions, that correspond to degenerate DOs with  $\pi$ -character respectively, here also the cross section dependence on the photon energy is studied. In Figure ??, the energy-dependence of the first two transitions shown in Figure that showing the PES is shown as obtained with various theoretical methods. Comparing the results obtained with the multiple scattering method citation and the Stieltjes imaging approach [280], a reasonable agreement is achieved. Both approaches reproduce the main behaviour of the function. However, for small kinetic energies, both methods do not reproduce the experimental data that well. The larger problems in case of the  $\pi_g$ -transition (Figure ??) can be explained by the higher binding energy of ... and thus lower kinetic energy compared to the  $\pi_u$ -transition whose cross section is shown in Figure ??.

- Qualitative agreement in case of Stieltje, Mult. Scattering and also Coulomb
- The good quality of Coulomb is surprising
- The general trend can be seen in case of the  $\pi_g$ -transition
- The  $p_{i_u}$ -transition has completely wrong behaviour
- in both cases not systematic.

First show spectra for CO<sub>2</sub>. Figure 6.11 shows the PES of benzene obtained with this setup using a grid of height (orthogonal to the molecular plane) of 8 Å and a diameter of 12 Å in both directions of the molecular plane with 380 points in each direction. The expansion of Coulomb waves includes the terms up to an angular momentum of  $l = 10$ . The second spectrum shown in To indicate the consequences of the OTRSH procedure, in Figure ?? the PES of benzene as predicted with the optimised functional and the B3LYP functional are shown. For this system, the agreement is good, for other systems the differences are much larger as the example of S<sub>8</sub> in the supplement shows. OTRSH is known no be not very good for linear molecules -*i*. is there some reason for this?

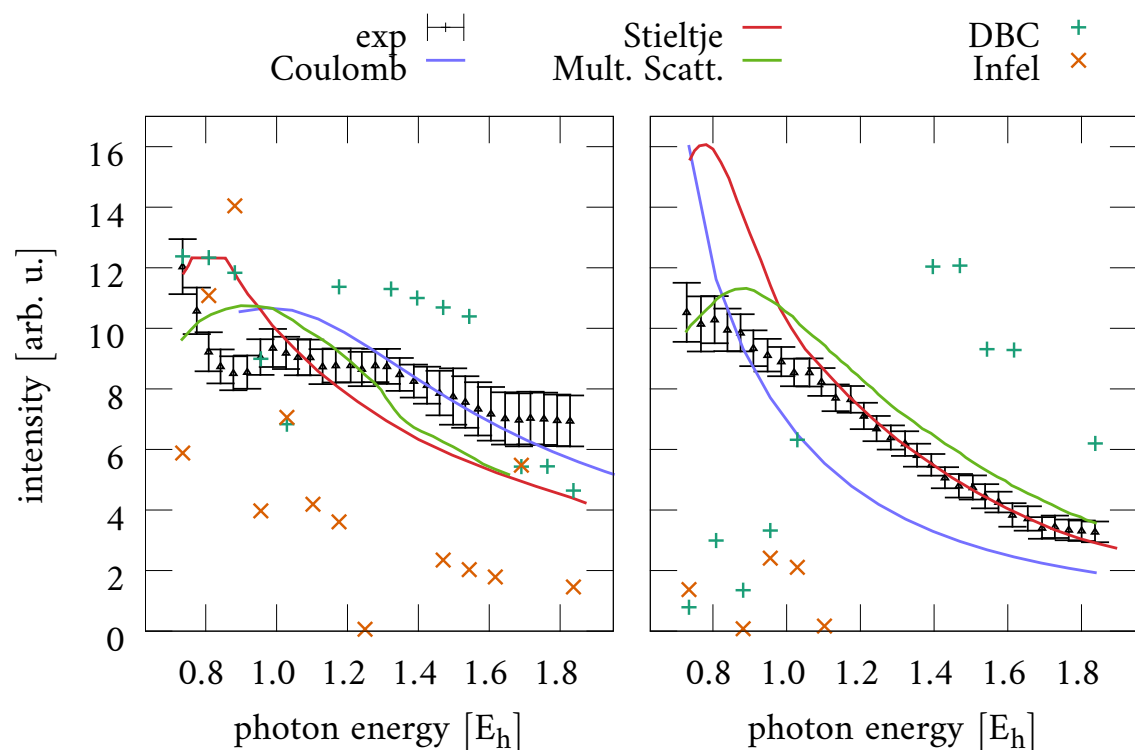


Figure 6.10: Add labels!

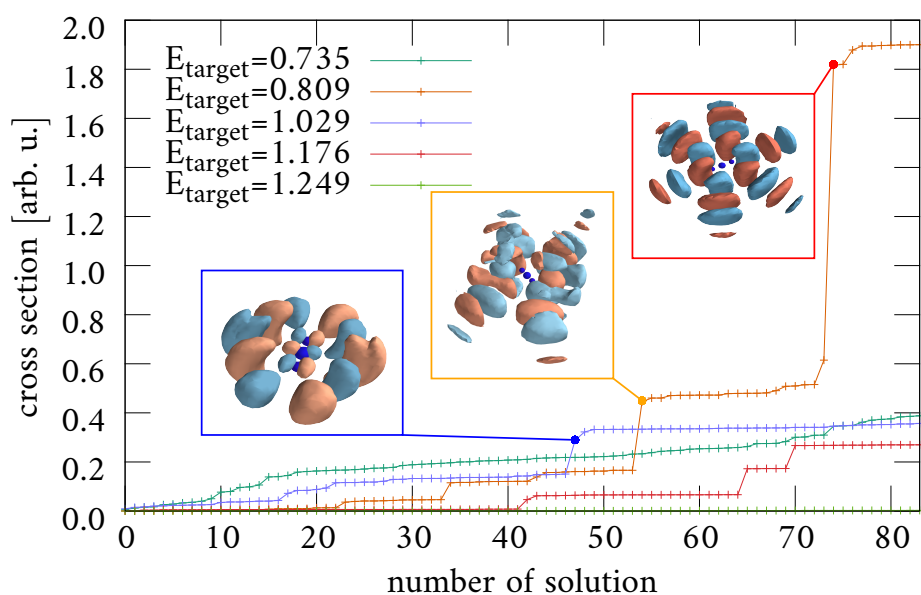


Figure 6.11: Convergence of intensities for the  $\pi_g$ -transition of  $\text{CO}_2$ .

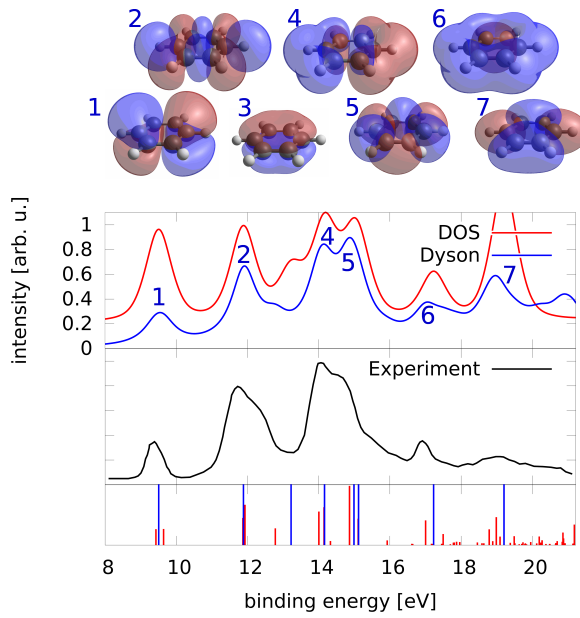


Figure 6.12: Photoelectron spectra of benzene at different levels of theory. In the upper panel the spectra obtained with the Dyson orbital formalism (Dyson) and using the Koopmans' approach (DOS) are compared, the experimental reference is shown in the lower panel [281].

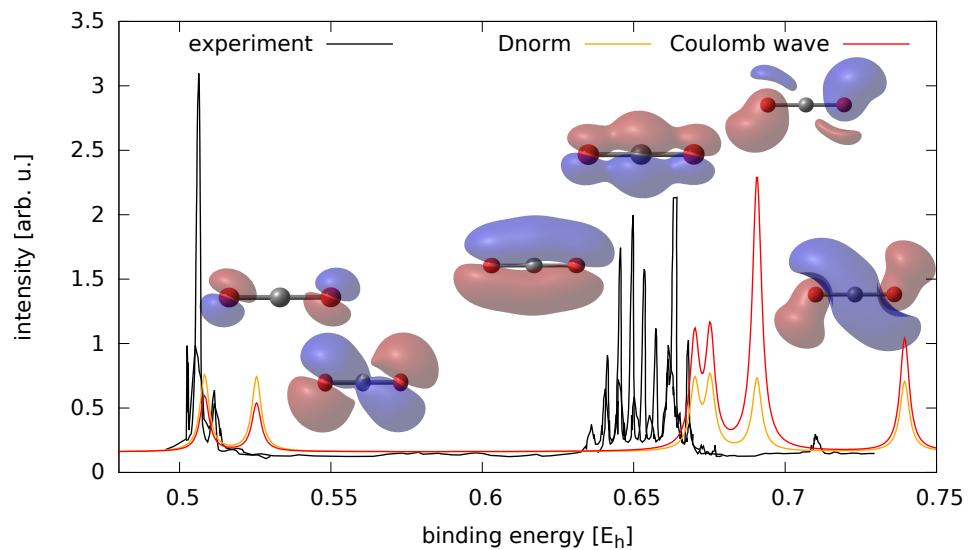


Figure 6.13: I forgot about this degeneracy!!!!!!

# 7 | Resumee

## 7.0.1 Boundary condition

The dependence of density of eigenenergies to size/mixing of angular momentum can also hold for the different formulations of infinite elements, compared in section 6.1.2, as well. Thus, a comparison of the different formulations could be redone under this aspect, probably leading to better results. However, previous studies that are not presented in this work have shown that the Astley-Leis elements leads to similar problems which initially motivated the symmetric formulation.

- is it worth the effort? - What energy-range is achievable? - Which effects are still missing?
- How to proceed with it?

# Bibliography

- [1] B. Winter et al. “Full Valence Band Photoemission from Liquid Water Using EUV Synchrotron Radiation”. In: *J. Phys. Chem. A* 108.14 (Apr. 2004), pp. 2625–2632.
- [2] K. M. Lange and E. F. Aziz. “The Hydrogen Bond of Water from the Perspective of Soft X-Ray Spectroscopy”. In: *Chem-Asian J.* 8.2 (2013), pp. 318–327.
- [3] S. E. Canton et al. “Visualizing the non-equilibrium dynamics of photoinduced intramolecular electron transfer with femtosecond X-ray pulses”. In: *Nat. Comm.* 6.6359 (Mar. 2015).
- [4] H. Hafied et al. “Electron momentum spectroscopy of the valence orbitals of the water molecule in gas and liquid phase: A comparative study”. In: *Chem. Phys. Letters* 439.1 (May 2007), pp. 55–59.
- [5] B. E. Van Kuiken and M. Khalil. “Simulating Picosecond Iron K-Edge X-ray Absorption Spectra by ab Initio Methods To Study Photoinduced Changes in the Electronic Structure of Fe(II) Spin Crossover Complexes”. In: *J. Phys. Chem. A* 115.39 (2011), pp. 10749–10761.
- [6] X. Yang et al. “Solvation of the Azide Anion (N<sub>3</sub><sup>-</sup>) in Water Clusters and Aqueous Interfaces: A Combined Investigation by Photoelectron Spectroscopy, Density Functional Calculations, and Molecular Dynamics Simulations”. In: *J. Phys. Chem. A* 108.39 (2004), pp. 7820–7826.
- [7] B. Minofar et al. “Interior and Interfacial Aqueous Solvation of Benzene Dicarboxylate Dianions and Their Methylated Analogues: A Combined Molecular Dynamics and Photoelectron Spectroscopy Study”. In: *J. Phys. Chem. A* 109.23 (2005), pp. 5042–5049.
- [8] S. Thürmer et al. “Flexible H<sub>2</sub>O<sub>2</sub> in Water: Electronic Structure from Photoelectron Spectroscopy and Ab Initio Calculations”. In: *J. Phys. Chem. A* 115.23 (2011), pp. 6239–6249.
- [9] M. Etinski and C. M. Marian. “Ab initio investigation of the methylation and hydration effects on the electronic spectra of uracil and thymine”. In: *Phys. Chem. Chem. Phys.* 12 (19 2010), pp. 4915–4923.
- [10] F. Lépine et al. “Molecular applications of attosecond laser pulses”. In: *Chem. Phys. Lett.* 578 (July 18, 2013), pp. 1–14.
- [11] E. Goulielmakis et al. “Real time observation of valence electron motion”. In: *Nature* 466 (Aug. 5, 2010), pp. 739–744.
- [12] D. G. Sansone et al. “Electron Correlation in Real Time”. In: *Chem. Phys. Chem.* 13.3 (2012), pp. 661–680.

- [13] M. F. Kling and M. J. Vrakking. “Attosecond Electron Dynamics”. In: *Annu. Rev. Phys. Chem.* 59.1 (May 2008), pp. 463–492.
- [14] M. Uiberacker et al. “Attosecond real-time observation of electron tunnelling in atoms”. In: *Nature* 446.7136 (Apr. 5, 2007), pp. 627–632.
- [15] F. Krausz and M. Ivanov. “Attosecond physics”. In: *Rev. Mod. Phys.* 81.1 (Feb. 2, 2009), pp. 163–234.
- [16] T. Koopmans. “Über die Zuordnung von Wellenfunktionen und Eigenwerten zu den Einzelnen Elektronen Eines Atoms”. In: *Physica* 1.1 (1934), pp. 104–113.
- [17] C.-O. Almbladh and U. von Barth. “Exact results for the charge and spin densities, exchange-correlation potentials, and density-functional eigenvalues”. In: *Phys. Rev. B* 31 (6 Mar. 1985), pp. 3231–3244.
- [18] D. A. Egger et al. “Outer-valence Electron Spectra of Prototypical Aromatic Heterocycles from an Optimally Tuned Range-Separated Hybrid Functional”. In: *J. Chem. Theory. Comput.* 10.5 (2014), pp. 1934–1952.
- [19] T. Körzdörfer et al. “Assessment of the performance of tuned range-separated hybrid density functionals in predicting accurate quasiparticle spectra”. In: *Phys. Rev. B* 86 (20 Nov. 2012), p. 205110.
- [20] T. Körzdörfer et al. “When to trust photoelectron spectra from Kohn-Sham eigenvalues: The case of organic semiconductors”. In: *Phys. Rev. B* 79 (20 May 2009), p. 201205.
- [21] C.-Z. Gao et al. “On the dynamics of photo-electrons in C 60”. In: *J Phys. B-A. Mol. Opt.* 48.10 (2015), p. 105102.
- [22] Y. N. Zhuravlev and D. V. Korabelnikov. “The nature of the electronic states and photoelectron spectra of oxyanion crystals”. In: *J. Struct. Chem+* 50.6 (2009), pp. 1021–1028.
- [23] R. Leckey. “Ultraviolet Photoelectron Spectroscopy of Solids”. In: *Surface Analysis Methods in Materials Science*. Ed. by D. J. O’Connor et al. Berlin, Heidelberg: Springer Berlin Heidelberg, 1992, pp. 291–300.
- [24] J. Schirmer et al. “Break-down of the molecular-orbital picture of ionization: CS, PN and P 2”. In: *J. Phys. B- At. Mol. Opt.* 11.11 (1978), p. 1901.
- [25] J. Schirmer et al. “Strong Correlation Effects in inner Valence Ionization of N<sub>2</sub> and CO”. In: *Chem. Phys.* 26.1 (1977), pp. 149–153.
- [26] M. Brosolo and P. Decleva. “Variational approach to continuum orbitals in a spline basis: An application to H<sub>2</sub>+ photoionization”. In: *Chem. Phys.* 159.2 (Jan. 1992), pp. 185–196.
- [27] A. Abdurrouf and F. H. M. Faisal. “Theory of intense-field dynamic alignment and high-order harmonic generation from coherently rotating molecules and interpretation of intense-field ultrafast pump-probe experiments”. In: *Phys. Rev. A* 79 (2 Feb. 2009), p. 023405.

- [28] P. Zhang and A. G. R. Thomas. “Enhancement of high-order harmonic generation in intense laser interactions with solid density plasma by multiple reflections and harmonic amplification”. In: *App. Phys. Lett.* 106.13 (Mar. 30, 2015), p. 131102.
- [29] B. Dromey et al. “High harmonic generation in the relativistic limit”. In: *Nature Phys.* 2.7 (July 2006), pp. 456–459.
- [30] E. Fermi. *Nuclear Physics*. Chicago: University of Chicago Press, 1949.
- [31] B. Sonntag and P. Zimmermann. “XUV spectroscopy of metal atoms”. In: *Rep. Prog. Phys.* 55.7 (1992), p. 911.
- [32] G. Grell. “Theoretical Study of X-Ray Photoelectron Spectroscopy of Transition Metal Complexes”. University of Rostock, 2015.
- [33] L. D. Landau and E. Lifschitz. *Quantenmechanik*. 9th ed. Berlin: Akademie-Verlag, 1979.
- [34] C. M. Oana and A. I. Krylov. “Cross sections and photoelectron angular distributions in photodetachment from negative ions using equation-of-motion coupled-cluster Dyson orbitals”. In: *J. Chem. Phys.* 131.12, 124114 (2009).
- [35] Y. Liu and C. Ning. “Calculation of photodetachment cross sections and photo-electron angular distributions of negative ions using density functional theory”. In: *J. Chem. Phys.* 143.14 (Oct. 14, 2015), p. 144310.
- [36] D. Braess. *Finite Elemente*. 4th ed. Heidelberg: Springer, 2007.
- [37] D. Gilbarg. *Elliptic Partial Differential Equations of Second Order*. Berlin: 1983, 1983.
- [38] P. G. Ciarlet. *The Finite Element Method for Elliptic Problems*. Amsterdam et al.: SIAM, 2002.
- [39] R. J. Astley. “Wave envelope and infinite elements for acoustical radiation”. In: *Int. J. Numer. Meth. Fl.* 3.5 (1983), pp. 507–526.
- [40] R. J. Astley et al. “Three-dimensional wave-envelope elements of variable order for acoustic radiation and scattering. Part I. Formulation in the frequency domain”. In: *J. Acoust. Soc. Am.* 103.1 (1998), pp. 49–63.
- [41] R. J. Astley. “Infinite elements for wave problems: a review of current formulations and an assessment of accuracy”. In: *Int. J. Numer. Meth. Eng.* 49.7 (2000), pp. 951–976.
- [42] D. Dreyer. “Efficient Infinite Elements for Exterior Acoustics”. PhD thesis. Germany: TU Hamburg-Harburg, 2004.
- [43] A. Sommerfeld. *Partial differential equation in physics*. 1949.
- [44] P. Hohenberg and W. Kohn. “Inhomogeneous Electron Gas”. In: *Phys. Rev.* 136 (3B Nov. 1964), B864–B871.
- [45] W. Kohn and L. J. Sham. “Self-Consistent Equations Including Exchange and Correlation Effects”. In: *Phys. Rev.* 140 (4A Nov. 1965), A1133–A1138.
- [46] O. S. Bokareva et al. “Tuning Range-Separated Density Functional Theory for Photocatalytic Water Splitting Systems”. In: *J. Chem. Theory Comp.* 11.4 (Apr. 14, 2015), pp. 1700–1709.

- [47] G. Grell et al. “Multi-reference approach to the calculation of photoelectron spectra including spin-orbit coupling”. In: *J. Chem. Phys.* 143.7, 074104 (2015).
- [48] I. C. Gerber and J. G. Ángyán. “Potential curves for alkaline-earth dimers by density functional theory with long-range correlation corrections”. In: *Chem. Phys. Letters* 416.4–6 (2005), pp. 370–375.
- [49] I. C. Gerber and J. G. Ángyán. “Hybrid functional with separated range”. In: *Chem. Phys. Letters* 415.1–3 (2005), pp. 100–105.
- [50] S. Saha et al. “Coexistence of 1,3-butadiene conformers in ionization energies and Dyson orbitals”. In: *J. Chem. Phys.* 123.12, 124315 (2005).
- [51] A. Soba et al. “Real-space density functional theory and time dependent density functional theory using finite/infinite element methods”. In: *Comp. Phys. Comm.* 183.12 (Dec. 2012), pp. 2581–2588.
- [52] P. Bettess and R. A. Abram. “Finite and infinite elements for a simple problem in quantum mechanics”. In: *Commun. Numer. Meth En.* 18.5 (2002), pp. 325–334.
- [53] M. Valiev et al. “NWChem: A comprehensive and scalable open-source solution for large scale molecular simulations”. In: *Comput. Phys. Commun.* 181.9 (2010), pp. 1477–1489.
- [54] M. J. Frisch et al. *Gaussian 09 Revision E.01*.
- [55] T. Möhle. *FreeWilly*. 2017.
- [56] B. S. Kirk et al. “libMesh: A C++ Library for Parallel Adaptive Mesh Refinement/Coarsening Simulations”. In: *Eng. Comput.* 22.3–4 (2006), pp. 237–254.
- [57] V. Hernandez et al. “SLEPc: A scalable and flexible toolkit for the solution of eigenvalue problems”. In: *ACM Trans. Math. Software* 31.3 (2005), pp. 351–362.
- [58] V. Hernandez et al. “SLEPc: Scalable Library for Eigenvalue Problem Computations”. In: *Lect. Notes Comput. Sci.* 2565 (2003), pp. 377–391.
- [59] S. Balay et al. *PETSc Web page*. <http://www.mcs.anl.gov/petsc>. 2016.
- [60] S. Hüfner. *Photoelectron Spectroscopy*. 3rd ed. Berlin: Springer Verlag, 2003.
- [61] C. Milne et al. “Recent experimental and theoretical developments in time-resolved X-ray spectroscopies”. In: *Coordin. Chem. Rev.* 277–278 (Oct. 2014), pp. 44–68.
- [62] O. V. Gritsenko and E. J. Baerends. “Time-dependent Dyson orbital theory”. In: *Phys. Chem. Chem. Phys.* (2016).
- [63] S. Bauch et al. “Time-dependent generalized-active-space configuration-interaction approach to photoionization dynamics of atoms and molecules”. In: *Phys. Rev. A* 90.6 (Dec. 9, 2014).
- [64] H. R. Larsson et al. “Correlation effects in strong-field ionization of heteronuclear diatomic molecules”. In: *Phys. Rev. A* 93 (1 Jan. 2016), p. 013426.
- [65] A. Ponzi et al. “Dynamical photoionization observables of the CS molecule: The role of electron correlation”. In: *J. Chem. Phys.* 140.20, 204304 (2014).

- [66] Z. Sun et al. “Time-Dependent Wave Packet Split Operator Calculations on a Three-Dimensional Fourier Grid in Radau Coordinates Applied to the OClO Photoelectron Spectrum”. In: *J. Phys. Chem. A* 108.42 (2004), pp. 9226–9232.
- [67] T.-C. Jagau and A. I. Krylov. “Complex Absorbing Potential Equation-of-Motion Coupled-Cluster Method Yields Smooth and Internally Consistent Potential Energy Surfaces and Lifetimes for Molecular Resonances”. In: *JPCL* 5.17 (Sept. 4, 2014), pp. 3078–3085.
- [68] L. Journel et al. “First experimental determination and theoretical calculation of partial photoionization cross sections of lithium over the energy region of hollow Atomic States”. In: *Physical review letters* 76.1 (1996), p. 30.
- [69] S. Diehl et al. “Angle-Resolved Photoelectron Spectrometry Studies of the Autoionization of the 2 s 2 2 p 2 P Triply Excited State of Atomic Lithium: Experimental Results and R-Matrix Calculations”. In: *Physical review letters* 84.8 (2000), p. 1677.
- [70] A. Sunderland et al. “A parallel R-matrix program PRMAT for electron–atom and electron–ion scattering calculations”. In: *Comput. Phys. Commun.* 145.3 (2002), pp. 311–340.
- [71] Y. Yan and M. J. Seaton. “R-matrix theory of the hydrogen atom”. In: *J. Phys. B- At. Mol. Opt.* 18.13 (1985), p. 2577.
- [72] B. Buckley et al. “R-matrix calculations for electron-molecule scattering”. In: *Comp. Phys. Commun.* 17.1 (1979), pp. 175–179.
- [73] C. A. Bayse and K. N. Ortwine. “Calculation of Photoelectron Spectra of Molybdenum and Tungsten Complexes Using Green’s Functions Methods”. In: *J. Phys. Chem. A* 111.32 (2007), pp. 7841–7847.
- [74] J. Schirmer et al. “Strong correlation effects in the ionisation of CS<sub>2</sub>”. In: *Chem. Phys. Lett.* 61.1 (1979), pp. 30–35.
- [75] W. Richards. “The use of Koopmans’ Theorem in the interpretation of photoelectron spectra”. In: *Int. J. Mass Spectrom.* 2.6 (1969), pp. 419–424.
- [76] A. R. Schwager et al. “Photoelectron Spectra of the Alkyl Phenyl Disulfides”. In: *Phosphorus, Sulfur, and Silicon and the Related Elements* 70.1 (1992), pp. 287–295.
- [77] K. Prince et al. “Study of complex molecules of biological interest with synchrotron radiation”. In: *J. Electron Spectrosc.* 204, Part B (2015), pp. 335–344.
- [78] A. Lisini et al. “An analysis of configuration-interaction model spaces for the study of the core photoelectron spectra of small molecules”. In: *J. Phys. B- At. Mol. Opt.* 21.22 (1988), p. 3653.
- [79] I. Josefsson et al. “Collective hydrogen-bond dynamics dictates the electronic structure of aqueous I<sub>3</sub><sup>-</sup>”. In: *Phys. Chem. Chem. Phys.* 15 (46 2013), pp. 20189–20196.
- [80] M. Barysz and L. Syrocki. “Relativistic calculations of X-ray photoelectron spectra and the accuracy of the IOTC method\*”. In: *Mol. Phys.* 112.5-6 (2014), pp. 583–591.

- [81] A. W. Potts et al. “An experimental and theoretical study of the valence shell photoelectron spectra of purine and pyrimidine molecules”. In: *J Phys. B-A. Mol. Opt.* 36.14 (2003), p. 3129.
- [82] D. A. Egger et al. “Outer-valence Electron Spectra of Prototypical Aromatic Heterocycles from an Optimally Tuned Range-Separated Hybrid Functional”. In: *J. Chem. Theory Comput.* 10.5 (2014), pp. 1934–1952.
- [83] D. Yepes et al. “Photoemission Spectra and Density Functional Theory Calculations of 3d Transition Metal–Aqua Complexes (Ti–Cu) in Aqueous Solution”. In: *J. Phys. Chem. B* 118.24 (2014), pp. 6850–6863.
- [84] L. P. Kadanoff and G. Baym. *Quantum Statistical Mechanics: Green’s Function Method in Equilibrium and Nonequilibrium Problems*. Addison-Wesley Publishing Co. Inc., 1989.
- [85] W. Von Niessen et al. “Computational methods for the one-particle green’s function”. In: *Comput. Phys. Rep.* 1.2 (1984), pp. 57–125.
- [86] J. Schirmer et al. “New approach to the one-particle Green’s function for finite Fermi systems”. In: *Phys. Rev. A* 28 (3 Sept. 1983), pp. 1237–1259.
- [87] G. Onida et al. “Electronic excitations: density-functional versus many-body Green’s-function approaches”. In: *Rev. Mod. Phys.* 74 (2 June 2002), pp. 601–659.
- [88] L. Hedin. “New Method for Calculating the One-Particle Green’s Function with Application to the Electron-Gas Problem”. In: *Phys. Rev.* 139 (3A Aug. 1965), A796–A823.
- [89] M. J. Seaton. “Use of the R matrix method for bound-state calculations. I. General theory”. In: *J. Phys. B- At. Mol. Opt.* 18.11 (1985), p. 2111.
- [90] L. M. Kiernan et al. “Resonant photoionization of atomic lithium in the region of the first and second inner-shell thresholds”. In: *J Phys. B-A. Mol. Opt.* 29.6 (1996), p. L181.
- [91] B. M. McLaughlin and R. C. Forrey. “Low energy electron collisions with the N 2 H radical”. In: *J. Phys.: Conference Series* 388.5 (2012), p. 052027.
- [92] K. H. Johnson. “Scattered-Wave Theory of the Chemical Bond\*”. In: Advances in Quantum Chemistry 7 (1973). Ed. by P.-O. Löwdin, pp. 143–185.
- [93] J. C. Slater and K. H. Johnson. “Self-Consistent-Field  $X\alpha$  Cluster Method for Polyatomic Molecules and Solids”. In: *Phys. Rev. B* 5 (3 Feb. 1972), pp. 844–853.
- [94] F. Beleznay and M. J. Lawrence. “The ‘muffin-tin’ approximation in the calculation of electronic band structure”. In: *J. Phys. C Solid State* 1.5 (1968), p. 1288.
- [95] D. D. Koelling et al. “Shifts in the Electronic Band Structure of Metals Due to Non-Muffin-Tin Potentials”. In: *Phys. Rev. B* 1 (4 Feb. 1970), pp. 1318–1324.
- [96] M. Venut et al. “Valence photoionization of C<sub>6</sub>H<sub>6</sub> by the B-spline one-centre expansion density functional method”. In: *Chem. Phys.* 234.1 (1998), pp. 95–109.
- [97] J. A. Richards and F. P. Larkins. “Molecular photoionisation calculations with numerical continuum wavefunctions: application to the hydrogen molecule”. In: *J. Phys. B- At. Mol. Opt.* 17.6 (1984), p. 1015.

- [98] L. Tao et al. “Grid-based methods for diatomic quantum scattering problems: A finite-element discrete-variable representation in prolate spheroidal coordinates”. In: *Phys. Rev. A* 79 (1 Jan. 2009), p. 012719.
- [99] G. M. Krishnan et al. “Theoretical Study of the Electronic Nonadiabatic Transitions in the Photoelectron Spectroscopy of F<sub>2</sub>O”. In: *J. Phys. Chem. A* 110.3 (2006), pp. 1022–1030.
- [100] R. T. Pack and G. A. Parker. “Quantum reactive scattering in three dimensions using hyperspherical (APH) coordinates. Theory”. In: *J. Chem. Phys.* 87.7 (1987), pp. 3888–3921.
- [101] F. L. Yip et al. “Hybrid orbital and numerical grid representation for electronic continuum processes: Double photoionization of atomic beryllium”. In: *Phys. Rev. A* 81 (5 May 2010), p. 053407.
- [102] M. Ruckenbauer et al. “Revealing Deactivation Pathways Hidden in Time-Resolved Photoelectron Spectra”. In: *Sci. Rep.* (2016), p. 35522.
- [103] T. Åberg. “Theory of X-Ray Satellites”. In: *Phys. Rev.* 156 (1 Apr. 1967), pp. 35–41.
- [104] E. L. Michelsen. *Quirky Quantum Concepts*. Springer, 2014.
- [105] H. Park and R. N. Zare. “Molecular-orbital decomposition of the ionization continuum for a diatomic molecule by angle- and energy-resolved photoelectron spectroscopy. I. Formalism”. In: *J. Chem. Phys.* 104.12 (1996), p. 4554.
- [106] K. Gokhberg et al. “Molecular photoionization cross sections by Stieltjes-Chebyshev moment theory applied to Lanczos pseudospectra”. In: *J. Chem. Phys.* 130.6, 064104 (2009).
- [107] S. Gozem et al. “Photoelectron Wave Function in Photoionization: Plane Wave or Coulomb Wave?” In: *J. Phys. Chem. Lett.* 6.22 (2015), pp. 4532–4540.
- [108] L. C. Green et al. “Tables of the Continuum Wave Functions for Hydrogen.” In: *apjs* 3 (Nov. 1958), p. 459.
- [109] A. R. Edmonds. *Angular Momentum in Quantum Mechanics*. 4th ed. Princeton, New Jersey: Princeton University Press, 1996.
- [110] A. Humeniuk et al. “Time-resolved photoelectron imaging spectra from non-adiabatic molecular dynamics simulations”. In: *J. Chem. Phys.* 139.13, 134104 (2013).
- [111] G. Tomasello et al. “Exploring Ultrafast Dynamics of Pyrazine by Time-Resolved Photoelectron Imaging”. In: *J. Phys. Chem. A* 118.37 (2014), pp. 8437–8445.
- [112] B. Mignolet et al. “Probing Rapidly-Ionizing Super-Atom Molecular Orbitals in C<sub>60</sub>: A Computational and Femtosecond Photoelectron Spectroscopy Study”. In: *Chem. Phys. Chem.* 14.14 (2013), pp. 3332–3340.
- [113] P. Langhoff. “Bounds for second-order optical properties from quantum-mechanical sum rules and the theory of moments”. In: *Chem. Phys. Letters* 9.2 (1971), pp. 89–94.
- [114] J. Cukras et al. “Photoionization cross section by Stieltjes imaging applied to coupled cluster Lanczos pseudo-spectra”. In: *J. Chem. Phys.* 139.9, 094103 (2013).

- [115] P. Langhoff. “Stieltjes imaging of atomic and molecular photoabsorption profiles”. In: *Chem. Phys. Lett.* 22.1 (1973), pp. 60–64.
- [116] P. W. Langhoff et al. “Moment-theory investigations of photoabsorption and dispersion profiles in atoms and ions”. In: *Phys. Rev. A* 14 (3 Sept. 1976), pp. 1042–1056.
- [117] R. K. Nesbet. “Stieltjes imaging method for computation of oscillator-strength distributions for complex atoms”. In: *Phys. Rev. A* 14 (3 Sept. 1976), pp. 1065–1081.
- [118] L. Gong et al. “Numerical analysis on quantum dots-in-a-well structures by finite difference method”. In: *Superlattices and Microstructures* 60 (2013), pp. 311–319.
- [119] L. Gong et al. “Numerical computation of pyramidal quantum dots with band non-parabolicity”. In: *Superlattices and Microstructures* 61 (2013), pp. 81–90.
- [120] I. Gainullin and M. Sonkin. “High-performance parallel solver for 3D time-dependent Schrodinger equation for large-scale nanosystems”. In: *Comp. Phys. Comm.* 188 (2015), pp. 68–75.
- [121] S.-K. Son. “Voronoi-cell finite difference method for accurate electronic structure calculation of polyatomic molecules on unstructured grids”. In: *J. Comput. Phys.* 230.5 (2011), pp. 2160–2173.
- [122] F. Aurenhammer. “Voronoi Diagrams& Mdash;a Survey of a Fundamental Geometric Data Structure”. In: *ACM Comput. Surv.* 23.3 (Sept. 1991), pp. 345–405.
- [123] N. Sukumar. “Voronoi cell finite difference method for the diffusion operator on arbitrary unstructured grids”. In: *Int. J. Numer. Meth. Eng.* 57.1 (2003), pp. 1–34.
- [124] Q. Du and M. Gunzburger. “Grid generation and optimization based on centroidal Voronoi tessellations”. In: *Appl. Math. Comput.* 133.2–3 (2002), pp. 591–607.
- [125] S.-K. Son and S.-I. Chu. “Theoretical study of orientation-dependent multiphoton ionization of polyatomic molecules in intense ultrashort laser fields: A new time-dependent Voronoi-cell finite difference method”. In: *Chem. Phys.* 366.1–3 (2009), pp. 91–102.
- [126] B. Shizgal. *Spectral Methods in Chemistry and Physics. Applications to Kinetic Theory and Quantum Mechanics*. 2nd ed. Springer Verlag, 2015.
- [127] J. B. Fourier. *Theorie Analytique de la Chaleur*. Firmin Didot, 1822.
- [128] B. Fornberg. *A Practical Guide to Pseudospectral Methods*. Ed. by P. G. Ciarlet et al. Vol. 1. Cambridge University Press, 1996.
- [129] D. J. Tannor. *Introduction to Quantum Mechanics. A Time-dependent Perspective*. Sausalito, California: University Science Book, 2007.
- [130] D. Yu et al. “An improved Lobatto discrete variable representation by a phase optimisation and variable mapping method”. In: *Chem. Phys.* 458 (2015), pp. 41–51.
- [131] L.-Y. Peng and A. F. Starace. “Application of Coulomb wave function discrete variable representation to atomic systems in strong laser fields”. In: *JCP* 125.15, 154311 (2006).

- [132] R. Franke. “Scattered data interpolation: tests of some methods”. In: *Math. Comp.* 38.157 (1982), pp. 181–200.
- [133] J. C. Carr et al. “Surface interpolation with radial basis functions for medical imaging”. In: *IEEE Transactions on Medical Imaging* 16.1 (Feb. 1997), pp. 96–107.
- [134] A. Mohebbi et al. “The use of a meshless technique based on collocation and radial basis functions for solving the time fractional nonlinear Schrödinger equation arising in quantum mechanics”. In: *Eng. Anal. Bound. Elem.* 37.2 (2013), pp. 475–485.
- [135] L. Wang et al. “Study of radial basis collocation method for wave propagation”. In: *Eng. Anal. Bound. Elem.* 37.2 (2013), pp. 453–463.
- [136] M. W. Frazier. *An Introduction to Wavelets Through Linear Algebra*. New York: Springer, 1999.
- [137] S. Dahlke. “Wavelets: Construction Principles and Applications to the Numerical Treatment of Operator Equations”. PhD thesis. Germany: RWTH Aachen, 1996.
- [138] T. Torsti et al. “Three real-space discretization techniques in electronic structure calculation”. In: *Physica Status Solidi (B)* 243.5 (2006), pp. 1016–1053.
- [139] *Information technology – JPEG 2000 image coding system: Conformance testing*. Standard. International Organization for Standardization, Dec. 2004.
- [140] G. Plonka and M. Tasche. “On the Computation of Periodic Spline Wavelets”. In: *Appl. Comput. Harmonic Anal.* 2 2.1 (1995), pp. 1–14.
- [141] “6. Orthonormal Bases of Compactly Supported Wavelets”. In: *Ten Lectures on Wavelets*, pp. 167–213.
- [142] S. R. Jensen et al. “Linear scaling Coulomb interaction in the multiwavelet basis, a parallel implementation”. In: *Int. J. Modeling, Simulation Sci. Comput.* 05.sup01 (2014), p. 1441003.
- [143] *Wavelet Applications in Chemical Engineering*. 1st ed. Springer US, 1994.
- [144] A. Kunoth. *Wavelet Methods- Ellipting Boundary Value Problems and Control Problems*. 1st ed. Teubner, 2001.
- [145] P. F. Batcho. “Computational method for general multicenter electronic structure calculations”. In: *Phys. Rev. E* 61 (6 June 2000), pp. 7169–7183.
- [146] Y. Maday and R. Munoz. “Spectral element multigrid. II. Theoretical justification”. In: *J. Sci. Comput.* 3.4 (1988), pp. 323–353.
- [147] M. A. Watson and K. Hirao. “A linear-scaling spectral-element method for computing electrostatic potentials”. In: *J. Chem. Phys.* 129.18 (2008), p. 184107.
- [148] S. Petersen et al. “Practical considerations of the acoustic FEM for higher frequencies.” In: *30. Tagung der Arbeitsgemeinschaft für Akustik DAGA 2004*. Straßburg, 2004, pp. 307–308.
- [149] D. A. Mazziotti. “Spectral difference methods for solving differential equations”. In: *Chem. Phys. Lett.* 299.5 (1999), pp. 473–480.
- [150] C. Liang et al. “A p-multigrid spectral difference method with explicit and implicit smoothers on unstructured triangular grids”. In: *Computers & Fluids* 38.2 (2009), pp. 254–265.

- [151] Y. Liu et al. “Spectral difference method for unstructured grids I: Basic formulation”. In: *J. Comput. Phys.* 216.2 (2006), pp. 780–801.
- [152] M. N. Guimarães and F. V. Prudente. “A study of the confined hydrogen atom using the finite element method”. In: *J Phys. B-A. Mol. Opt.* 38.15 (2005), p. 2811.
- [153] D. Xu et al. “Solving the vibrational Schrödinger equation on an arbitrary multi-dimensional potential energy surface by the finite element method”. In: *Comput. Phys. Commun.* 180.11 (2009), pp. 2079–2094.
- [154] R. Alizadegan et al. “A divide and conquer real space finite-element Hartree–Fock method”. In: *J. Chem. Phys.* 132.3, 034101 (2010).
- [155] J. Fang et al. “A Kohn–Sham equation solver based on hexahedral finite elements”. In: *J. Comput. Phys.* 231.8 (2012), pp. 3166–3180.
- [156] W. Bangerth et al. “The `deal.II` Library, Version 8.4”. In: *J. Num. Math.* 24 (2016).
- [157] F. Hecht. “New development in FreeFem++”. In: *J. Numer. Math.* 20.3-4 (2012), pp. 251–265.
- [158] P. Karban et al. “Numerical solution of coupled problems using code Agros2D”. In: *Computing* 95.1 (2013), pp. 381–408.
- [159] B. Patzák. “OOFEM - an object-oriented simulation tool for advanced modeling of materials and structures”. In: *Acta Polytech.* 52.6 (2012), pp. 59–66.
- [160] C. Perdigou and B. Audoly. “The viscous curtain: General formulation and finite-element solution for the stability of flowing viscous sheets”. In: *J. Mech. Phys. Solids* 96 (2016), pp. 291–311.
- [161] F. Ballarin et al. “Fast simulations of patient-specific haemodynamics of coronary artery bypass grafts based on a POD-Galerkin method and a vascular shape parametrization”. In: *J. Comput. Phys.* 315 (June 2016), pp. 609–628.
- [162] H. Huang and B. W. Spencer. “Grizzly model of fully coupled heat transfer, moisture diffusion, alkali-silica reaction and fracturing processes in concrete”. In: *Proceedings of the 9th International Conference on Fracture Mechanics of Concrete and Concrete Structures (FraMCoS-9)*, Berkeley, CA. Ed. by V. Saouma et al. May 2016.
- [163] M. P. Lüthi et al. “Heat sources within the Greenland Ice Sheet: dissipation, temperate paleo-firn and cryo-hydrologic warming”. In: *The Cryosphere* 9.1 (2015), pp. 245–253.
- [164] P. Bauman et al. “Statistical calibration of thermocouple gauges used for inferring heat flux”. In: *42nd AIAA Thermophysics Conference, Fluid Dynamics and Co-located Conferences*. June 2011.
- [165] K. A. Gamble et al. “A feasibility study on the use of the MOOSE computational framework to simulate three-dimensional deformation of CANDU reactor fuel elements”. In: *Nuc. Eng. Des.* 293 (2015), pp. 385–394.
- [166] X. Yang et al. “Fluid–structure interaction analysis of the drop impact test for helicopter fuel tank”. In: *SpringerPlus* 5.1 (2016), p. 1573.

- [167] J. Ackermann. “Finite-element-method expectation values for correlated two-electron wave functions”. In: *Phys. Rev. A* 52 (3 Sept. 1995), pp. 1968–1975.
- [168] A. Scrinzi. “A 3-dimensional finite elements procedure for quantum mechanical applications”. In: *Comput. Phys. Commun.* 86.1 (1995), pp. 67–80.
- [169] J. S. Neto and J. Linderberg. “A numerical study of various finite-element method schemes applied to quantum mechanical calculations”. In: *Comput. Phys. Commun.* 66.1 (1991), pp. 55–65.
- [170] W. Zheng et al. “Numerical solutions of the Schrödinger equation for the ground lithium by the finite element method”. In: *Appl. Math. Comput.* 153.3 (2004), pp. 685–695.
- [171] J. Ackermann et al. “A self-adaptive multilevel finite element method for the stationary Schrödinger equation in three space dimensions”. In: *J. Chem. Phys.* 101.9 (1994), pp. 7643–7650.
- [172] J. E. Pask et al. “Real-space local polynomial basis for solid-state electronic-structure calculations: A finite-element approach”. In: *Phys. Rev. B* 59 (19 May 1999), pp. 12352–12358.
- [173] J. Linderberg. “Finite element methods in quantum mechanics”. In: *Comput. Phys. Rep.* 6.1 (1987), pp. 209–242.
- [174] L. Lehtovaara et al. “All-electron density functional theory and time-dependent density functional theory with high-order finite elements”. In: *J. Chem. Phys.* 131.5, 054103 (2009).
- [175] P. Motamarri et al. “Higher-order adaptive finite-element methods for Kohn–Sham density functional theory”. In: *J. Comput. Phys.* 253 (2013), pp. 308–343.
- [176] E. Romero and J. E. Roman. “A parallel implementation of Davidson methods for large-scale eigenvalue problems in SLEPc”. In: *ACM Trans. Math. Software* 40.2 (2014), 13:1–13:29.
- [177] V. Hernandez et al. “Parallel Arnoldi eigensolvers with enhanced scalability via global communications rearrangement”. In: *Parallel Comput.* 33.7–8 (2007), pp. 521–540.
- [178] J. M. Elble et al. “GPU computing with Kaczmarz’s and other iterative algorithms for linear systems”. In: *Parallel Comput.* 36.5–6 (2010), pp. 215–231.
- [179] F. Furche et al. “Accelerating molecular property calculations with nonorthonormal Krylov space methods”. In: *J. Chem. Phys.* 144.17, 174105 (2016).
- [180] I. Babuska et al. “The p-Version of the Finite Element Method”. In: *SIAM J. Numer. Anal.* 18.3 (1981), pp. 515–545.
- [181] W. Rachowicz et al. “Fully automatic hp-adaptivity in three dimensions”. In: *Comput. Method Appl. M.* 195.37–40 (2006), pp. 4816–4842.
- [182] A. Meinken. *Finite Elemente in der Praxis*. 1st ed. Expert Verlag, 2001.
- [183] Z.-C. Shi. “Nonconforming finite element methods”. In: *J. Comput. Appl. Math.* 149.1 (2002), pp. 221–225.

- [184] S.-W. Cheng and J. Dey Tamal K.and Shewchuk. *Delaunay Mesh Generation*. 1st ed. Taylor & Francis, 2012.
- [185] V. Lebedev and D. Laikov. “A quadrature formula for the sphere of the 131st algebraic order of accuracy”. In: *Dokl. Math.* 59.3 (1999), pp. 477–481.
- [186] R. S. Womersley and I. H. Sloan. “How good can polynomial interpolation on the sphere be?” In: *Adv. Comput. Math.* 14.3 (2001), pp. 195–226.
- [187] I. H. Sloan and R. S. Womersley. “Good approximation on the sphere, with application to geodesy and the scattering of sound”. In: *J. Comput. Appl. Math.* 149.1 (2002), pp. 227–237.
- [188] R. Santra. “Why complex absorbing potentials work: A discrete-variable-representation perspective”. In: *Phys. Rev. A* 74 (3 Sept. 2006), p. 034701.
- [189] J. Muga et al. “Complex absorbing potentials”. In: *Phys. Rep.* 395.6 (2004), pp. 357–426.
- [190] U. V. Riss and H.-D. Meyer. “The transformative complex absorbing potential method: a bridge between complex absorbing potentials and smooth exterior scaling”. In: *J. Phys. B- At. Mol. Opt.* 31.10 (1998), p. 2279.
- [191] W. P. Reinhardt. “Complex Coordinates in the Theory of Atomic and Molecular Structure and Dynamics”. In: *Ann. Rev. Phys. Chem.* 33.1 (1982), pp. 223–255.
- [192] T.-C. Jagau et al. “A Fresh Look at Resonances and Complex Absorbing Potentials: Density Matrix-Based Approach”. In: *JPCL* 5.2 (Jan. 16, 2014), pp. 310–315.
- [193] J. J. Shirron and I. Babuška. “A comparison of approximate boundary conditions and infinite element methods for exterior Helmholtz problems”. In: *Comput. Method Appl. M.* 164.1 (1998), pp. 121–139.
- [194] D. Givoli. “High-order local non-reflecting boundary conditions: a review”. In: *Wave Motion* 39.4 (2004), pp. 319–326.
- [195] S. Marburg and B. Nolte, eds. *Computational Acoustics of Noise Propagation in Fluids - Finite and Boundary Element Methods*. Springer, 2008.
- [196] F. Collino. “Perfectly Matched Absorbing Layers for the Paraxial Equations”. In: *J. Comput. Phys.* 131.1 (1997), pp. 164–180.
- [197] C. Zheng. “A perfectly matched layer approach to the nonlinear Schrödinger wave equations”. In: *J. Comput. Phys.* 227.1 (2007), pp. 537–556.
- [198] B. Engquist and A. Majda. “Absorbing boundary conditions for the numerical simulation of waves”. In: *Math. Comp.* 31.0436612 (1977), pp. 629–651.
- [199] R. Kechroud et al. “Preconditioning techniques for the solution of the Helmholtz equation by the finite element method”. In: *Math. Comput. Simulat.* 65.4–5 (2004), pp. 303–321.
- [200] H. Han and C. Zheng. “Exact Nonreflecting Boundary Conditions for an Acoustic Problem in Three Dimensions”. In: *J. Comput. Math.* 21.1 (2003), pp. 15–24.
- [201] R. J. Astley. “FE mode-matching schemes for the exterior Helmholtz problem and their relationship to the FE-DtN approach”. In: *Commun. Numer. Meth En.* 12.4 (1996), pp. 257–267.

- [202] D. Dai. “An improved boundary element formulation for wave propagation problems”. In: *Eng. Anal. Bound. Elem.* 10.4 (1992), pp. 277–281.
- [203] M. Costabel. “Principles of boundary element methods”. In: *Comput. Phys. Rep.* 6.1 (1987), pp. 243–274.
- [204] W.-T. Ang. *A Beginner’s Course in Boundary Element Methods*. Boca Raton, Florida: Universal Publishers, 2007.
- [205] S. K. Rana and A. Jena. “A BEM formulation of two dimensional steady state heat conduction in exchanger tubes of arbitrary cross sections”. In: *Int. J. Heat Mass Tran.* 106 (2017), pp. 195–211.
- [206] Y. Gong et al. “An isogeometric boundary element method for three dimensional potential problems”. In: *J. Comput. Appl. Math.* 313 (2017), pp. 454–468.
- [207] H. Wu et al. “A Fast Multipole Boundary Element Method for Three-Dimensional Half-Space Acoustic Wave Problems Over an Impedance Plane”. In: *Int. J. Comput. Meth.* 12.01 (2015), p. 1350090.
- [208] F. Guerracino et al. “A simple analysis of soil-structure interaction by BEM-FEM coupling”. In: *Eng. Anal. Bound. Elem.* 10.4 (1992), pp. 283–289.
- [209] O. C. Zienkiewicz et al. “The coupling of the finite element method and boundary solution procedures”. In: *Int. J. Numer. Meth. Eng.* 11.2 (1977), pp. 355–375.
- [210] D. Dreyer and O. Von Estorff. “Improved conditioning of infinite elements for exterior acoustics”. In: *Int. J. Numer. Meth. Eng.* 58.6 (2003), pp. 933–953.
- [211] L. Demkowicz and J. Shen. “A few new (?) facts about infinite elements”. In: *Computer Methods in Applied Mechanics and Engineering* 195.29–32 (2006), pp. 3572–3590.
- [212] K. Gerdes. “The conjugated vs. the unconjugated infinite element method for the Helmholtz equation in exterior domains”. In: *Comput. Method Appl. Mech. Eng.* 152.1–2 (1998), pp. 125–145.
- [213] D. Dreyer et al. “Effectiveness and robustness of improved infinite elements for exterior acoustics”. In: *Comput. Method Appl. M.* 195.29 (June 2006), pp. 3591–3607.
- [214] R. Astley and J. Hamilton. “The stability of infinite element schemes for transient wave problems”. In: *Comput. Method Appl. M.* 195.29 (June 2006), pp. 3553–3571.
- [215] G. L. G. Sleijpen and H. A. V. der Vorst. “A Jacobi–Davidson Iteration Method for Linear Eigenvalue Problems”. In: *SIAM J. Matrix Anal. Appl.* 17.2 (1996), pp. 401–425.
- [216] V. Simoncini and D. B. Szyld. “Theory of Inexact Krylov Subspace Methods and Applications to Scientific Computing”. In: *SIAM J. Sci. Comput.* 25.2 (2003), pp. 454–477.
- [217] D. Watkins. *The Matrix Eigenvalue Problem*. Society for Industrial and Applied Mathematics, 2007.
- [218] J. E. Roman et al. *SLEPc Users Manual*. Tech. rep. DSIC-II/24/02 - Revision 3.7. D. Sistemes Informàtics i Computació, Universitat Politècnica de València, 2016.

- [219] K.-J. Bathe and E. L. Wilson. “Solution methods for eigenvalue problems in structural mechanics”. In: *Int. J. Num. Meth. Eng.* 6.2 (1973), pp. 213–226.
- [220] V. Hernandez et al. *A survey of software for sparse eigenvalue problems*. Tech. rep. STR-4. Universitat Politècnica de València, 2009.
- [221] V. Hernandez et al. *A survey of software for sparse eigenvalue problems*. Tech. rep. STR-5. Universitat Politècnica de València, 2009.
- [222] V. Hernandez et al. *A survey of software for sparse eigenvalue problems*. Tech. rep. STR-7. Universitat Politècnica de València, 2009.
- [223] G. W. Stewart. “A Krylov–Schur Algorithm for Large Eigenproblems”. In: *Siam J. Matrix Anal. A.* 23.3 (2002), pp. 601–614.
- [224] M. E. Hochstenbach and G. L. G. Sleijpen. “Harmonic and refined Rayleigh–Ritz for the polynomial eigenvalue problem”. In: *Numer. Linear Algebra Appl.* 15.1 (2008), pp. 35–54.
- [225] U. Helmke and J. Jordan. “Control and Stabilization of Linear Equation Solvers”. In: *Perspectives in Mathematical System Theory, Control, and Signal Processing: A Festschrift in Honor of Yutaka Yamamoto on the Occasion of his 60th Birthday*. Ed. by J. C. Willems et al. Berlin, Heidelberg: Springer Berlin Heidelberg, 2010, pp. 73–82.
- [226] R. Shamasundar and W. Mulder. “Improving the accuracy of mass-lumped finite-elements in the first-order formulation of the wave equation by defect correction”. In: *J. Comput. Phys.* 322 (2016), pp. 689–707.
- [227] A. Aminfar and E. Darve. “A fast, memory efficient and robust sparse preconditioner based on a multifrontal approach with applications to finite-element matrices”. In: *Int. J. Numer. Meth. Eng.* 107.6 (2016), pp. 520–540.
- [228] W. Dahmen and A. Kunoth. “Multilevel preconditioning”. In: *Numer. Math.* 63.1 (1992), pp. 315–344.
- [229] H. Yserentant. “On the multi-level splitting of finite element spaces”. In: *Numer. Math.* 49.4 (1986), pp. 379–412.
- [230] N. Kushida. “Newton–Raphson preconditioner for Krylov type solvers on GPU devices”. In: *SpringerPlus* 5.1 (2016), p. 788.
- [231] C. M. Oana and A. I. Krylov. “Cross sections and photoelectron angular distributions in photodetachment from negative ions using equation-of-motion coupled-cluster Dyson orbitals”. In: *J. Chem. Phys.* 131.12 (2009), p. 124114.
- [232] R. Baer et al. “Tuned Range-Separated Hybrids in Density Functional Theory”. In: *Ann. Rev. Phys. Chem.* 61.1 (2010), pp. 85–109.
- [233] W. Koch and M. C. Holthausen. *A Chemist’s Guide to Density Functional Theory*. 2nd ed. Wiley-VCH Verlag GmbH, 2001.
- [234] A. D. Becke. “Density-functional exchange-energy approximation with correct asymptotic behavior”. In: *Phys. Rev. A* 38 (6 Sept. 1988), pp. 3098–3100.
- [235] C. Lee et al. “Development of the Colle-Salvetti correlation-energy formula into a functional of the electron density”. In: *Phys. Rev. B* 37 (2 Jan. 1988), pp. 785–789.

- [236] E. Runge and E. K. U. Gross. “Density-Functional Theory for Time-Dependent Systems”. In: *Phys. Rev. Lett.* 52 (12 Mar. 1984), pp. 997–1000.
- [237] A. Dreuw and M. Head-Gordon. “Single-Reference ab Initio Methods for the Calculation of Excited States of Large Molecules”. In: *Chem. Rev.* 105.11 (2005), pp. 4009–4035.
- [238] M. Casida et al. “Linear-Response Time-Dependent Density Functional Theory for Open-Shell Molecules”. In: *Time-Dependent Density Functional Theory*. Ed. by M. A. Marques et al. Berlin, Heidelberg: Springer Berlin Heidelberg, 2006, pp. 243–257.
- [239] Y. Tawada et al. “A long-range-corrected time-dependent density functional theory”. In: *J Chem. Phys.* 120.18 (2004), pp. 8425–8433.
- [240] J. P. Perdew et al. “Density-Functional Theory for Fractional Particle Number: Derivative Discontinuities of the Energy”. In: *Phys. Rev. Lett.* 49 (23 Dec. 1982), pp. 1691–1694.
- [241] P. Mori-Sánchez and A. J. Cohen. “The derivative discontinuity of the exchange-correlation functional”. In: *Phys. Chem. Chem. Phys.* 16 (28 2014), pp. 14378–14387.
- [242] J. Autschbach and M. Srebro. “Delocalization Error and “Functional Tuning” in Kohn–Sham Calculations of Molecular Properties”. In: *Acc. Chem. Res.* 47.8 (2014), pp. 2592–2602.
- [243] R. Ditchfield et al. “Self-Consistent Molecular-Orbital Methods. IX. An Extended Gaussian-Type Basis for Molecular-Orbital Studies of Organic Molecules”. In: *J. Chem. Phys.* 54.2 (1971), pp. 724–728.
- [244] G. A. Petersson et al. “A complete basis set model chemistry. I. The total energies of closed-shell atoms and hydrides of the first-row elements”. In: *J. Chem. Phys.* 89.4 (1988), pp. 2193–2218.
- [245] H. Iikura et al. “A long-range correction scheme for generalized-gradient-approximation exchange functionals”. In: *J. Chem. Phys.* 115.8 (2001), pp. 3540–3544.
- [246] F. Weigend and R. Ahlrichs. “Balanced basis sets of split valence, triple zeta valence and quadruple zeta valence quality for H to Rn: Design and assessment of accuracy”. In: *Phys. Chem. Chem. Phys.* 7 (18 2005), pp. 3297–3305.
- [247] G. Y. Lu and D. W. Wong. “An adaptive inverse-distance weighting spatial interpolation technique”. In: *Comput. Geosci.* 34.9 (2008), pp. 1044–1055.
- [248] L. de Mesnard. “Pollution models and inverse distance weighting: Some critical remarks”. In: *Comput. Geosci.* 52 (2013), pp. 459–469.
- [249] R. Franke. “Scattered data interpolation: tests of some methods”. In: *Math. Comput.* 38.157 (1982), pp. 181–200.
- [250] D. Zimmerman et al. “An Experimental Comparison of Ordinary and Universal Kriging and Inverse Distance Weighting”. In: *Mathematical Geology* 31.4 (1999), pp. 375–390.

- [251] D. E. Myers. “spatial interpolation: an overview”. In: *Geoderma* 62.1 (1994), pp. 17–28.
- [252] D. W. Silverstein et al. “Simulating One-Photon Absorption and Resonance Raman Scattering Spectra Using Analytical Excited State Energy Gradients within Time-Dependent Density Functional Theory”. In: *J. Chem. Theor. Comput.* 9.12 (2013), pp. 5490–5503.
- [253] T. Möhle. *NWC2Dy*. 2015.
- [254] G. Guennebaud, B. Jacob, et al. *Eigen v3*. <http://eigen.tuxfamily.org>. 2010.
- [255] H. Si. “TetGen, a Delaunay-Based Quality Tetrahedral Mesh Generator”. In: *ACM Trans. Math. Softw.* 41.2 (Feb. 2015), 11:1–11:36.
- [256] C. B. Barber et al. “The Quickhull algorithm for convex hulls”. In: *ACM Trans. Math. Software* 22.4 (1996), pp. 469–483.
- [257] H. Tomita et al. “Shallow Water Model on a Modified Icosahedral Geodesic Grid by Using Spring Dynamics”. In: *J. Comput. Phys.* 174.2 (2001), pp. 579–613.
- [258] D. A. Randall et al. “Climate modeling with spherical geodesic grids”. In: *Comput. Sci. Eng.* 4.5 (Sept. 2002), pp. 32–41.
- [259] M. A. Spackman. “Potential derived charges using a geodesic point selection scheme”. In: *J. Comput. Chem.* 17.1 (1996), pp. 1–18.
- [260] V. Lebedev. “Difference analogues of orthogonal decompositions, basic differential operators and some boundary problems of mathematical physics. II”. In: *USSR Comp. Math. Math+* 4.4 (1964), pp. 36–50.
- [261] R. H. Hardin and N. J. A. Sloane. “McLaren’s improved snub cube and other new spherical designs in three dimensions”. In: *Discrete & Computational Geometry* 15.4 (1996), pp. 429–441.
- [262] E. Bannai et al. “A survey on tight Euclidean t-designs and tight relative t-designs in certain association schemes”. In: *P. Steklov Inst. Math.* 288.1 (2015), pp. 189–202.
- [263] S.-H. Chien and P. M. W. Gill. “SG-0: A small standard grid for DFT quadrature on large systems”. In: *J. Comput. Chem.* 27.6 (2006), pp. 730–739.
- [264] X.-G. Wang and T. Carrington. “Using Lebedev Grids, Sine Spherical Harmonics, and monomer Contracted Basis Functions to Calculate Bending Energy Levels of HF Trimer”. In: *J. Theor. Comp. Chem.* 02.04 (2003), pp. 599–608.
- [265] R. M. Parrish et al. “Discrete variable representation in electronic structure theory: Quadrature grids for least-squares tensor hypercontraction”. In: *J. of Chem. Phys.* 138.19, 194107 (2013).
- [266] S. T. Brown et al. “Interpolation density values on a cartesian grid: Improving the efficiency of Lebedev based numerical integration in Kohn–Sham density functional algorithms”. In: *Chem. Phys. Letters* 418.4–6 (2006), pp. 490–495.
- [267] J. Fliege and U. Maier. “The distribution of points on the sphere and corresponding cubature formulae”. In: *IMA J. Numer. Anal.* 19.2 (1999), pp. 317–334.

- [268] R. S. Womersley and I. H. Sloan. “How good can polynomial interpolation on the sphere be?” In: *Adv. Comput. Math.* 14.3 (2001), pp. 195–226.
- [269] I. H. Sloan and R. S. Womersley. “Good approximation on the sphere, with application to geodesy and the scattering of sound”. In: *J. Comput. Appl. Math.* 149.1 (2002), pp. 227–237.
- [270] I. H. Sloan and R. S. Womersley. “Extremal Systems of Points and Numerical Integration on the Sphere”. In: *Adv. Comput. Math.* 21.1 (2004), pp. 107–125.
- [271] B. Keinert et al. “Spherical Fibonacci Mapping”. In: *ACM Trans. Graph.* 34.6 (Oct. 2015), 193:1–193:7.
- [272] Á. González. “Measurement of Areas on a Sphere Using Fibonacci and Latitude–Longitude Lattices”. In: *Math. Geosci.* 42.1 (2009), p. 49.
- [273] D. B. Meade et al. “Derivation and Comparison of Radiation Boundary Conditions for the Two-Dimensional Helmholtz Equation with Non-Circular Artificial Boundaries”. In: *Proceedings of the Third International Conference on Mathematical and Numerical Aspects of Wave Propagation Phenomena*. Mandelieu-La Napoule, France, 1995, pp. 506–514.
- [274] S. V. Tsynkov. “Numerical solution of problems on unbounded domains. A review”. In: *Appl. Numer. Math.* 27.4 (1998), pp. 465–532.
- [275] R. Mittra et al. “A review of absorbing boundary conditions for two and three-dimensional electromagnetic scattering problems”. In: *IEEE T. Magn.* 25.4 (July 1989), pp. 3034–3039.
- [276] “3. Perturbation Theory and Error Analysis”. In: *Numerical Methods for Large Eigenvalue Problems*, pp. 47–84.
- [277] J. H. Wilkinson, ed. *The Algebraic Eigenvalue Problem*. New York, NY, USA: Oxford University Press, Inc., 1988.
- [278] S. Krummacher et al. “Inner-shell photoemission studies of lithium and sodium vapour”. In: *J. Phys. B- At. Mol. Opt.* 15.23 (1982), p. 4363.
- [279] S. H. P. and L. Dong. “Theoretical study of the valence and core photoionization of a three-electron system from lithium to neon”. In: *J. Phys. B- At. Mol. Opt.* 30.7 (1997), p. 1651.
- [280] M. Stener et al. “Molecular photoionization cross sections by the local density LCAO Stieltjes imaging approach”. In: *J. Electron Spectrosc.* 74.1 (1995), pp. 29–43.
- [281] S.-Y. Liu et al. “He I Ultraviolet Photoelectron Spectroscopy of Benzene and Pyridine in Supersonic Molecular Beams Using Photoelectron Imaging”. In: *J. Phys. Chem. A* 115.14 (2011), pp. 2953–2965.

# A | Appendix

## A.1 Additional Data

### A.1.1 Comparison of Setup-schemes

Moreover, the library `tetgen` [255] used to construct the meshes also may vary the point-distribution locally by adding additional points to ensure high quality tetrahedra, *i.e.* the ratio of its circumsphere and the shortest edge is bounded in all results presented in this work by 1.5 and the maximum volume of any tetraheder is below  $8 \text{ bohr}^3$  whereby the latter has only minor influence on the mesh [255]. To compare the resulting meshes, in Table A.1 some characteristics of the results obtained for an atomic mesh (*i.e.* using only one sphere) are presented, using a Lebedev-grid [185] for the spherical distribution. As radial distribution, the tm-mapping eq.(5.15) is used for the schemes denoted as *const* and *tm* whereas eq.(5.14)) map is used for the scheme *son*. The number of points per sphere is  $M_i = 74$  for all spheres for the *const* scheme and according to eq.(5.16) and eq.(5.17) for the others, respectively. The parameters for the radial mapping are chosen as  $q = 1.8$  and  $p = 2.6$ . Some characteristic properties of the respective results are shown in Table A.1. The main conclusion to be drawn from Table A.1 is that the density of states is much larger for the radial mapping scheme suggested here compared to the son scheme. It should be noted, however, that the direct comparison of the schemes is disputable due to the different dependence on the parameter  $q$  and thus a more detailed study would be needed to draw definite conclusions about the quality of the schemes. Moreover, the density of eigenenergies is not uniform along the spectrum and thus can depend on the number of states taken into account. Finally, also the adaption of the mesh to ensure a good quality of the tetrahedra has some influence here.

To illustrate the very similar statistics obtained by the different mapping schemes described and discussed in section ??, in Figure A.2 further properties are shown, each normalised for better comparability. In the figures, the radius-edge ratio denotes the ratio of the radius of circumsphere divided by the sortest edge length.

scheme	runtime [s]	DOS <sup>a)</sup> $[(mE_h)^{-1}]$	number of nodes
const	438	7	3255
tm	825	13	5132
son	891	4	6368

Table A.1: Different properties of the solutions obtained with different setup-schemes as described in the text.

<sup>a)</sup>: density of states (eigenenergies), averaged over 23 states

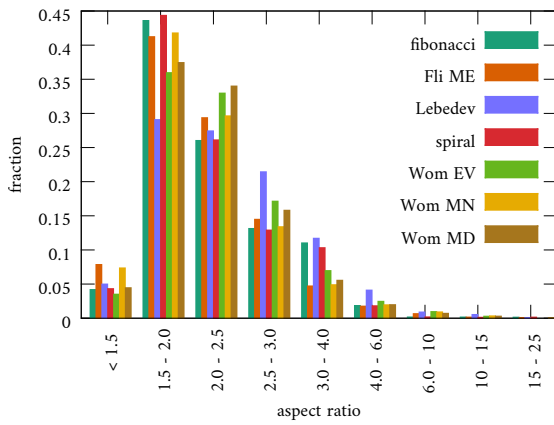


Figure A.1: Distribution of aspect ratio (longest edge length divided by the smallest side height). Be aware that the ranges of the different bins differ.

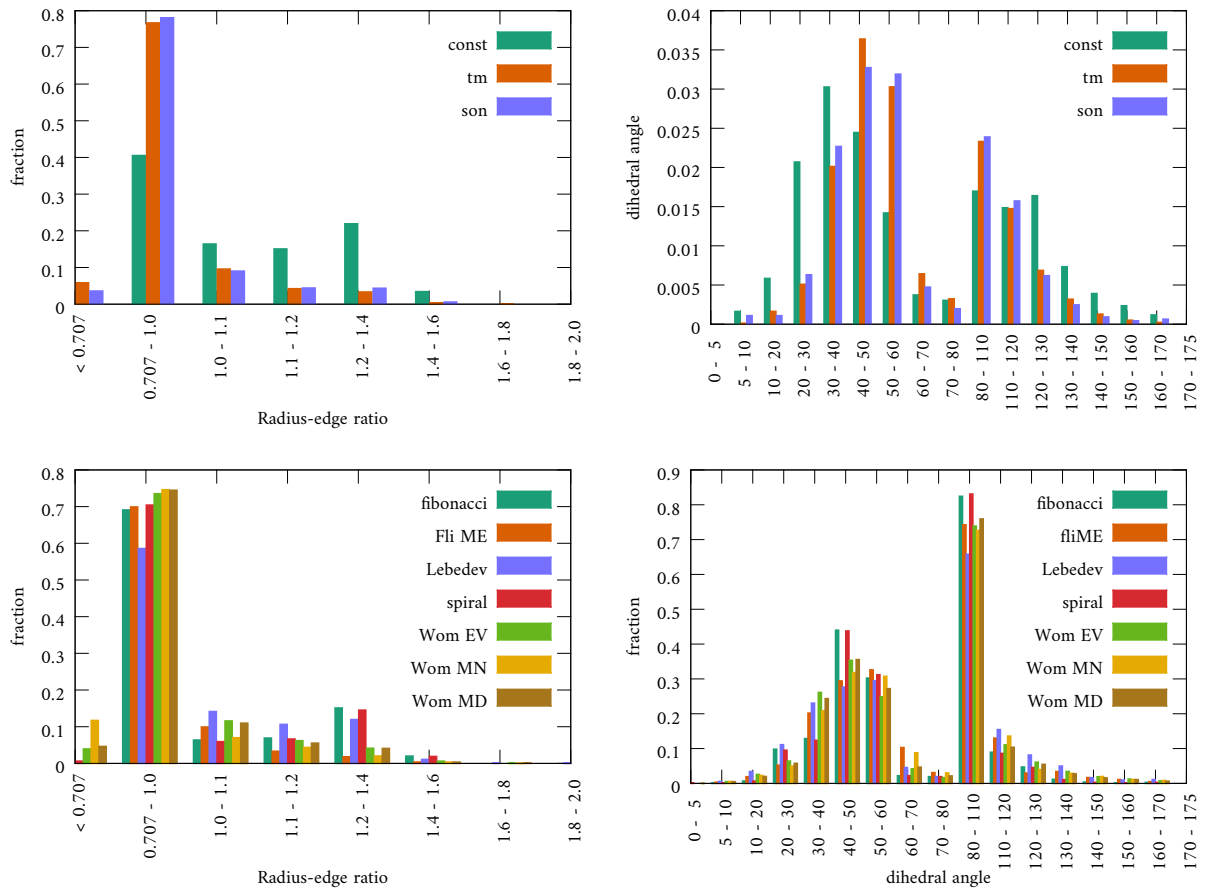


Figure A.2: Distribution of the ratio of radius and edge (left) and the dihedral angles (right) for the different radial schemes (top) and angular distributions (bottom) described in section ??.

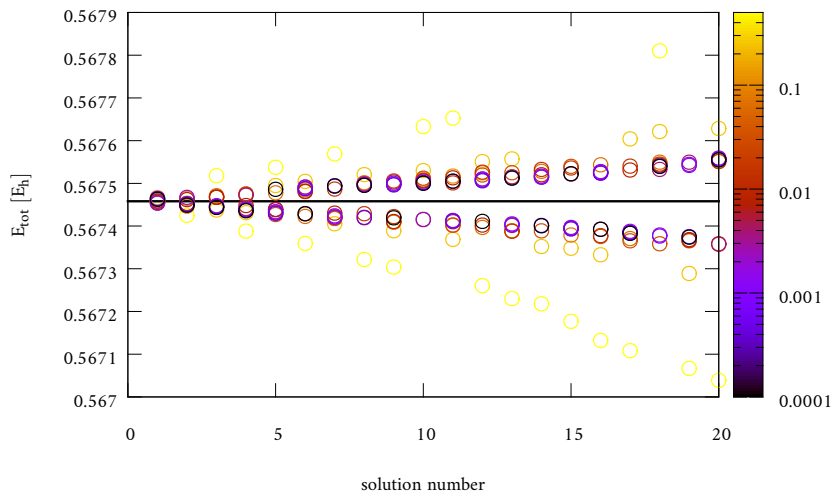


Figure A.3: The eigen energies of the first 20 solutions (circles) for different powers  $p$  of the damping function  $D(r)$  which determines the colours. The spectra do not change significantly for  $p < \frac{1}{8}$ .

### A.1.2 Cross section

### A.1.3 Photoelectron spectra of Sulphur

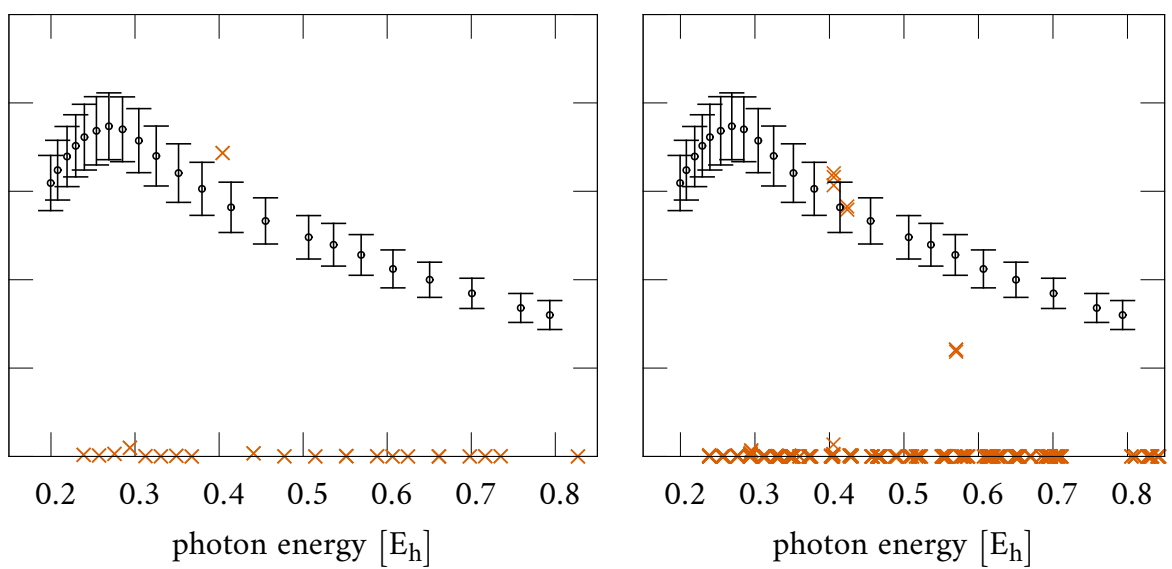


Figure A.4: Cross section of Lithium, obtained with a larger box.

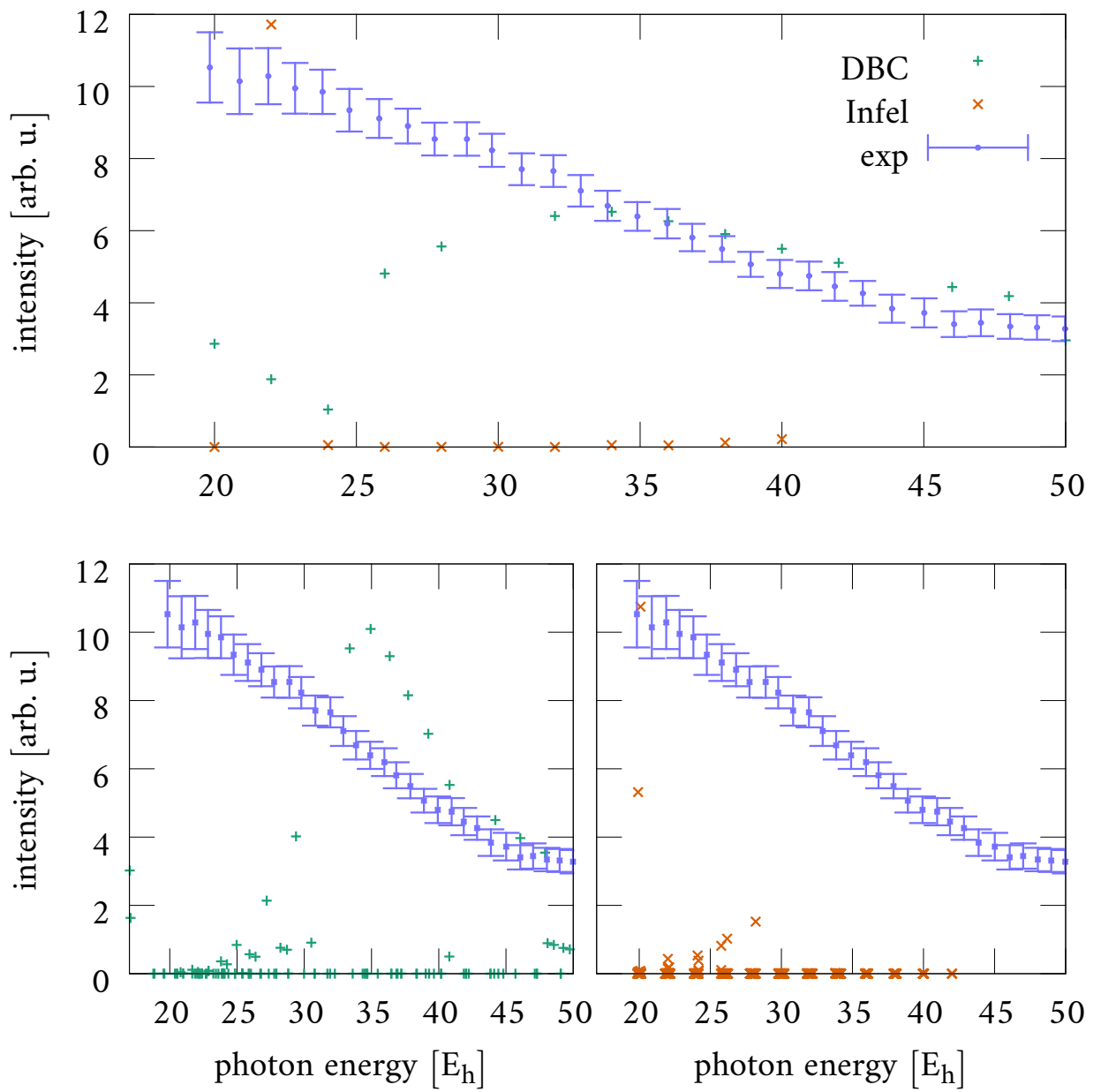


Figure A.5: Cross section of  $\text{CO}_2$  for the  $\pi_u$ -transition.

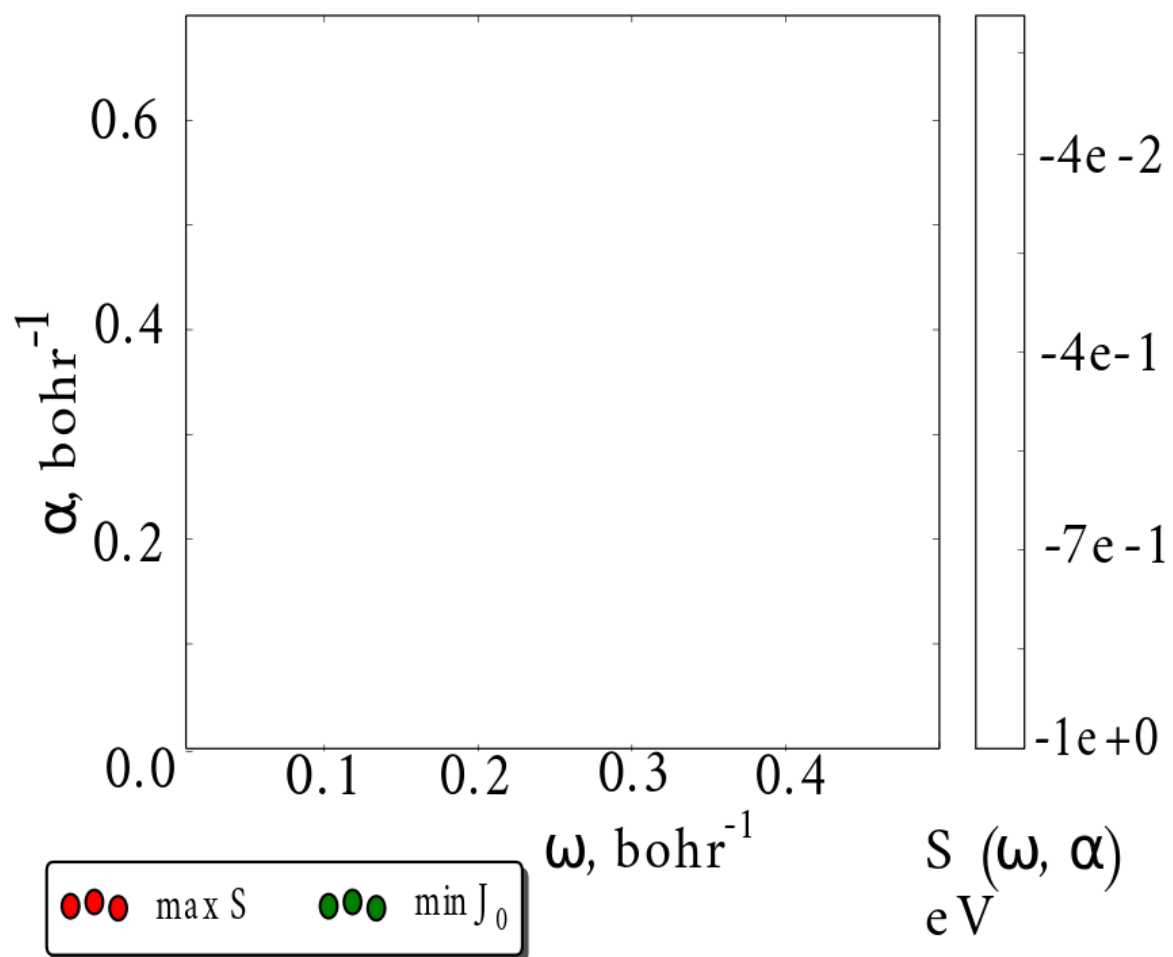


Figure A.6: deine Mudda

